
Multiscale Computing and Informatics Aided
Optimization for Perovskite-type Fast Li-Ion Conductive oxides

ペロブスカイト型リチウムイオン伝導性酸化物の
マルチスケールコンピューティングと
インフォマティクス最適化

Yang Zijian

名古屋工業大学大学院 工学研究科
生命・応用化学専攻

令和 2 年度博士論文

指導教員: 中山 将伸 教授

Table of Contents

Table of Contents	0
Chapter 1 Introduction	3
1.1 Preface	3
1.2 Lithium-ion battery	5
1.3 The solid-state Li-ion battery	7
1.4 Inorganic Solid-state electrolyte.....	10
1.5 Calculation and Simulation	23
1.6 The purpose of this work.....	31
Reference.....	32
Chapter 2. Arrangement in $\text{La}_{1/3}\text{NbO}_3$ Obtained by First-Principles Density Functional Theory with Cluster Expansion and Monte Carlo Simulation.....	39
2.1 Introduction	39
2.2 Research methods.....	43
2.3 Results and Discussion.....	46
2.4 Conclusion on Chapter 2	61
References	63
Chapter 3 Explore the diffusion mechanism of Li-ions in different modulated arrangements of $\text{La}_{(1-x)/3}\text{Li}_x\text{NbO}_3$ with the fitted force fields obtained via metaheuristic algorithm	65
3.1 Introduction	65
3.2 Research Method.....	67
3.3 Result and Discussion	72
3.4 Conclusion.....	84
Reference.....	86
Chapter 4. An Efficient Experimental Search for Discovering Fast Li Ion Conductor from Perovskite-type $\text{Li}_x\text{La}_{(1-x)/3}\text{NbO}_3$ (LLNO) Solid State Electrolyte Using Bayesian Optimization	88

4.1	Introduction.....	88
4.2	Research methods	89
4.3	Results and Discussion.....	91
4.4	Conclusion on Chapter 4.....	106
	Reference.....	110
	Chapter 5 Conclusion.....	112
	Chapter 6 Appendix	116
6.1	Density functional theory ¹⁻⁵	116
6.2	Monte Carlo method ⁷⁻¹³	121
6.3	Molecular Dynamics	128
	Reference.....	140

Chapter 1 Introduction

1.1 Preface

For environmental issues such as global warming, it is expected that electric vehicles using secondary battery technology and fuel cell technology, hybrid electric vehicles, fuel cell vehicles, etc. will be practically used. In order to put them into practical use, it is necessary to develop technical elements such as safety, long life, low cost, high energy density, and high output.

In secondary batteries such as lithium ion batteries, Li^+ moves between electrodes pass through electrolyte to perform charging and discharging in order to convert energy. However, since organic liquid electrolytes are unstable under high pressure and flammable conditions, conventional electrolytes used in current lithium ion battery technology are undesirable. In order to replace liquid electrolytes with solid-state materials, much effort has been made. Considering there is no probability of solid-state electrolyte to leakage or vaporization, it is a much safer development. Due to the low ionic conductivity of solid-state electrolytes. However, the current and voltage density of all-solid-state lithium-ion batteries is lower than that of conventional lithium-ion batteries. Solving these problems is the key to the commercialization of all-solid-state batteries.

The electrochemical properties of most solid-state materials are strongly related to their crystal structure and defect chemistry. In particular, the latter relates to the kinetics of electrochemical scheme and ion migration, and precise understanding of ionic arrangements in solids are often required. The energies for a given structure/arrangements are precisely determined by using Ab-initio density functional theory (DFT) calculations. However, the combination of possible arrangement of defects (Li/Cations/vacancy arrangement) is often huge, it is difficult to solve only by DFT calculations. Therefore, multi-scale calculation methods are usually used, in which the microscopic and macroscopic physical quantities are evaluated by tracking the microscopic motion of particles from a microscopic perspective (for example, at the atomic level).^{1,2} Figure 1.1 summarizes the main calculation methods.³

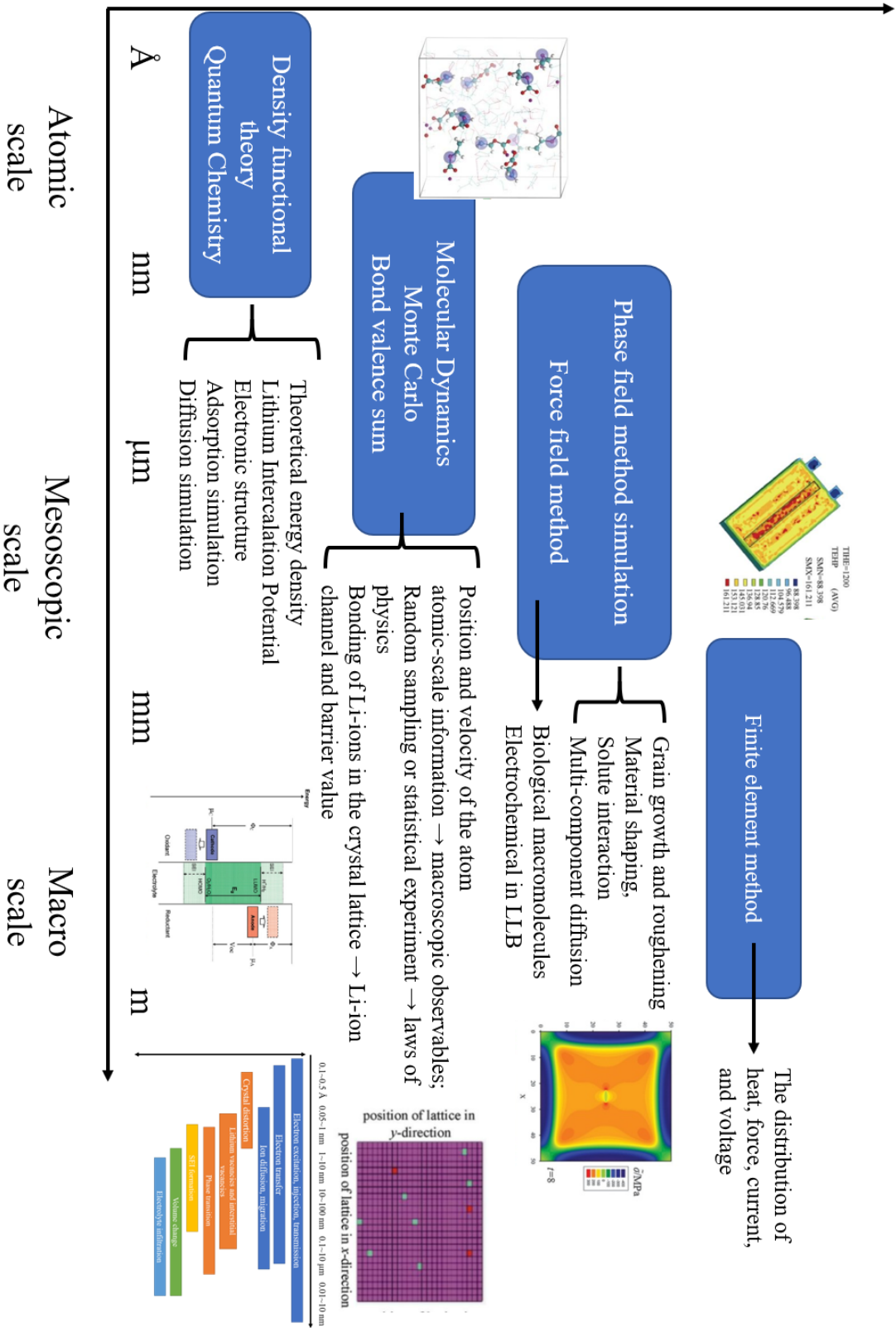


Fig 1.1 main calculation methods and their applicable scale and time scale

The purpose of this thesis is to conduct multi-scale material function analysis and design by evaluating ion conductivity from the knowledge of atomic structure and diffusion mechanism. If the mechanism of ion conduction can be clarified by linking microscopic crystal structure information, it will guide researcher to explore new material with better performance more scientifically. As the extension of this work, after revealing the relationship of ion conduction and microscopic structure, to further improve the electrochemical performance is necessary. However, when using traditional experimental method to design and screen the new material, faced with an infinite number of potentially feasible ternary or multi-component compounds and their derivatives is inevitable, we hope to speed up the exploration of feasible compounds. Combined with informatics methods is a possible way to reduce the complexity of the mutual constraints of multiple factors involved in the exploration process.

The outline of Chapter 1 is described as below. This chapter consist of the following five sections. Section 1.2 describe the principles of Li-ion batteries involved in this work. Section 1.3 describe the developments and advantages of all solid-state Li-ion batteries. Section 1.4 describe the main research target, solid-state electrolytes. In this section mainly introduces three important types of oxide solid electrolyte materials, structural characteristics, factors affecting lithium ion diffusion, and the research progress of these materials. Section 1.5 describe the basic concept of multi-scale calculation, which is the research method of this thesis and the recent research trends. Section 1.6 reiterate the purpose of this thesis and describe the structure of the entire paper.

1.2 Lithium-ion battery

Lithium batteries are divided into lithium batteries and Li-ion batteries. Mobile phones and notebook computers usually use Li-ion batteries with Li-containing materials as electrodes. Because they are widely used, they are usually called lithium batteries. The real lithium batteries are rarely used in daily electronic products due to their high risk.

Lithium-ion batteries were first successfully developed by Sony Corporation of Japan in the 1990s. By inserting lithium ions into carbon to form a negative electrode, the high activity of lithium is overcome, and the safety problem in traditional lithium batteries is solved. At the same time, the commonly used cathode material Li_xCoO_2 can reach a

higher level in charge and discharge performance, which reduces the cost and improves the overall performance of the lithium-ion battery.

John Goodenough, Stanley Whittingham and Akira Yoshino awarded the 2019 Nobel Prize in Chemistry in recognition of their contributions in the field of lithium-ion battery research and development.

1.2.1 Working principle

The charging and discharging process of lithium ion batteries essentially corresponds to the process of intercalation and deintercalation of lithium ions between the cathode and anode electrodes. Along with the back and forth movement of lithium ions inside the battery, the same amount of electrons flow into the external circuit, so the lithium ion battery is also vividly called the "rocking chair battery".^{4,5,6}

Taking a typical lithium-ion battery as an example, when graphite is used as the anode electrode, LiCoO_2 is used as the cathode electrode, and a non-aqueous liquid organic solvent is used as the electrolyte, the charging and discharging principle is shown as the Figure 1.2 and down below reaction:

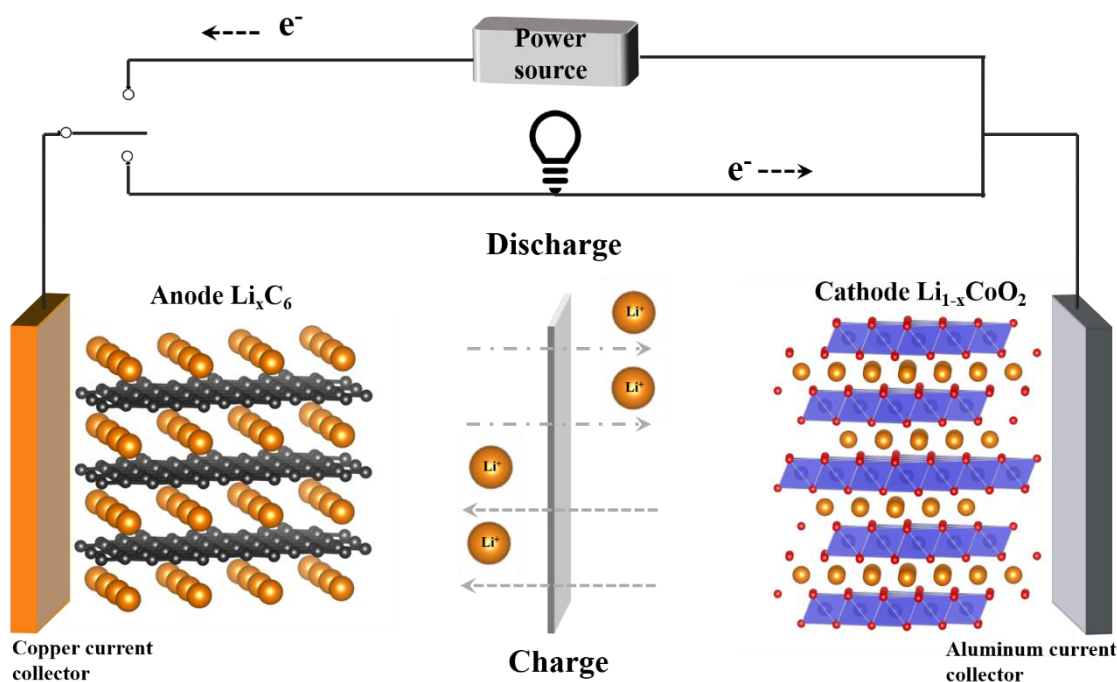
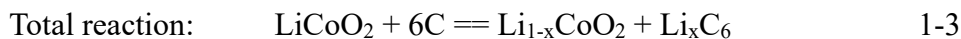
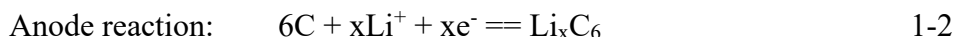
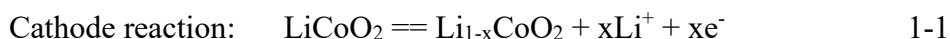


Fig. 1.2 Schematic model of the working mechanism of Li-ion battery



During charging, Li^+ is extracted from LiCoO_2 and an electron is released, C^{3+} is oxidized to C^{4+} . At the same time, Li^+ migrates from the electrolyte to the surface of the carbon anode electrode through the diaphragm and inserted into the graphite structure. The carbon anode electrode obtains an electron from the external circuit to form the lithium-carbon intercalation compound Li_xC_6 . The discharge process is the reverse process, Li^+ is extracted from the anode electrode and inserted into the cathode electrode LiCoO_2 . In this Li-ion battery, charge/discharge reactions are performed by repeating intercalation and deintercalation of lithium ions on two electrode materials, and lithium exists as an ionic state, so this type of battery also called “lithium-ion secondary battery”.

1.3 The solid-state Li-ion battery

Since the organic electrolytic solution is widely used in the Li-ion battery, there is a risk of liquid leakage and ignition. If the organic electrolyte can be replaced by the solid-state electrolyte, a highly reliable all-solid-state battery should be prepared. So far, researchers have achieved a lot of results on all-solid-state lithium-ion batteries.^{7,8}

Table 1.1 compares the advantages and disadvantages of organic liquid electrolytes, gel electrolytes and solid-state electrolytes. Compared with the first two types of electrolytes, solid-state electrolytes have outstanding advantages in terms of safety, thermal stability, and electrochemical stability. Therefore, replacing the electrolyte with a solid electrolyte and developing an all-solid-state lithium-ion battery is the only way to fundamentally solve the safety problem. The structure of the all-solid lithium ion battery includes a positive electrode, an electrolyte, and a negative electrode, all of which are composed of solid materials, as shown in Table 1.1 The solid-state electrolyte conducts lithium ions while acting as a separator to prevent electron transmission, making the battery construction process complete significantly simplified.

1.3.1 The advantage of solid state Li-ion battery

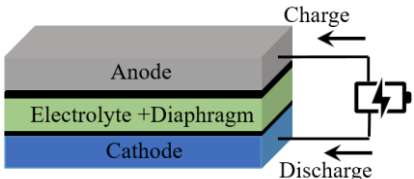
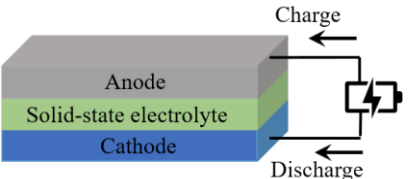
Compared with the traditional electrolyte lithium-ion battery, the all-solid-state lithium-ion battery has the advantages:⁹

1. Completely eliminates the potential safety hazards of electrolyte corrosion and leakage and has higher thermal stability. The battery shell and cooling system module can be simplified to reduce the weight of the battery, thereby increasing the energy density.
2. No need to encapsulate the liquid, support the serial stack arrangement and bipolar mechanism, which can reduce the ineffective space in the battery pack and improve the production efficiency.
3. Because of the solid-state characteristics of the solid electrolyte, it can be stacked. Two electrodes make it possible to prepare 12 V and 24 V high-voltage single cells in series in the unit.
4. The electrochemical stability window is wide (up to 5 V or more), which can match high-voltage electrode materials, and the energy density and power density are further improved.
5. Solid electrolyte is generally a single-ion conductor, and there are almost no side reactions, so a longer service life can be obtained. The unique advantages of all-solid-state lithium-ion batteries make them have considerable potential in the fields of large batteries and ultra-micro and ultra-thin batteries.

1.3.2 The development of all-solid-state Li-ion battery

Research institutions around the world are actively researching all-solid-state lithium-ion batteries and are committed to bringing them to the market, including some large electronics and automobile manufacturing companies, such as South Korea's Samsung Electronics and Japan's Toyota Motor.

Table 1.1 Comparison of the properties of different electrolytes and their lithium-ion battery systems

Properties	Liquid/gel electrolyte		Solid-state electrolyte	
			Organic polymer (PEO based)/	Inorganic (Oxide, Sulfide)
Ionic conductivity	High 10^{-2} S/cm	Moderate $> 10^{-4}$ S/cm	Highest 10^{-3} S/cm	Highest 10^{-2} S/cm
Battery structure				

Advantages	Wide range of applications, including 3C products and energy storage / No leakage problem	High electrochemical stability High safety, with flexible processing characteristics/ Very high safety, suitable for long-term storage, good high-temperature performance
Disadvantages	Flammable and explosive, electrochemical stability is not high	Low power density, low energy density, low cycle life, high cost

Replacing traditional organic electrolytes with solid electrolytes to prepare solid-state batteries can fundamentally solve the safety problems of lithium-ion batteries. At present, a large amount of work is concentrated on the development of all-solid-state lithium-ion batteries with higher energy and power density. In the process of advancing the industrialization of high-safety and high-energy storage batteries, the development and preparation of key materials (solid electrolyte, positive electrode and negative electrode) is the most important thing. With the deepening of research, solid electrolytes have developed: PEO and its derivative systems polymer electrolytes,¹⁰ LiPON thin film electrolytes,⁷ oxide and sulfide crystalline electrolytes,¹¹ and sulfide glass electrolytes,¹² the ionic conductivity has been continuously improved. At present, the solid electrolyte materials most likely to be applied to all-solid-state lithium-ion batteries include PEO-based polymer electrolytes, NASICON-type and garnet-type oxide electrolytes,¹³ and sulfide electrolytes. PEO-based polymer batteries have been industrialized.^{14,15} It has reported that perovskite-type electrolyte LLTO exhibits high conductivity of 10^{-3} S/cm at room temperature with the activation energy of 0.4 eV.^{7,16} The room temperature ion conductivity of garnet-type crystalline oxide electrolytes represented by LAGP and LLZO has reached the order of 10^{-3} S/cm and has high stability in the air.^{17,18} Sulfide electrolytes generally have high conductivity, and the room temperature ion conductivity can reach the order of 10^{-2} S/cm, which is equivalent to organic electrolytes.^{11,12}

Examples of lithium-ion conductors reported so far and their ionic conductivity are summarized in Figure 1.3.¹⁹ In the development of these materials, technologies related to ceramics such as analysis of lithium ion migration mechanism, analysis of crystal structure or structural design, and synthesis technology play a major role.

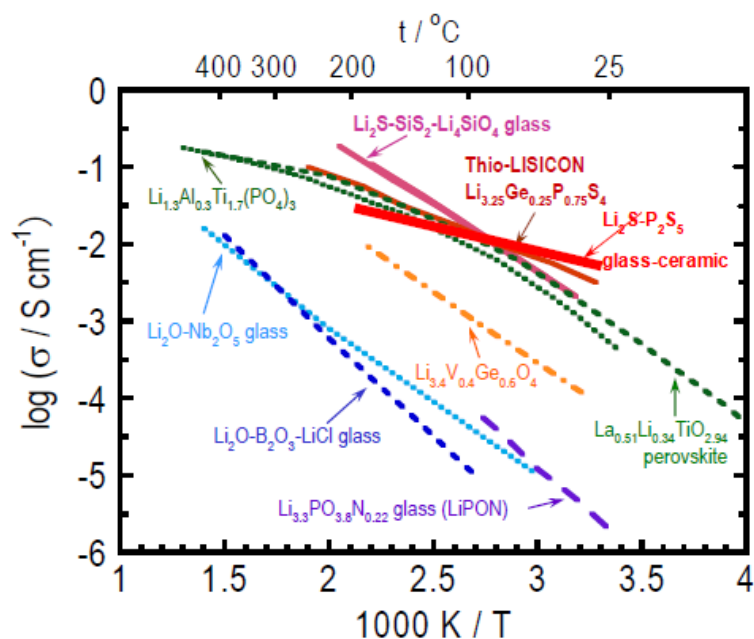


Fig 1.3 Ionic conductivity of various lithium ion conductor.¹⁹

1.4 Inorganic Solid-state electrolyte

Both sulfide electrolyte and oxide electrolyte contain three different crystalline materials: glass, ceramic, and glass-ceramic. In general, since S^{2-} has a weaker binding effect on Li -ion compared to O^{2-} , which is beneficial to the migration of Li^+ , the conductivity of sulfides is often significantly higher than that of oxides of the same type. In oxides, Li -ion migrates in the gap of the framework structure composed of O^{2-} which size is much large than Li^+ , this will weaken the Li - O interaction. With many years development, some oxide Li -ion conductor materials with complex structures have appeared one after another. Representative ones include the NASICON structure system, Garnet structure system, and Perovskite structure system. In this section, I will basically introduce the development of these three types of solid-state electrolytes.

1.4.1 NASICON type solid-state electrolyte

NASICON (sodium (Na) Super Ion Conductors) type fast ion conductor material is a type of solid electrolyte material that has been widely studied. The crystal structure of this type of material was first reported in 1968.²⁰ In 1976, Goodenough and Hong²¹ reported a new material composed of $Na_3Zr_2Si_2PO_{12}$, which is the Na^+ ion conductive material commonly known as NASICON. The molecular formula of this type material is

$M[A_2B_3O_{12}]$, where M, A, and B represent monovalent, tetravalent and pentavalent cations, respectively. The skeleton structure is formed by AO_6 octahedron and BO_4 tetrahedron, this material belongs to $R\bar{3}c$ space group. Each AO_6 octahedron is connected with 6 BO_4 tetrahedrons, and each BO_4 tetrahedron is connected with 4 AO_6 octahedrons. These polyhedrons are connected by vertex oxygen atoms to form a three-dimensional interconnected skeleton structure, also forming ions pathway which parallel to the c-axis. The schematic diagram of its structure and ion transmission is shown in Figure 1.4 (The yellow ball represents the MI site, the hollow square represents the MII site, and the arrow represents the M^+ transmission pathway).¹³

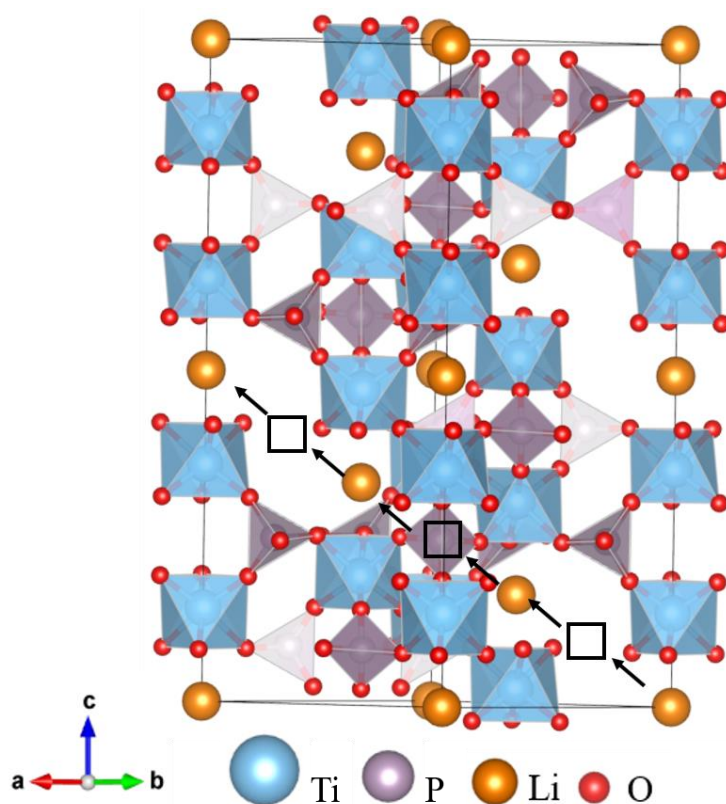


Fig 1.4 Structure schematic of NASICON type electrolyte

In this structure, M^+ conductive ions can occupy two interstitial positions. These positions are called MI site (octahedral void, the position occupied by the blue ball) and MII site (tetrahedral void, black hollow square position). Since the potential energy of the MI site is lower than that of the MII site, the MI site is fully occupied by M^+ , and usually the MII site is not occupied. Therefore, in the NASICON structure, there are two migration pathway for M^+ : one is through the MIMII bottleneck MI-MII transition, the other is through the MIIMII bottleneck MII-MII transition. When M^+ conductive ions

migrate through the bottleneck, there is a coordinated movement of $[A_2B_3O_{12}]^-$ skeleton shrinkage and M^+ migration. Only when the radius of the transmission channel match the migration ion at a certain degree, that can be beneficial to M^+ migration. However, the size of transmission channel depends on the size of skeleton $[A_2B_3O_{12}]^-$. Therefore, the ionic conductivity of the NASICON type material will change with the composition of the skeleton $[A_2B_3O_{12}]^-$ ion.^{22,23} The prerequisite for improving the ionic conductivity of the NASICON type solid-state electrolyte is that the ion transmission channel and the migration ions' radius must be matched, the skeleton structure has a weak binding effect on the migration ions, and the material has a stable structure and high density.^{10,24}

Replace the Na-ion in $Na_3Zr_2Si_2PO_{12}$ with the Li-ion, it becomes a solid-state electrolyte for the lithium-ion batteries, but with preparation method of direct substitution, $Li_3Zr_2Si_2PO_{12}$ has a very low Li-ionic conductivity, which is about 3 orders of magnitude lower than the Na-ionic conductivity of $Na_3Zr_2Si_2PO_{12}$. The reason of that is the original size of the transmission channel in the $Na_3Zr_2Si_2PO_{12}$ structure is only suitable for Na^+ , which means it is too large compared to Li^+ . The solution is to replace the structural skeleton ions with the ions of different sizes, thereby changing the size of the transmission channel.²⁵ Among the possible candidates, Zr^{4+} can be replaced by Ti^{4+} , Ge^{4+} , Hf^{4+} , V^{5+} or Sc^{3+} , after the substitution, the compound can still maintain the NASICON structure, but significantly improved the Li-ionic conductivity.^{26,27} It has the characteristics of stable structural properties and convenient synthesis. It will have good application potential as a solid electrolyte with high ionic conductivity. However, its room temperature conductivity needs to be further improved. Therefore, improving the room temperature lithium ion conductivity of NASICON structural materials has become a hotspot of research.

As far as we know, most inorganic solid electrolytes are polycrystalline materials. The bulk ionic conductivity of solid electrolytes is the sum of the contribution of grains and grain boundary conductance to the total conductance, and the contribution of grain boundaries will dominate under certain conditions. The grain boundary conductivity of is 1~2 orders of magnitude lower than that of grain ionic conductivity, which limit the electrochemical performance of NASICON type solid electrolytes. After many years development, the total ionic conductivity at room temperature of NASICON-type material has been significantly improved, the modification ideas are mainly rely on

collective effective of grains and grain boundaries. Utilized low-valent ions of appropriate size to replace high-valent ions in the framework structure, such as Al^{3+} and Ga^{3+} for the A position, and Si^{4+} for the B position, without changing the crystal phase structure, the introduction of low-valent ions can change the size of the ion transport channel on the one hand, and on the other hand, because of the charge balance, it can introduce more transferable Li-ion, which will affect the total ionic conductivity from two aspects.²⁸ In the study of grain boundary control, the first is to optimize the preparation method. The common solid-phase reaction method is difficult to produce products with uniform particle size and single phase. Co-precipitation method and sol-gel method are used to synthesize the product, and the product is uniform. And phase purity has been significantly improved.^{29,30} Secondly, using the traditional solid-phase reaction method, it is difficult to form a product with a dense structure even at a very high temperature, while new preparation processes such as spark plasma sintering (SPS) and mechanochemical synthesis can increase the density of the product (even greater than 99%).^{30,31} Before the sample is synthesis, adding low-melting lithium-containing compounds which will not undergo chemical reactions, such as Li_3PO_4 , Li_3BO_3 , etc., and fill them in the inter-grain voids during the sintering process to improve the interface contact, thereby increasing the density, and also helping to increase conductive Li-ion concentration at the grain boundary.³²

Among the Li-ion conductive materials of NASICON type, the most studied is about $\text{LiM}_2(\text{PO}_4)_3$ (M= Zr, Ti, Ge, Hf), the representatives are $\text{Li}_2\text{O}-\text{Al}_2\text{O}_3-\text{TiO}_2-\text{P}_2\text{O}_5$ (LATP) and $\text{Li}_2\text{O}-\text{Al}_2\text{O}_3-\text{GeO}_2-\text{P}_2\text{O}_5$ (LAGP). Generally, the system with M being Ti^{4+} has the best transmission channel of Li-ion, so these systems have better electrochemical performance.³³ The summaries of the development of LATP and LAGP as shown in Table 1.2 and Table 1.3, respectively.

Table 1.2 Summary LATP based Li-ion solid electrolytes

Author	Composition	Research characteristics
Kotobuki ²⁹	$\text{Li}_{1.5}\text{Al}_{0.5}\text{Ti}_{1.5}(\text{PO}_4)_3$	Sol-gel method; Different aluminum sources will generate impurity phases to hinder Li-ion migration.
Ymamoto ³⁴	$\text{Li}_{1.4}\text{Al}_{0.4}\text{Ti}_{1.4}\text{Ge}_{0.2}(\text{PO}_4)_3$	Sol-gel method; 1.29×10^{-3} S/cm; density 94.4%

Xu ³¹	$\text{Li}_{1.4}\text{Al}_{0.4}\text{Ti}_{1.6}(\text{PO}_4)_3$	SPS method; 1.12×10^{-3} S/cm; The sintering temperature is greatly reduced, the grain size of the sample reaches the nanometer level, and the grain boundary ionic conductivity is increased by about 2 times
Morimoto ³⁵	$\text{Li}_{1.3}\text{Al}_{0.3}\text{Ti}_{1.7}(\text{PO}_4)_3$	Mechanical grinding; $\sim 10^{-4}$ S/cm
Wen ³⁶	$\text{Li}_{1.4}\text{Al}_{0.4}\text{Ti}_{1.6}(\text{PO}_4)_3$	Mechanical grinding; 5.16×10^{-4} S/cm; point out that decrease the size of grain is the key
Aono ²⁵	$\text{Li}_{1.3}\text{Al}_{0.3}\text{Ti}_{1.7}(\text{PO}_4)_3$ / $\text{Li}_{1.3}\text{Sc}_{0.3}\text{Ti}_{1.7}(\text{PO}_4)_3$	The Ti^{4+} was replaced by Al^{3+} , Sc^{3+} ; 7×10^{-4} S/cm
	$\text{Li}_{1.3}\text{Ti}_2(\text{P}_{0.9}\text{Si}_{0.1}\text{O}_4)_3$	The P^{5+} was replaced by Si^{4+} ; 3.2×10^{-4} S/cm;
Johnson ³⁷	$\text{Li}_{1.5}\text{Al}_{0.3}\text{Ti}_{1.7}\text{Si}_{0.2}\text{P}_{2.8}\text{O}_{12}$	Co-replacement by Al^{3+} , Si^{4+} ; 2.77×10^{-4} S/cm; Poor sintering performance
Kumar ³⁸	$\text{Li}_{1.4}\text{Al}_{0.4}\text{Ti}_{1.6}(\text{PO}_4)_3$	Space charge effect; Add a small amount of high-dielectric phase BST and low-dielectric phase Al_2O_3 to composite with LATP glass ceramics; Overgrowth of dielectric phase, blocking effect

Table 1.3 Summary of LAGP based Li-ion solid electrolytes

Author	Composition	Research characteristics
Fu ³⁹	$\text{Li}_{1+x}\text{Al}_x\text{Ge}_{2-x}(\text{PO}_4)_3$ $X=(0,0.2,0.4,0.6,0.8)$	$x=0.5$ The stability of the system is better. $x=0.5\sim 0.6$, the material has high room temperature conductivity and low activation energy E_a ; $\sim 10^{-4}$ S/cm; 0.375 eV
He ⁴⁰	$\text{Li}_{1+x}\text{Al}_x\text{Ge}_{2-x}(\text{PO}_4)_3$ $x=(0\sim 0.7)$	Analysis the effect of Al_2O_3 , $x=0.5$, 5.8×10^{-4} S/cm, $x>0.5$, the impurity phase appear.
Fu ⁴¹	$\text{Li}_{1.2}\text{M}_{0.2}\text{Ge}_{1.8}(\text{PO}_4)_3$ (M=Al, Ga, Y, Dy, Gd, La)	The Al^{3+} and Ga^{3+} substitution samples have higher ionic conductivity. Due to the poor ion size matching of other ions, the lattice structure is distorted and the ionic conductivity decreases.

Takashi ⁴²	$\text{Li}_{1+x+y}\text{Al}_x(\text{Ti}_{2-y}\text{Ge}_y)\text{P}_3\text{-}_x\text{Si}_2\text{O}_{12}$	Combined with LATP and LAGP, and partially replaced by Si^{4+} and P^{5+} , the stability of the sample is improved, but the after assembled the performance is decreased.
Xu ⁴³	$\text{Li}_{1.5}\text{Al}_{0.5}\text{Ge}_{1.5}(\text{PO}_4)_3\text{-}_x\text{Li}_2\text{O}$ $x=(0,0.05,0.075,0.1,0.2)$	Excessive lithium helps to increase the density of the sample, but excessive lithium will cause abnormal growth of crystal grains, and there will be gaps between the crystal grains, resulting in a decrease in density; $x=0.05$, 7.25×10^{-4} S/cm
Jadhav ⁴⁴	$\text{Li}_{1.5}\text{Al}_{0.5}\text{Ge}_{1.5}(\text{PO}_3)_4$	Explored the effect of B_2O_3 , B_2O_3 would reduce the crystallization temperature of the sample and increase the diffusion of Li-ion at grain boundary; B_2O_3 (0.05% wt) 6.9×10^{-4} S/cm
Thokchom ⁴⁵	$\text{Li}_{1.5}\text{Al}_{0.5}\text{Ge}_{1.5}(\text{PO}_3)_4$	Melt-quench method; the grain ionic conductivity is higher; 5.08×10^{-3} S/cm

1.4.2 Garnet type solid-state electrolyte

In the ideal garnet type structure $\text{X}_3\text{Y}_2(\text{SiO}_4)_3$ (X=Ca, Mg, Fe, etc.; B=Al, Cr, Fe, etc.), X and Y are the eight-coordinate and six-coordinate O^{2-} , respectively. It can be seen that in the garnet structure contains eight-coordinated, six-coordinated and four-coordinated cations, and various cations are in different valence states. Therefore, X, Y or Si^{4+} can be replaced by alkali metals, alkaline earth metals, rare earth metals and transition metal ions.

The Li-containing garnet material $\text{Li}_3\text{Ln}_3\text{M}_2\text{O}_{12}$ (M=W, Te) was discovered by Kasper⁴⁶ as early as 1969. Subsequently, Mazza and Hyooma studied the ternary phase diagram of $\text{La}_2\text{O}_3\text{-M}_2\text{O}_5\text{-Li}_2\text{O}$ (M=Nb, Ta), after the XRD analysis, they considered that the structure of this compound is closely related to the garnet structure, and the space group is Ia-3d. The crystal structure of $\text{Li}_3\text{La}_3\text{M}_2\text{O}_{12}$ (M=Nb, Ta) is shown in Figure 1.5, where La occupies the X position (1/8,0,1/4), Nb or Ta occupies the Y position (0,0,0), and three Li occupies the four-coordinate position (3/8,0,1/4), the remaining 2 Li occupy the

eight -coordinate position, which is not occupied in the ideal garnet structure.

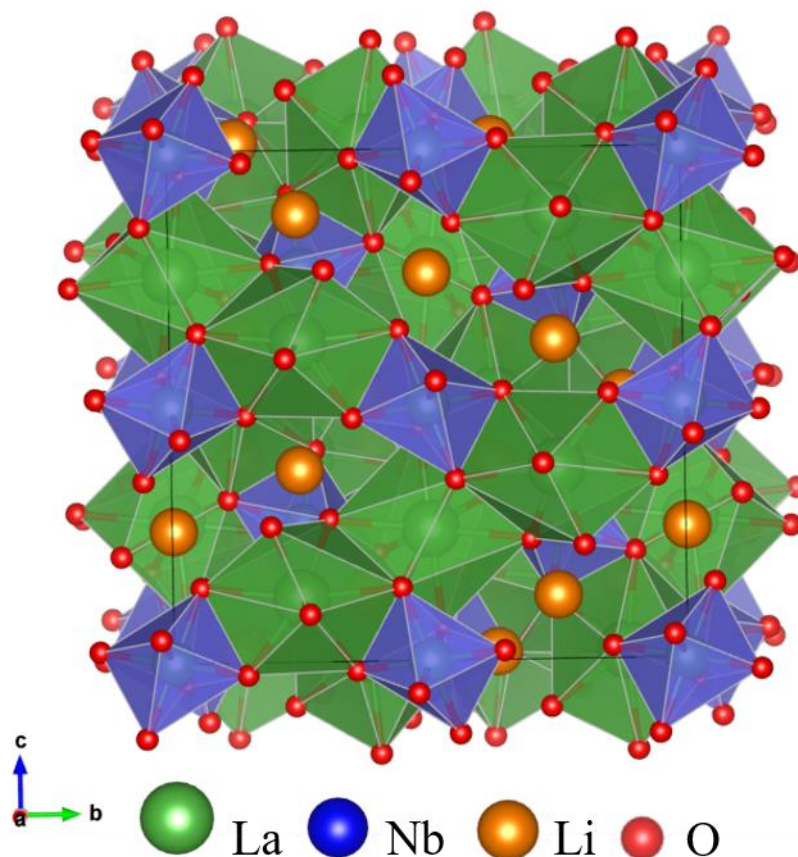


Fig 1.5 Crystal structure of cubic-type LLNO(la-3d)

Cussen⁴⁷ used neutron powder diffraction to study $\text{Li}_5\text{La}_3\text{Ta}_2\text{O}_{12}$, found that Li occupies octahedral and tetrahedral position respectively. The connection of these positions construct a three-dimensional channel for Li-ion migration. Although there are not many octahedral positions occupied by Li-ion, they are the main reason for the migration. This characteristic is common on $\text{Li}_5\text{La}_3\text{Ta}_2\text{O}_{12}$ at high temperature and $\text{Li}_5\text{La}_3\text{Nb}_2\text{O}_{12}$ at room temperature.

The study about solid electrolyte of this garnet type structure material $\text{Li}_5\text{La}_3\text{M}_2\text{O}_{12}$ (M=Nb,Ta) was first reported by Thangadurai and Weppner in 2003.⁴⁸ This material shows the typical Li-ion conductivity, and has good electrochemical and chemical stability, the room temperature conductivity is $\sim 10^{-6}$ S/cm and the activation energy is 0.43 eV ($\text{Li}_5\text{La}_3\text{Nb}_2\text{O}_{12}$) and 0.57 eV ($\text{Li}_5\text{La}_3\text{Ta}_2\text{O}_{12}$). Studies have shown that the total conductivity of the Nb system is slightly higher than that of the Ta system, but the stability of the reaction of the Ta system with molten Li is higher than that of the Nb system. There

are two main ways to improve the conductivity of this garnet structure material through doping modification, one is La-site doping, and the other is M-site doping. Using alkaline earth metal to replace the La^{3+} of $\text{Li}_5\text{La}_3\text{M}_2\text{O}_{12}$ ($\text{M}=\text{Nb}, \text{Ta}$), studies have shown that this method can well reduce the grain boundary resistance and increase the total Li ionic conductivity.^{49,50} In addition, M-site doping modification also have been reported. At present, the most research is about Zr^{4+} to replace M, which has the best ionic conductivity of Li-containing garnet structure material so far. The room temperature ionic conductivity is 3.0×10^{-4} S/cm, and the activation energy is about 0.30 eV.⁵¹ Compared with other lithium ion solid electrolyte materials, $\text{Li}_7\text{La}_3\text{Zr}_2\text{O}_{12}$ only lower than $\text{Li}_{1.3}\text{Al}_{0.3}\text{Ti}_{1.7}(\text{PO}_4)_3$ below 100 °C. as shown in Figure 1.6. Its high lithium ion conductivity can be attributed to the following points: Zr ion radius is larger than M ions, which increases the three-dimensional framework for Li-ion pathway; Increases the migration concentration of Li-ion; The interaction intensity of Li-ion with other ions is decreased; The density of ceramic samples is higher (relative density reaches 92%). The doping of alkali metals at La-site and the lower valance metal doping at M-site has also been reported.⁵² The summaries of the development of $\text{Li}_7\text{La}_3\text{M}_2\text{O}_{12}$ ($\text{M}=\text{Zr}, \text{Sn}$) garnet type solid electrolyte have shown in Table 1.4.

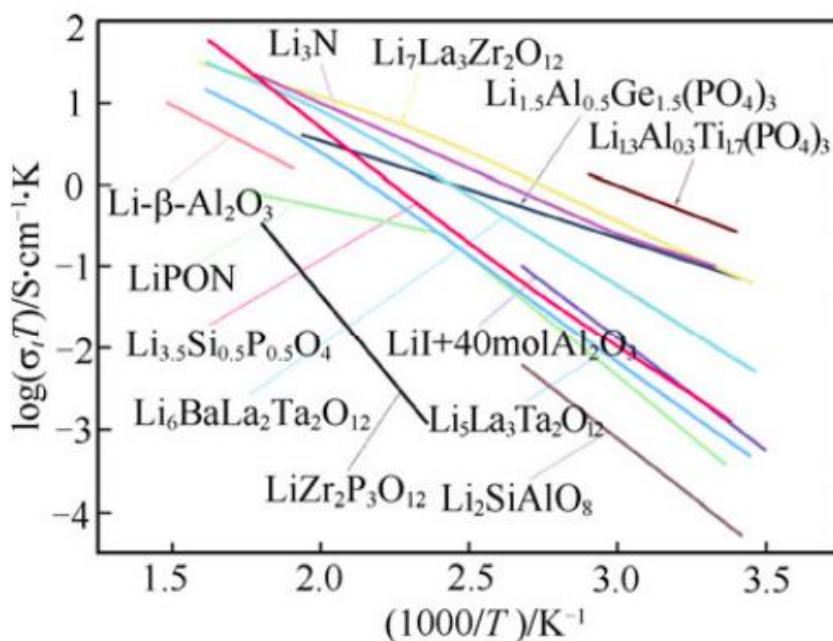


Fig 1.6 The temperature dependence of ionic conductivity of oxide lithium electrolytes and Li_3N electrolyte⁵¹

Table 1.4. Summary of $\text{Li}_7\text{La}_3\text{M}_2\text{O}_{12}$ (M=Zr, Sn) solid electrolytes

Author	Composition	Research characteristics
Weppner ⁵¹	$\text{Li}_7\text{La}_3\text{Zr}_2\text{O}_{12}$	First report this Zr series garnet structure SSI, confirmed that the space group is Ia-3d; 3.0×10^{-4} S/cm
Awaka ⁵³	$\text{Li}_7\text{La}_3\text{Zr}_2\text{O}_{12}$	Molten salt method; First report tetragonal structure of LLZ crystal with $I4_1/acd$ space group; bulk resistance 1.64×10^{-6} S/cm, gb resistance 5.59×10^{-7} S/cm; Mentioned the reason for sharp decrease in conductivity performance: The fully ordered Li atom-vacancy pair suppresses the ion jumping between Li sites. At the same time, compared with the cubic garnet structure, the equivalent Li sites of the tetragonal LLZ crystal are reduced, which ultimately leads to low Li ion conductivity.
Weppner ⁵⁴	$\text{Li}_7\text{La}_3\text{Zr}_2\text{O}_{12}$	Analyze the reason why there are two different phase structure of LLZ at room temperature: When using corundum crucible for sintering, a small amount of Al^{3+} will be doped, and the addition of Al^{3+} can keep the high temperature cubic phase structure of LLZ to room temperature.
Adams ⁵⁵	$\text{Li}_7\text{La}_3\text{Zr}_2\text{O}_{12}$	In-situ variable temperature XRD test; Tetragonal phase structure show an orderly rearrangement of lithium ions. Most of Li completely occupies the octahedral positions of 16f and 32g. Of the two types of tetrahedral positions, the 8a position is completely occupied, and the energy of the 16e octahedral position is increased.

Murugan ⁵⁶	$\text{Li}_{7.06}\text{La}_3\text{Y}_{0.06}\text{Zr}_{1.94}\text{O}_{12}$	Choose Y stable ZrO_2 (3% YSZ) as raw material; 8.1×10^{-4} S/cm
Ohta ⁵⁷	$\text{Li}_{7-x}\text{La}_3(\text{Zr}_{2-x}\text{Nb}_x)\text{O}_{12}$ ($x=0\sim 2$)	$X=0.25$, 8.0×10^{-4} S/cm, activation energy 30kJ/mol
Allen ⁵⁸	$\text{Li}_{6.75}\text{La}_3\text{Zr}_{1.75}\text{Ta}_{0.25}\text{O}_{12}$	Prepare precursor powder by co-precipitation method, hot-press sintering; 8.7×10^{-4} S/cm, 0.22 eV
Goodenough ⁵⁹	$\text{Li}_{7-x}\text{La}_3\text{Zr}_{2-x}\text{Ta}_x\text{O}_{12}$ ($x=0\sim 1$)	Alumina as a crucible; $X=0.6$, 1.0×10^{-3} S/cm; The Al element exists in the grain boundary as an amorphous phase, which acts as a sintering aid and prevents the volatilization of Li element.
Murugan ⁶⁰	$\text{Li}_{7-2x}\text{La}_3\text{Zr}_{2-x}\text{W}_x\text{O}_{12}$ ($x=0.3, 0.5$)	$X=0.3$, 7.89×10^{-4} S/cm
Murugan ⁶¹	$\text{Li}_{6.5}\text{La}_3\text{Zr}_{1.75}\text{Te}_{0.25}\text{O}_{12}$	1.03×10^{-3} S/cm; Pointed out that Li-ion stoichiometry $x \approx 6.4$ can prepare the $\text{Li}_x\text{La}_3\text{M}_2\text{O}_{12}$ with best performance at room temperature

1.4.3 Perovskite type solid-state electrolyte

Generally, the titanate of alkaline earth metals is called perovskite ATiO_3 ($A=\text{Ca}, \text{Sr}, \text{Ba}$), and the general formula can be written as ABO_3 . In 1987, Belous et al,⁶² first synthesis the perovskite structure material $\text{Li}_{0.5}\text{La}_{0.5}\text{TiO}_3$ (LLTO) by replacing the A site alkaline earth ions with the La^{3+} and monovalent alkaline earth cations ($\text{Li}^+, \text{Na}^+, \text{K}^+$). The ABO_3 cubic perovskite structure is composed of a series of oxygen shared octahedrons. The B-site ion with higher valence and smaller radius is located in the center of the oxygen octahedron, such as Ti, Sn, Zr, Nb, Ta, In. In the oxygen octahedron, is the A-site ions with a large radius, lower valence, and the coordination number is 12, such as Na, K, Rb, Ca, Sr, Ba, Pb, etc.

In the crystal structure of LLTO (as shown in Figure 1.7), LLTO belongs to the cubic crystal system and the space group is Pm-3m . Titanium ions and oxygen ions form TiO_6 octahedral structure, lithium ions and lanthanum ions are located in the gaps formed by eight co-topped TiO_6 octahedra, and Li^+ ions are surrounded by 12 O^{2-} ions.⁶³ From the

structure point of view, ionic conductivity mainly depends on the size of A-site cation, Li-ion and vacancy concentration.⁶⁴ In LLTO, Li-ion migration in the framework of material based on the ion-vacancy transition mechanism, during the migration process, Li-ion needs to pass through quadrilateral gap formed by four oxygen ions, the size of this quadrilateral gap directly affects the transition rate of lithium ions. The experimental results show that in the composition $\text{Li}_x\text{La}_{(2-x)/3}\text{TiO}_3$, the lithium ion concentration and the vacancy concentration in the framework of LLTO reach the optimal ratio, when $x=0.11$. and the grain ionic conductivity is as high as $1.43 \times 10^{-3} \text{ S/cm}$.⁶⁵

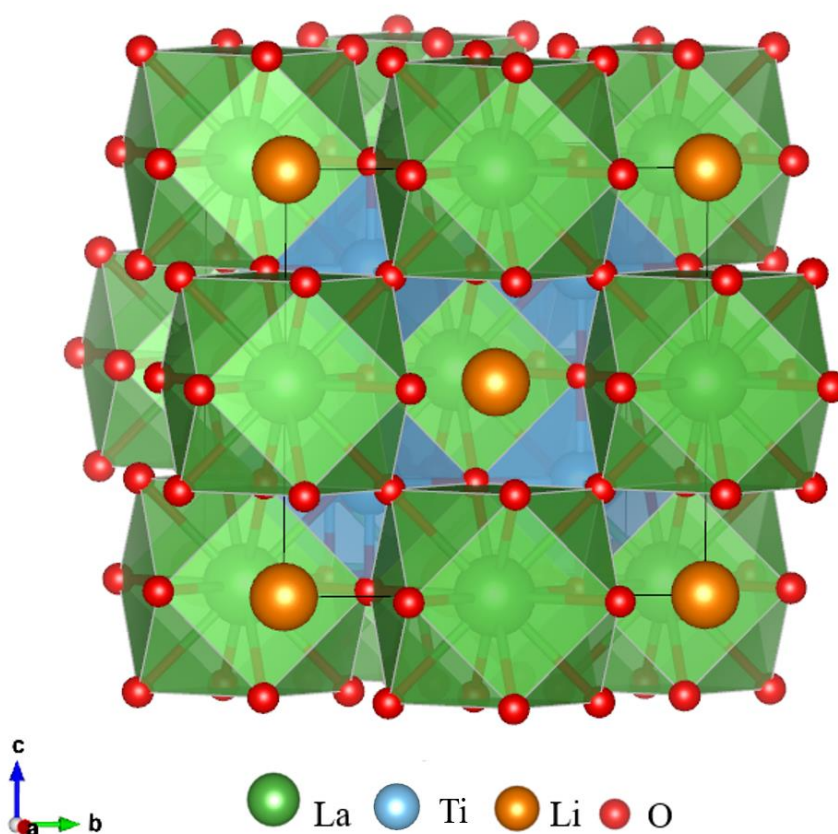


Fig 1.7 The crystal structure of LLTO

Although perovskite-type compounds have higher lithium ion conductivity, they also have certain problems. For example, Ti^{4+} is easily reduced to Ti^{3+} , which changes its electrical conductivity, and Li_2O is easily lost during the sintering process. Dionysions⁶⁶ have used Ta^{5+} instead of Ti^{4+} to obtain $\text{R}_{1/4}\text{Li}_{1/4}\text{TaO}_3$ ($\text{R}=\text{La}, \text{Nd}, \text{Sm}, \text{Y}$), but as the radius of rare earth ions decreases, the conductivity also decreases, which is mainly due

to the influence of lattice volume and A-site order. In addition, the sintering performance of these compounds usually is poor, so when prepared as a ceramic sample, its total ionic conductivity is about 2 orders of magnitude lower than its grain ionic conductivity. Therefore, how to improve its sintering performance has become a key issue in the research of such materials.⁶⁷ At present, the methods for synthesizing LLTO inorganic solid electrolyte mainly include solid-state reaction, sol-gel and other methods. When preparing LLTO, a suitable method should be selected, and factors such as the content of raw materials, sintering temperature and sintering time should be reasonably controlled, to obtain an electrolyte with stable structure and high conductivity. The various elements of substitution at the different substitute sites in the LLTO are summarized as follows: (i) A-site: The substitution of other lanthanides (Y, Dy, Gd, Sm, Nd, Pr); (ii) B-site: Other alkali (Na, K), alkaline earth (Sr, Ba) and Ag ions are substituted for the A-site of Li ion; (iii) Ti-ion are substituted by other trivalent, tetravalent, pentavalent and hexavalent ions at B-site; (iv) Co-replacement of A-site and B-site.

The summaries of the development of LLTO perovskite-type solid electrolyte have shown in Table 1.5 and Table 1.6 based on different synthesis methods and doping modification, respectively.

Table 1.5 Summary of LLTO perovskite-type solid electrolytes based on different synthesis method

Author	Composition	Research characteristics
Inaguma ⁶⁸	$\text{Li}_{0.34}\text{La}_{0.51}\text{TiO}_{2.94}$	Solid-state reaction; grain ionic conductivity 1.0×10^{-3} S/cm
Sutorik ⁶⁹	$\text{Li}_{0.29}\text{La}_{0.57}\text{TiO}_3$	Sol-gel preparation precursor, higher sintering temperature is benefit to increase the conductivity; 1100°C 6.3×10^{-5} S/cm, 900°C 3.15×10^{-5} S/cm
Romero ⁷⁰	$\text{Li}_{0.30}\text{La}_{0.57}\text{TiO}_3$	Sol-gel preparation precursor (Acetic acid medium); LLTO has a sharp cubic structure and the grain boundary conductivity reaches 1.5×10^{-5} S/cm.
Mei ⁷¹	LLTO/SiO ₂ Composite ceramics	Co-precipitation; SiO ₂ is distributed in the grain boundaries and amorphous lithium

		silicate is formed at the grain boundaries, increase the transition of Li-ion at grain boundaries. $\sim 10^{-4}$ S/cm
Laffita ⁷²	$\text{Li}_{0.5}\text{La}_{0.5}\text{TiO}_3$	Sol-gel low temperature combustion method; grain conductivity 1.33×10^{-4} S/cm, grain boundaries conductivity 7.28×10^{-10} S/cm.
Vidal ⁷³	$\text{Li}_{0.30}\text{La}_{0.57}\text{TiO}_3$	Glycine-nitrate combustion method; grain conductivity 9.0×10^{-4} S/cm

Table 1.6 Summary of LLTO perovskite-type solid electrolytes based on different doping modification

Author	Composition	Research characteristics
Teranishi ⁷⁴	$\text{Li}_{0.33}\text{Ln}_x\text{La}_{0.56-2x/3}\text{TiO}_3$ (Ln=Nd, Ba)	Grain conductivity was improved, 1.24×10^{-3} S/cm; Increase volume fraction of cubic α phase.
Teranishi ⁷⁵	$\text{Li}_{0.36}\text{Sr}_x\text{La}_{0.55-2x/3}\text{TiO}_3$	X=0.04, grain conductivity 1.24×10^{-3} S/cm; The doping of Sr can stabilize the phase as a cubic phase, increase the lattice parameter, and enlarge the lithium ion transmission bottleneck, thereby increasing the grain conductivity of the sample and reducing the activation energy of lithium ion.
Lee ⁷⁶	$(\text{Li}_{0.5-x}\text{Na}_x\text{La}_{0.5})\text{Ti}_{0.8}\text{Zr}_{0.2}\text{O}_3$ (LNTLZ)	The conductivity of the sample increases with the increase in Na content, when X=0.4, activation energy 0.56 eV
Le ⁷⁷	$(\text{Li}_{0.33}\text{La}_{0.56})_{1.005}\text{Ti}_{0.99}\text{Al}_{0.01}\text{O}_3$	Added 1 wt% Al and excess Li_2O to LLTO by sol-gel method; The sample has a tetragonal phase structure, when excess amount of Li_2O is 20%, grain conductivity 2.99×10^{-3} S/cm
Ling ⁷⁸	$\text{Li}_{0.5}\text{La}_{0.5}\text{TiO}_3 (\text{Zr}^{4+})$	Sol-gel; 4 wt% Zr^{4+} total conductivity

		5.84×10^{-5} S/cm
Okumura ⁷⁹	$\text{La}_{0.56-y}\text{Li}_{0.33}\text{TiO}_{3-3y}\text{F}_{3y}$	Adding LiF to change concentration of Li-ion and vacancy, when $y=0.017$, grain conductivity 2.30×10^{-3} S/cm
Hu ⁸⁰	$\text{Li}_{0.43}\text{La}_{0.56}\text{Ti}_{0.95}\text{Ge}_{0.05}\text{O}_3$	Adding GeO ₂ into LLTO, total conductivity 1.2×10^{-5} S/cm, Densification of solid electrolyte and improvement of structural integrity
Kawakami ⁸¹	($\text{Li}_{0.05}\text{La}_{0.317}$) ($\text{Li}_{0.1}\text{La}_{0.3}$) ($\text{Li}_{0.25}\text{La}_{0.25}$) _{1-x} M _x NbO ₃ (M= Sr, Ca)	Best composition ($\text{Li}_{0.25}\text{La}_{0.25}$) _{1-x} Sr _{0.5x} NbO ₃ , total conductivity 7.3×10^{-5} S/cm; Sr ²⁺ increase the cell volume.
Nakayama ⁸²	($\text{Li}_{0.1}\text{La}_{0.3}$) _{1+x} M _x Nb _{1-x} O ₃ (M=Zr,Ti; X=0,0.05)	The Li ⁺ migration pathway in the Zr-doped samples is subjected to contract due to the local lattice distortion around Zr-doped site

1.5 Calculation and Simulation

New energy materials are a hot spot in the development of modern science and technology, and research on battery materials is also in full swing. At the same time, the development of computer technology has made the application of first-principles calculation and molecular simulation more and more widespread. Using theoretical calculations to analyze the energy storage mechanism of battery materials can analyze the electrochemical reaction kinetics from the atomic scale, combined with high-precision experimental characterization techniques, which can often explain the relationship between structure and performance. Theoretical calculations can also be used to predict the electrochemical performance of electrode materials, or to screen suitable electrode materials from a large number of materials, without the need for complicated experiments and instrumental characterization. Using theoretical calculations to guide experiments can often save time and cost.

1.5.1 Density functional theory (DFT)

Density functional theory has a wide range of applications in the basic research of

lithium-ion batteries. It is often used to calculate the, lithium-intercalation potential, electronic/band structure, energy band, relaxation structure, defect generation energy, structural stability, , migration path, activation energy of lithium electrode materials. Ion transport kinetics and phase transition of lithium deintercalation.⁸³⁻⁸⁵ The iterative process of density functional theory calculation is shown in the Figure 1.8.

The functional methods to describe exchange-correlation interactions often used in battery material calculations include local density approximation (LDA), gradient approximation and related techniques (GGA, meta-GGA, GGA+U) and hybrid functionals (HSE06). The LDA or GGA cannot handle the relative exchange energy of electrons well. When electron transfer occurs in the calculation system, there will often be non-negligible errors. The lithium ion intercalation potential obtained by LDA and GGA is often a few tenths of electron volts lower than the actual potential.^{86,87} The self-interaction of non-local electrons in Li metal is very small, while the self-interaction of d-orbital electrons of transition metals is very large. When the non-local electrons in Li metal are transferred to the d-orbital of transition metal, the energy change is relatively large. The LDA and GGA will underestimate the energy change, thereby underestimating the reaction potential. GGA+U is a semi-empirical method, and the U value needs to be corrected by experimental values. The same element may need to use different U values in different chemical environments. So the determination of the U value is very critical.^{88,89} The meta-GGA functional SCAN can describe the mid-range van der Waals effect very well. It is better than LDA/GGA functionals in analyzing the electronic structure and unit cell parameters and predicting the stability of the structure.⁹⁰ HSE06 reduces the error of electron self-interaction energy by introducing a certain proportion of Hartree-Fock exchange energy. The calculation accuracy is higher, but the calculation amount is much larger than that of GGA and GGA+U, which requires a lot of calculation resources.⁹¹

First principles have been widely used in the research of lithium-ion battery materials. However, the calculation system is still too small. The conventional methods still have problems with applicability and calculation accuracy. Therefore, it is necessary to ensure accuracy and develop large-scale calculation software.

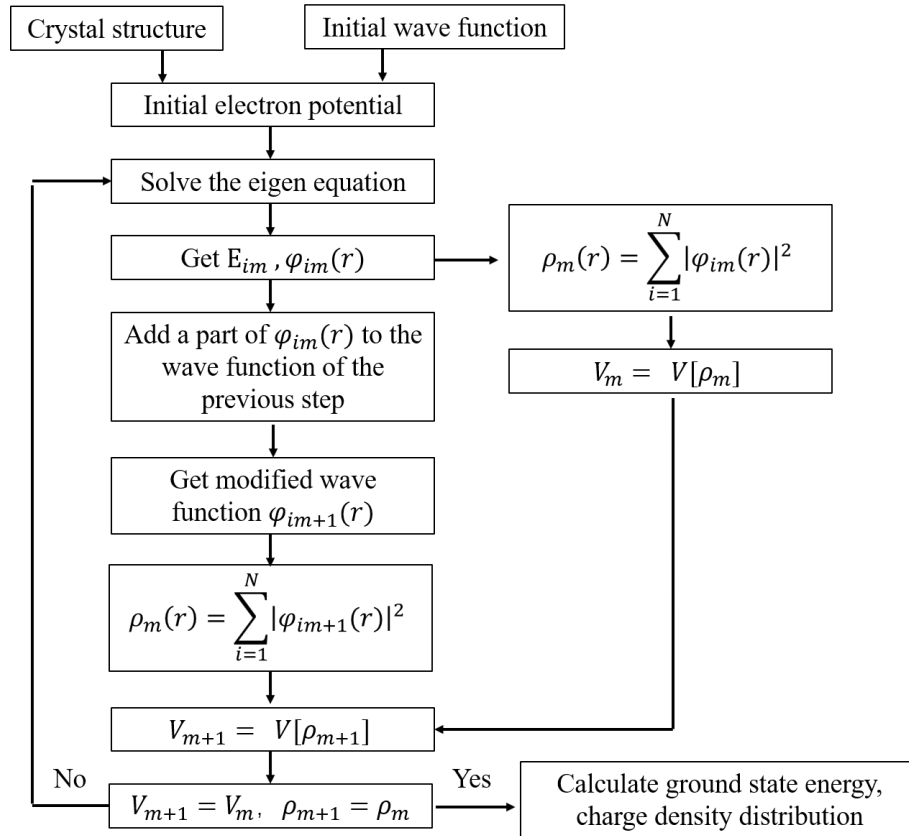


Fig 1.8 The iterative process of density functional theory calculation

1.5.2 Monte Carlo simulation

Monte Carlo method is also known as random sampling or statistical experiment method, belongs to a branch of computational mathematics and was developed in the mid-1940s in order to adapt to the atomic energy industry at that time.¹ We can use the Monte Carlo method to simulate a large number of random events that meet the laws of physics. From these random events, the values of the physical quantities that can be calculated. Some experiments are very expensive or dangerous to implement, and some physical processes are currently undetectable. Monte Carlo methods can be used to simulate the real process.

The Monte Carlo method usually uses the Metropolis algorithm for the transmission of Li-ion in solid materials. The Li-ion migration process will be considered as a Markov process. The position of each Li-ion jump is a node on the Markov chain. The success of the jump from the previous node to the next node is determined by a certain probability. The specific research ideas include two categories: (a) Simplify the process by using the classical interactions, and calculate the potential energy of Li-ions at different points

through approximate expressions. When the classical interaction is directly used for simplification, the expression of potential energy of different systems is related to the material composition. Ouyang et al,⁹² averaged the interaction between Li-Mn and Li-O to a constant in the LiMn_2O_4 system, to analyze the Li-ion diffusion behavior. (b) Obtain the potential energy through the first-principles calculation method. First-principles calculations can accurately calculate the energy of some representative atomic structures, and then use the cluster expansion method to fit the general expressions of energy and structural parameters, so as to obtain the energy of all possible structural models; then use Monte Carlo simulation to study the diffusion and transport properties of Li-ions in various complex materials. Ceder et al,⁹³ discovered the double-vacancy diffusion mechanism of Li-ion in Li_xCoO_2 . Nakayama et al^{94,95} analyze the influence of modulated arrangement cation/Vac in perovskite-type material LLMO (M=Ti, Nb) on the Li-ion migration.

The advantage of Monte Carlo simulation is that the simulation system can be very large, and it can even directly do the simulation at the real system size of material. Ouyang et al,⁹⁶ simulated the blocking effect of Cr^{4+} on Li-ion migration in LiFePO_4 with a periodic boundary system, the model is composed of $1000 \times 1000 \times 1000$ unit cell, this model size is on the same order of magnitude of real LiFePO_4 particle size.

1.5.3 Molecular Dynamics (MD)

The molecular dynamics method is a deterministic simulation method. The basic idea is to describe the motion of particles by solving the Newtonian equation of motion. Under a given potential field, the initial position and velocity of the particles in the system are known. The force and acceleration can be determined by solving the equation of motion, and finally the position, velocity and acceleration of each particle can be obtained over time. In the process of calculating lithium ion diffusion behavior, molecular dynamics includes classical molecular dynamics and first-principles molecular dynamics.⁹⁷⁻¹⁰⁰

The classical molecular dynamics method is limited by the observation time and the size of the simulation system. It is necessary to introduce boundary conditions such as periodic boundary, total (diffuse) reflection boundary, and open boundary. For Li-ion diffusion behavior in lithium ion battery materials, to calculate the diffusion coefficient at a certain temperature, the suitable ensemble (NVT/NPT/NET) should be considered.

Applying molecular dynamics to simulate the diffusion behavior, the most important thing is to construct a model that can accurately describe the potential field of the particles, and then calculate the precise force of the particles. For solid-state materials, it is still difficult to construct the model that can perfectly describes the force field of particles.¹⁰¹

The basic idea of first-principles molecular dynamics simulation is to use the first-principles method to calculate the force between atoms, and then to calculate the atomic motion through the molecular dynamics method, and the motion of atoms and electrons were consider separately.

In terms of the size of the simulation system, the number of atoms that can reach several thousand and even hundreds of thousands for the large-scale calculations by using classical molecular dynamics. Although, First-principles molecular dynamics simulation can obtain more accurate results, the simulation system is relatively small (within a few hundred). From the perspective of simulation time, the time scales that can be simulated by classical molecular dynamics are usually on the order of nanoseconds, and some can even reach the order of microseconds. The time scales of first-principles molecular dynamics simulations are only on the order of picoseconds, which limits this method on the diffusion mechanism level, and cannot truly study the diffusion behavior of the actual battery system.

Molecular dynamics can not only reveal the movement path and energy barrier in the self-diffusion process in materials, but also allow us to understand the diffusion mechanism with higher degree of freedom. Many achievements have been reported in the field of lithium battery materials via MD simulation. The structural defect characteristic and ion migration properties of {cathode materials (spinel manganese oxide,¹⁰² olivine phosphate,^{103–107} silicate,^{108,109} tavorite¹¹⁰); anode materials^{111,112} ; electrolytes(nasicon-type,^{113–115} garnet-type,^{13,116} perovskite-type,^{16,95} Sulfide^{117–119})} for Li-ion battery has been investigated. With the development of a series of simulation techniques such as molecular dynamics simulation, the research on solid electrolyte interfacial (SEI) membranes has also made considerable progress. Y.Qi et al,¹²⁰ summarized the design of SEI films, and gave a detailed overview of the formation process, principles and modification methods of SEI. Takenaka et al,¹²¹ developed a new method which combines MC (reaction energy calculated by DFT) with MD (classical force field) to observed a nano-thick SEI film with a two-layer structure, this method overcomes the time and length

scale of SEI formation, successfully.

1.5.4 High-throughput computing and data mining

Beginning in 2010, Ceder et al, has carried out a research project called genetic engineering of lithium-ion battery materials. They have developed a data platform for material performance calculation, data generation, and data analysis. The polyanion XO_4 ($X=P, S, As, Si$) compound is replaced with other elements to synthesize new compounds, and new materials are screened by evaluating parameters such as energy density, voltage, and cell volume after removing Li.¹²² In addition, based on the Sidorenkite structure, more than 270 components and structures are constructed, several candidate Li_3MnX ($X=CO_3, PO_4$), Li_2VX ($X=CO_3, PO_4$), Li_3VX ($X=CO_3, SiO_4$) are screened out.¹²³⁻¹²⁵ They also screened compounds of various transition metals and Li containing (P_mO_n) anion groups by the similar methods.¹²⁶ Tanaka et al,^{127,128} analyzed the ion transport of LISICON-type material by combining first-principles molecular dynamics simulation with machine learning technology. It can effectively predict the ionic conductivity with different components of $LiO_{1/2}AO_{m/2}BO_{n/2}$ LISICON system, accelerated the development of solid electrolytes.

The high-throughput calculation methods used in the above research work all have the common characteristics shown in Figure 1.9. First input selected data from the external structural database, generate input files that can be called by calculation software, and calculate the corresponding property data of the material, and save the calculation results to the database for further analysis. The new knowledge obtained can expand the original database, and help more accurate data selection. In conclusion, to establish a set of programmed high-throughput calculation platform, linking various calculation software packages, single-function calculation programs or instructions (such as input file generation &, material property simulation, result analysis program, etc.) with computing hardware equipment, etc., so that the entire process can be completed automatically, is the key to achieving high-throughput computing and improving overall efficiency. The calculation process designed by the Ceder's team which mentioned above, realized the automatic call function of the crystal structure database and the first-principles calculation program VASP, so as to obtain thermodynamic data such as the formation energy of the material and the information of the electronic structure through high-throughput calculations. However, since the attention properties of material is often different, the

material database, simulation method, and analysis method that you want to use may differ. Therefore, it is necessary to design corresponding software for various materials to achieve specific Automated calculation process.

At present, there are still the following problems in the high-throughput screening of lithium battery materials: (1) The emphasis is on the thermodynamic properties of materials, such as the calculation of formation energy and thermal stability, and the lack of consideration of the important kinetic performance of lithium ion transport (2) The constraints used in screening are not targeted and hierarchical, causing a lot of repetition and unnecessary calculations; (3) Most calculations are based on first-principles methods based on density functionals, which have not yet been combined with other more Calculation method or software; (4) The large amount of data obtained by calculation has not yet been effectively mined. In fact, the performance of the material is completely determined by two factors: the structure and composition of the material. Through large-scale calculations, the connection between the structure, composition and material properties of the material is unearthed. Constructing the (structure-activity relationship) of materials is also one of the important goals of high-throughput calculations. Through the establishment of targeted external constraints for the screening process, including application requirements, basic physical laws, temperature and pressure, and other external conditions, the material composition and structure model are constructed. High-throughput computing technology is used to calculate the various properties of the compounds corresponding to these structural models, and feed them back to the structural performance database, which is used to study the physical problems in lithium battery materials, and at the same time screen out materials that meet the application constraints. And through various experimental methods to prepare these materials, and then test and characterize the physical and chemical properties of these materials, and finally achieve the purpose of understanding the physical problems of lithium battery materials and discovering new materials. It is foreseeable that in the next few years, the application of high-throughput calculation methods, combined with experimental research, will greatly accelerate our research and development of lithium battery materials, and deepen our understanding of various problems in lithium batteries. Reveal the structure-performance relationship and intrinsic physics of materials Laws, thereby shortening the entire process of materials from research and development to application.

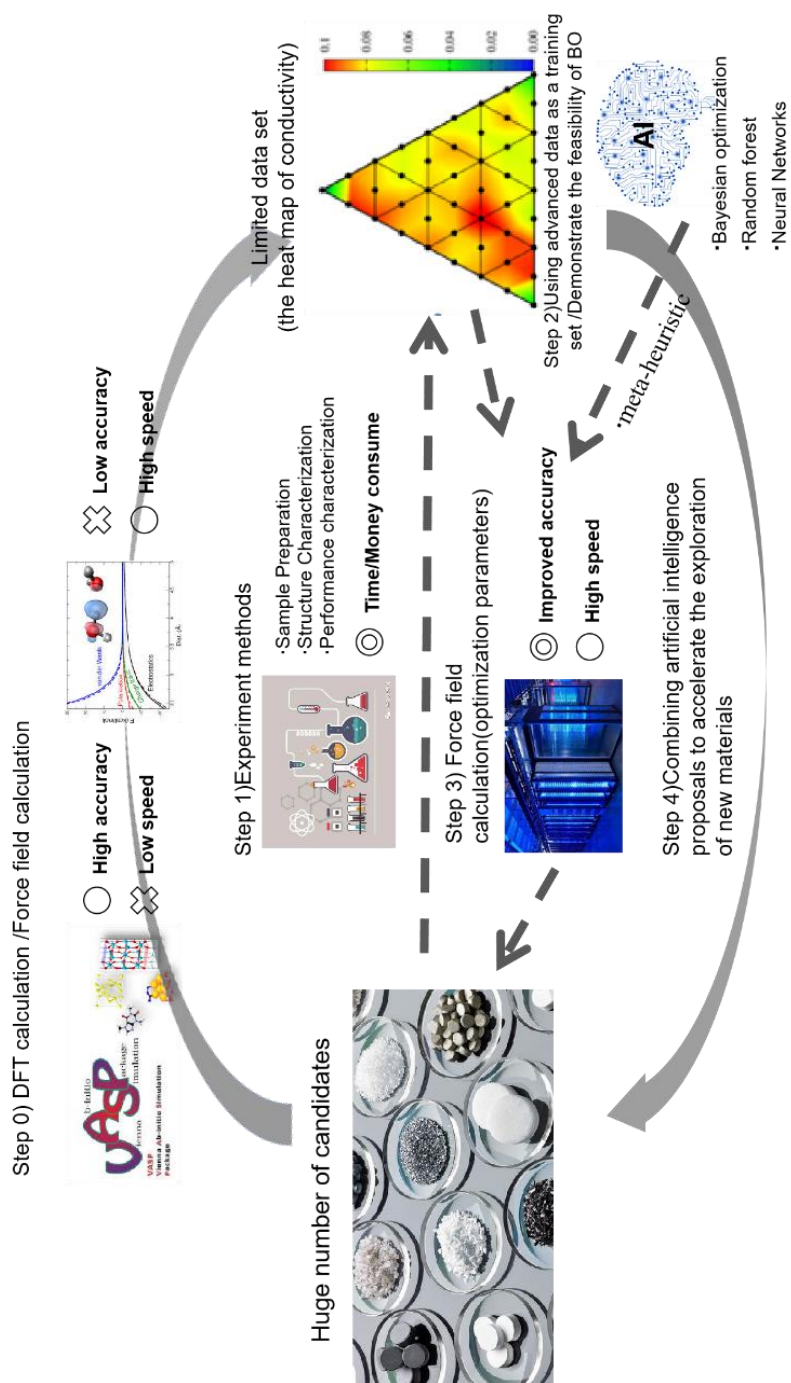


Fig 1.9 Data flow diagram for high-throughput computational screening of materials

1.6 The purpose of this work

To develop better performance battery device, obtained new material with specific function and outstanding performance is necessary, solid-state electrolyte as a very important part of all solid-state Li-ion battery still has some unsolved problems need to be conquered. Obtaining the knowledge of the ion conduction mechanism in the solid material is a very important path to improve the related researches. In this thesis, lanthanum lithium niobite (LLNO), a perovskite-type LLNO derivative introduced in section 1.4.3, is focused as a n attractive candidate for fast Li-ion conductor, since this series of materials has many structural advantages compared with LLTO, it has higher concentration of cation vacancy sites, and larger lattice volume than LLTO, which are interesting structural advantages, supposed to form effective Li-ion migration path-way. The structure and property details will be introduced at the head of Chapter 2 of this thesis.

The unrevealed atomic arrangement of Li/cation/vacancy in LLNO is the key to solve this problem. We hope to link the atomic crystal structure with physical properties such as ion diffusivity, it is expected to be a powerful method for other type solid-state electrolytes, and guide research to design new material.

In Chapter 2, we used DFT calculation combined with cluster expansion (CE) and Monte Carlo (MC) simulation in multiple scale to reveal the possible modulated arrangement of cation/vacancy of LLNO and dictated the available pathways for Li-ion.

In Chapter 3, we adopt DFT-derived force field molecular dynamics (FFMD) simulation via a metaheuristic approach to investigate the migration behavior of Li-ion in LLNO with specific modulated structure.

In Chapter 4, we used conventional experimental method to dope modified the properties of LLNO, except for the experimental part, as an extended exploration of proof-of-concept. Our computational simulations proved that the Bayesian optimization (BO) method can effectively search for the best material composition, so material retrieval during the exploration period can benefit from BO. This has guiding significance for the traditional materials industry that explores new materials through trial and error.

Reference

1. Metropolis, N. & Ulam, S. The Monte Carlo Method. *Journal of the American Statistical Association* **44**, 335–341 (1949).
2. Dynamics, M. 第四章 分子动力学方法. 1–15 (1814).
3. Bogdanova, M. *et al.* Simulation platform for multiscale and multiphysics modeling of OLEDs. *Procedia Computer Science* **29**, 740–753 (2014).
4. Megahed, S. & Scrosati, B. Lithium-ion rechargeable batteries. *Journal of Power Sources* **51**, 79–104 (1994).
5. Sarkar, S. & Jou, Y. C. Adaptive Control of the Reverse Link in cdma2000. *International Journal of Wireless Information Networks* **9**, 55–70 (2002).
6. Tarascon, J. M. & Guyomard, D. The $\text{Li}_{1+x}\text{Mn}_2\text{O}_4/\text{C}$ rocking-chair system: a review. *Electrochimica Acta* **38**, 1221–1231 (1993).
7. Zheng, F., Kotobuki, M., Song, S., Lai, M. O. & Lu, L. Review on solid electrolytes for all-solid-state lithium-ion batteries. *Journal of Power Sources* **389**, 198–213 (2018).
8. Oudenhoven, J. F. M., Baggetto, L. & Notten, P. H. L. All-solid-state lithium-ion microbatteries: A review of various three-dimensional concepts. *Advanced Energy Materials* **1**, 10–33 (2011).
9. Takada, K. Progress and prospective of solid-state lithium batteries. *Acta Materialia* **61**, 759–770 (2013).
10. Yue-Lei, Z., Ren-Jie, C., Feng, W. & Li, L. Progress of research on the conductive mechanism of the glassy electrolytes in lithium ion batteries. *Journal of Inorganic Materials* **28**, 1172–1180 (2013).
11. Sakuda, A., Hayashi, A. & Tatsumisago, M. Sulfide solid electrolyte with favorable mechanical property for all-solid-state lithium battery. *Scientific Reports* **3**, 2–6 (2013).
12. Tatsumisago, M., Nagao, M. & Hayashi, A. Recent development of sulfide solid electrolytes and interfacial modification for all-solid-state rechargeable lithium batteries. *Journal of Asian Ceramic Societies* **1**, 17–25 (2013).
13. Science, E. S. Research progress of inorganic solid electrolytes in foundmental and application field. (2015). doi:10.3969/j.issn.2095-4239.2015.01.001
14. Zhao, Y. *et al.* A promising PEO/LAGP hybrid electrolyte prepared by a simple method for all-solid-state lithium batteries. *Solid State Ionics* **295**, 65–71 (2016).
15. Zhang, N., He, J., Han, W. & Wang, Y. Composite solid electrolyte PEO/SN/LiAlO₂ for a solid-state lithium battery. *Journal of Materials Science* **54**, 9603–9612 (2019).
16. Wu, J. *et al.* A review on structural characteristics, lithium ion diffusion behavior and temperature dependence of conductivity in perovskite-type solid electrolyte $\text{Li}_3\text{xLa}_{2-3-x}\text{TiO}_3$. *Functional Materials Letters* **10**, 1730002 (2017).
17. Luo, W. *et al.* Transition from Superlithiophobicity to Superlithiophilicity of Garnet Solid-State Electrolyte. *Journal of the American Chemical Society* **138**, 12258–12262 (2016).
18. Thangadurai, V., Narayanan, S. & Pinzaru, D. Garnet-type solid-state fast Li ion conductors for Li batteries: Critical review. *Chemical Society Reviews* **43**, 4714–4727 (2014).
19. Minami, T. *Solid state ionics for batteries.* (Springer Science & Business Media, 2006).
20. Hagman, L.-O., Kierkegaard, P., Karvonen, P., Virtanen, A. I. & Paasivirta, J. The Crystal Structure of

- $\text{NaM}_2\text{IV}(\text{PO}_4)_3$; MeIV = Ge, Ti, Zr. *Acta Chemica Scandinavica* **22**, 1822–1832 (1968).
21. Goodenough, J. B., Hong, H. Y. & Kafalas, J. A. J. B. Goodenough, H. Y-P. **I**, 203–220 (1976).
 22. Fergus, J. W. Ceramic and polymeric solid electrolytes for lithium-ion batteries. *Journal of Power Sources* **195**, 4554–4569 (2010).
 23. Thangadurai, V. & Weppner, W. Recent progress in solid oxide and lithium ion conducting electrolytes research. *Ionics* **12**, 81–92 (2006).
 24. Hao, Z., Jian, G. A. O., Shaofei, W. & Hong, L. I. Fundamental scientific aspects of lithium batteries (VI)--Ionic transport in solids. *Energy Storage Science and Technology* **2**, 620 (2013).
 25. Aono, H., Sugimoto, E., Sadaoka, Y., Imanaka, N. & Adachi, G. Ionic Conductivity of Solid Electrolytes Based on Lithium Titanium Phosphate. *Journal of The Electrochemical Society* **137**, 1023–1027 (1990).
 26. Chowdari, B. V. R., Subba Rao, G. V. & Lee, G. Y. H. XPS and ionic conductivity studies on $\text{Li}_2\text{O}-\text{Al}_2\text{O}_3$ - $(\text{TiO}_2 \text{ or } \text{GeO}_2)$ - P_2O_5 glass-ceramics. *Solid State Ionics* **136–137**, 1067–1075 (2000).
 27. Leo, C. J., Chowdari, B. V. R., Rao, G. V. S. & Souquet, J. L. Lithium conducting glass ceramic with Nasicon structure. *Materials Research Bulletin* **37**, 1419–1430 (2002).
 28. Gao, Z. *et al.* Promises, Challenges, and Recent Progress of Inorganic Solid-State Electrolytes for All-Solid-State Lithium Batteries. *Advanced Materials* **30**, 1705702 (2018).
 29. Kotobuki, M., Hoshina, K., Isshiki, Y. & Kanamura, K. PREPARATION OF $\text{Li}_{1.5}\text{Al}_{0.5}\text{Ge}_{1.5}(\text{PO}_4)_3$ SOLID ELECTROLYTE BY SOL-GEL METHOD. *Phosphorus Research Bulletin* **25**, 61–63 (2011).
 30. Duluard, S. *et al.* Lithium conducting solid electrolyte $\text{Li}_{1.3}\text{Al}_{0.3}\text{Ti}_{1.7}(\text{PO}_4)_3$ obtained via solution chemistry. *Journal of the European Ceramic Society* **33**, 1145–1153 (2013).
 31. Xu, X., Wen, Z., Yang, X. & Chen, L. Dense nanostructured solid electrolyte with high Li-ion conductivity by spark plasma sintering technique. *Materials Research Bulletin* **43**, 2334–2341 (2008).
 32. XIAO, Z., CHEN, S. & GUO, M. Influence of Li_3PO_4 addition on properties of lithium ion-conductive electrolyte $\text{Li}_{1.3}\text{Al}_{0.3}\text{Ti}_{1.7}(\text{PO}_4)_3$. *Transactions of Nonferrous Metals Society of China* **21**, 2454–2458 (2011).
 33. Aono, H., Sugimoto, E., Sadaoka, Y., Imanaka, N. & Adachi, G. The Electrical Properties of Ceramic Electrolytes for $\text{LiM}_x\text{Ti}_{2-x}(\text{PO}_4)_3 + y\text{Li}_2\text{O}$, M = Ge, Sn, Hf, and Zr Systems. *Journal of The Electrochemical Society* **140**, 1827–1833 (1993).
 34. Zhang, P. *et al.* Water-stable lithium ion conducting solid electrolyte of the $\text{Li}_{1.4}\text{Al}_{0.4}\text{Ti}_{1.6-x}\text{Ge}_x(\text{PO}_4)_3$ system ($x=0-1.0$) with NASICON-type structure. *Solid State Ionics* **253**, 175–180 (2013).
 35. Morimoto, H. *et al.* Preparation of lithium ion conducting solid electrolyte of NASICON-type $\text{Li}_{1+x}\text{Al}_x\text{Ti}_{2-x}(\text{PO}_4)_3$ ($x = 0.3$) obtained by using the mechanochemical method and its application as surface modification materials of LiCoO_2 cathode for lithium cell. *Journal of Power Sources* **240**, 636–643 (2013).
 36. Xu, X., Wen, Z., Yang, X., Zhang, J. & Gu, Z. High lithium ion conductivity glass-ceramics in $\text{Li}_2\text{O}-\text{Al}_2\text{O}_3$ - TiO_2 - P_2O_5 from nanoscaled glassy powders by mechanical milling. *Solid State Ionics* **177**, 2611–2615 (2006).
 37. Johnson, P., Sammes, N., Imanishi, N., Takeda, Y. & Yamamoto, O. Effect of microstructure on the conductivity of a NASICON-type lithium ion conductor. *Solid State Ionics* **192**, 326–329 (2011).
 38. Kumar, B. & Thokchom, J. S. Space Charge Signature and Its Effects on Ionic Transport in Heterogeneous Solids. *Journal of the American Ceramic Society* **90**, 3323–3325 (2007).
 39. Fu, J. Fast Li^+ ion conducting glass-ceramics in the system $\text{Li}_2\text{O}-\text{Al}_2\text{O}_3$ - GeO_2 - P_2O_5 . *Solid State Ionics* **104**, 191–194 (1997).

-
40. Kun, H. *et al.* Influence of Al₂O₃ additions on crystallization mechanism and conductivity of Li₂O–Ge₂O–P₂O₅ glass–ceramics. *Physica B: Condensed Matter* **406**, 3947–3950 (2011).
 41. Fu, J. Effects of M³⁺ Ions on the Conductivity of Glasses and Glass–Ceramics in the System Li₂O—M₂O₃—GeO₂—P₂O₅ (M = Al, Ga, Y, Dy, Gd, and La). *Journal of the American Ceramic Society* **83**, 1004–1006 (2000).
 42. KATOH, T., INDA, Y., BABA, M. & YE, R. Lithium-ion conductive glass-ceramics with composition ratio control and their electrochemical characteristics. *Journal of the Ceramic Society of Japan* **118**, 1159–1162 (2010).
 43. Xu, X., Wen, Z., Wu, X., Yang, X. & Gu, Z. Lithium Ion-Conducting Glass–Ceramics of Li_{1.5}Al_{0.5}Ge_{1.5}(PO₄)_{3–x}Li₂O (x=0.0–0.20) with Good Electrical and Electrochemical Properties. *Journal of the American Ceramic Society* **90**, 2802–2806 (2007).
 44. Jadhav, H. S. *et al.* Influence of B₂O₃ addition on the ionic conductivity of Li_{1.5}Al_{0.5}Ge_{1.5}(PO₄)₃ glass ceramics. *Journal of Power Sources* **241**, 502–508 (2013).
 45. Thokchom, J. S., Gupta, N. & Kumar, B. Superionic Conductivity in a Lithium Aluminum Germanium Phosphate Glass–Ceramic. *Journal of The Electrochemical Society* **155**, A915 (2008).
 46. Kasper, H. M. Series of rare earth garnets Ln₃+ 3M₂Li+ 3O₁₂ (M= Te, W). *Inorganic Chemistry* **8**, 1000–1002 (1969).
 47. Cussen, E. J. The structure of lithium garnets: Cation disorder and clustering in a new family of fast Li+ conductors. *Chemical Communications* 412–413 (2006). doi:10.1039/b514640b
 48. Thangadurai, V., Kaack, H. & Weppner, W. J. F. Novel fast lithium ion conduction in garnet-type Li₅La₃M₂O₁₂ (M = Nb, Ta). *Journal of the American Ceramic Society* **86**, 437–440 (2003).
 49. Thangadurai, V. & Weppner, W. Li₆Ala₂Ta₂O₁₂ (A = Sr, Ba): Novel Garnet-Like Oxides for Fast Lithium Ion Conduction. *Advanced Functional Materials* **15**, 107–112 (2005).
 50. Thangadurai, V. & Weppner, W. Li₆Ala₂Nb₂O₁₂ (A=Ca, Sr, Ba): A New Class of Fast Lithium Ion Conductors with Garnet-Like Structure. *Journal of the American Ceramic Society* **88**, 411–418 (2005).
 51. Murugan, R., Thangadurai, V. & Weppner, W. Fast lithium ion conduction in garnet-type Li₇La₃Zr₂O₁₂. *Angewandte Chemie - International Edition* **46**, 7778–7781 (2007).
 52. Thangadurai, V. & Weppner, W. Effect of sintering on the ionic conductivity of garnet-related structure Li₅La₃Nb₂O₁₂ and In- and K-doped Li₅La₃Nb₂O₁₂. *Journal of Solid State Chemistry* **179**, 974–984 (2006).
 53. Awaka, J., Kijima, N., Hayakawa, H. & Akimoto, J. Synthesis and structure analysis of tetragonal Li₇La₃Zr₂O₁₂ with the garnet-related type structure. *Journal of Solid State Chemistry* **182**, 2046–2052 (2009).
 54. Geiger, C. A. *et al.* Crystal chemistry and stability of ‘Li₇La₃Zr₂O₁₂’ garnet: A fast lithium-ion conductor. *Inorganic Chemistry* **50**, 1089–1097 (2011).
 55. Adams, S. & Rao, R. P. Ion transport and phase transition in Li_{7–x}La₃(Zr_{2–x}M_x)O₁₂ (M = Ta⁵⁺, Nb⁵⁺, x = 0, 0.25). *Journal of Materials Chemistry* **22**, 1426–1434 (2012).
 56. Murugan, R., Ramakumar, S. & Janani, N. High conductive yttrium doped Li₇La₃Zr₂O₁₂ cubic lithium garnet. *Electrochemistry Communications* **13**, 1373–1375 (2011).
 57. Ohta, S., Kobayashi, T. & Asaoka, T. High lithium ionic conductivity in the garnet-type oxide Li_{7–X}La₃(Zr_{2–X}, Nb_X)O₁₂ (X=0–2). *Journal of Power Sources* **196**, 3342–3345 (2011).
 58. Allen, J. L., Wolfenstine, J., Rangasamy, E. & Sakamoto, J. Effect of substitution (Ta, Al, Ga) on the

- conductivity of $\text{Li}_7\text{La}_3\text{Zr}_2\text{O}_{12}$. *Journal of Power Sources* **206**, 315–319 (2012).
59. Li, Y., Han, J. T., Wang, C. A., Xie, H. & Goodenough, J. B. Optimizing Li^+ conductivity in a garnet framework. *Journal of Materials Chemistry* **22**, 15357–15361 (2012).
 60. Dhivya, L., Janani, N., Palanivel, B. & Murugan, R. Li^+ transport properties of W substituted $\text{Li}_7\text{La}_3\text{Zr}_2\text{O}_{12}$ cubic lithium garnets. *AIP Advances* **3**, (2013).
 61. Deviannapoorani, C., Dhivya, L., Ramakumar, S. & Murugan, R. Lithium ion transport properties of high conductive tellurium substituted $\text{Li}_7\text{La}_3\text{Zr}_2\text{O}_{12}$ cubic lithium garnets. *Journal of Power Sources* **240**, 18–25 (2013).
 62. Belous, A., Novitskaya, G., Polyanetskaya, S. & Gornikov, Y. Study of complex oxides with the composition $\text{La}_{2/3-x}\text{Li}_x\text{TiO}_3$. *Inorg. Mater. (Engl. Transl.)*; (United States) **23**:3, 412 (1987).
 63. Nakayama, M., Ikuta, H., Uchimoto, Y. & Wakihara, M. Ionic conduction of lithium in B-site substituted perovskite compounds, $(\text{Li}_{0.1}\text{La}_{0.3})\text{M}_x\text{Nb}_{1-x}\text{O}_3$ ($\text{M} = \text{Zr, Ti, Ta}$). *Journal of Materials Chemistry* **12**, 1500–1504 (2002).
 64. Stramare, S., Thangadurai, V. & Weppner, W. Lithium Lanthanum Titanates: A Review. *Chemistry of Materials* **15**, 3974–3990 (2003).
 65. Yashima, M., Itoh, M., Inaguma, Y. & Morii, Y. Crystal structure and diffusion path in the fast lithium-ion conductor $\text{La}_{0.62}\text{Li}_{0.16}\text{TiO}_3$. *Journal of the American Chemical Society* **127**, 3491–3495 (2005).
 66. Dionysiou, D., Qi, X., Lin, Y. S., Meng, G. & Peng, D. Preparation and characterization of proton conducting terbium doped strontium cerate membranes. *Journal of Membrane Science* **154**, 143–153 (1999).
 67. Stramare, S., Thangadurai, V. & Weppner, W. Lithium Lanthanum Titanates: A Review. *Chemistry of Materials* **15**, 3974–3990 (2003).
 68. Inaguma, Y. *et al.* High ionic conductivity in lithium lanthanum titanate. *Solid State Communications* **86**, 689–693 (1993).
 69. Sutorik, A. C., Green, M. D., Cooper, C., Wolfenstine, J. & Gilde, G. The comparative influences of structural ordering, grain size, Li-content, and bulk density on the Li^+ -conductivity of $\text{Li}_{0.29}\text{La}_{0.57}\text{TiO}_3$. *Journal of Materials Science* **47**, 6992–7002 (2012).
 70. Romero, M., Faccio, R., Vázquez, S., Davyt, S. & Mombrú, Á. W. Experimental and theoretical Raman study on the structure and microstructure of $\text{Li}_{0.30}\text{La}_{0.57}\text{TiO}_3$ electrolyte prepared by the sol-gel method in acetic medium. *Ceramics International* **42**, 15414–15422 (2016).
 71. Mei, A. *et al.* Enhanced ionic transport in lithium lanthanum titanium oxide solid state electrolyte by introducing silica. *Solid State Ionics* **179**, 2255–2259 (2008).
 72. Pérez Cappe, E., Aranda, P. & Mosqueda Laffita, Y. Influence of citrate/nitrate ratio on the preparation of $\text{Li}_{0.5}\text{La}_{0.5}\text{TiO}_3$ nanopowder by combustion method. (2014).
 73. Vidal, K. *et al.* Effects of synthesis conditions on the structural, stability and ion conducting properties of $\text{Li}_{0.30}(\text{La}_{0.50}\text{Ln}_{0.50})_{0.567}\text{TiO}_3$ ($\text{Ln} = \text{La, Pr, Nd}$) solid electrolytes for rechargeable lithium batteries. *Ceramics International* **40**, 8761–8768 (2014).
 74. Teranishi, T., Yamamoto, M., Hayashi, H. & Kishimoto, A. Lithium ion conductivity of Nd-doped (Li, La) TiO_3 ceramics. *Solid State Ionics* **243**, 18–21 (2013).
 75. Teranishi, T., Kouchi, A., Hayashi, H. & Kishimoto, A. Dependence of the conductivity of polycrystalline $\text{Li}_{0.33}\text{Ba}_x\text{La}_{0.56-2/3x}\text{TiO}_3$ on Ba loading. *Solid State Ionics* **263**, 33–38 (2014).

-
76. Lee, S. *et al.* Ceramics as Improved Electrolyte Materials for Li-ion Batteries. **15**, 96–99 (2014).
 77. Le, H. T. T. *et al.* Citrate gel synthesis of aluminum-doped lithium lanthanum titanate solid electrolyte for application in organic-type lithium–oxygen batteries. *Journal of Power Sources* **274**, 1188–1199 (2015).
 78. Ling, M., Zhu, X., Jiang, Y. & Zhu, J. Comparative study of solid-state reaction and sol-gel process for synthesis of Zr-doped $\text{Li}_{0.5}\text{La}_{0.5}\text{TiO}_3$ solid electrolytes. *Ionics* **22**, 2151–2156 (2016).
 79. Okumura, T. *et al.* Improvement of Li-ion conductivity in A-site disordering lithium-lanthanum-titanate perovskite oxides by adding LiF in synthesis. *Journal of Power Sources* **189**, 536–538 (2009).
 80. Hu, Z. *et al.* Enhanced Li ion conductivity in Ge-doped $\text{Li}_{0.33}\text{La}_{0.56}\text{TiO}_3$ perovskite solid electrolytes for all-solid-state Li-ion batteries. *New Journal of Chemistry* **42**, 9074–9079 (2018).
 81. Kawakami, Y., Fukuda, M., Ikuta, H. & Wakihara, M. Ionic conduction of lithium for perovskite type compounds, $(\text{Li}_{0.05}\text{La}_{0.317})_{1-x}\text{Sr}_{0.5x}\text{NbO}_3$, $(\text{Li}_{0.1}\text{La}_{0.3})_{1-x}\text{Sr}_{0.5x}\text{NbO}_3$ and $(\text{Li}_{0.25}\text{La}_{0.25})_{1-x}\text{M}_{0.5x}\text{NbO}_3$ (M = Ca and Sr). *Solid State Ionics* **110**, 187–192 (1998).
 82. Nakayama, M., Ikuta, H., Uchimoto, Y., Wakihara, M. & Terada, Y. Relationship between the Li ionic conduction and the local structures in B-site substituted perovskite compounds, $(\text{Li}_{0.1}\text{La}_{0.3})_{1+x}\text{M}_x\text{Nb}_{1-x}\text{O}_3$ (M=Zr, Ti; X=0, 0.05). *Applied Physics Letters* **81**, 2977–2979 (2002).
 83. Tianran, Z., Daixin, L., Tao, Z. & Jun, C. Understanding electrode materials of rechargeable lithium batteries via DFT calculations. *Progress in Natural Science: Materials International* **23**, 256–272 (2013).
 84. Park, J. H., Liu, T., Kim, K. C., Lee, S. W. & Jang, S. S. Systematic Molecular Design of Ketone Derivatives of Aromatic Molecules for Lithium-Ion Batteries: First-Principles DFT Modeling. *ChemSusChem* **10**, 1584–1591 (2017).
 85. Adekoya, D. *et al.* *DFT-Guided Design and Fabrication of Carbon-Nitride-Based Materials for Energy Storage Devices: A Review*. *Nano-Micro Letters* **13**, (Springer Singapore, 2021).
 86. Zhou, F., Cococcioni, M., Kang, K. & Ceder, G. The Li intercalation potential of LiMPO_4 and LiMSiO_4 olivines with M=Fe, Mn, Co, Ni. *Electrochemistry Communications* **6**, 1144–1148 (2004).
 87. Himmetoglu, B., Floris, A., de Gironcoli, S. & Cococcioni, M. Hubbard-corrected DFT energy functionals: The LDA+U description of correlated systems. *International Journal of Quantum Chemistry* **114**, 14–49 (2014).
 88. Wu, S. Q., Zhu, Z. Z., Yang, Y. & Hou, Z. F. Structural stabilities, electronic structures and lithium deintercalation in Li_xMSiO_4 (M=Mn, Fe, Co, Ni): A GGA and GGA+U study. *Computational Materials Science* **44**, 1243–1251 (2009).
 89. Kulik, H. J., Cococcioni, M., Scherlis, D. A. & Marzari, N. Density Functional Theory in Transition-Metal Chemistry: A Self-Consistent Hubbard U Approach. *Phys. Rev. Lett.* **97**, 103001 (2006).
 90. Chakraborty, A., Dixit, M., Aurbach, D. & Major, D. T. Predicting accurate cathode properties of layered oxide materials using the SCAN meta-GGA density functional. *npj Computational Materials* 46–49 (2018). doi:10.1038/s41524-018-0117-4
 91. Deák, P., Aradi, B., Frauenheim, T., Janzén, E. & Gali, A. Accurate defect levels obtained from the HSE06 range-separated hybrid functional. *Physical Review B - Condensed Matter and Materials Physics* **81**, 1–4 (2010).
 92. Ouyang, C. Y. *et al.* Ab initio molecular-dynamics studies on $\text{Li}_x\text{M}_2\text{O}_4$ as cathode material for lithium secondary batteries. *Europhysics Letters* **67**, 28–34 (2004).
 93. Lett, G. C. E. S., Ven, A. Van Der & Ceder, G. Lithium Diffusion in Layered Li_xCoO_2 Lithium Diffusion in

- Layered Li_xCoO_2 . 3–7 (2000).
94. Yang, Z. *et al.* Arrangement in $\text{La}_1/3\text{NbO}_3$ Obtained by First-Principles Density Functional Theory with Cluster Expansion and Monte Carlo Simulation. *J. Phys. Chem. C* **124**, 9746 (2020).
 95. Nakayama, M., Shirasawa, A. & Saito, T. Arrangement of La and vacancies in $\text{La}_2/3\text{TiO}_3$ predicted by first-principles density functional calculation with cluster expansion and Monte Carlo simulation. *Journal of the Ceramic Society of Japan* **117**, 911–916 (2009).
 96. Zheng, Y., Lu, L., Han, X., Li, J. & Ouyang, M. LiFePO_4 battery pack capacity estimation for electric vehicles based on charging cell voltage curve transformation. *Journal of Power Sources* **226**, 33–41 (2013).
 97. Haile, J. M., Johnston, I., Mallinckrodt, A. J. & McKay, S. Molecular Dynamics Simulation: Elementary Methods. *Computers in Physics* **7**, 625 (1993).
 98. Allen, M. P. & Tildesley, D. J. Computer Simulations of liquids, 1987. London, UK (1983).
 99. 2. Computer-Simulation Methods. **1990**, 8–9 (1990).
 100. Ciccotti, G. Molecular-dynamics simulation of statistical-mechanical systems: Varenna on Lake Como, Villa Monastero, 23 July–2 August 1985. (1986).
 101. Tateishi, K. & du BOULAY Pand Nobuo ISHIZAWA, D. Behavior of Li in LiMn_2O_4 Structure: Molecular Dynamics Study. *Journal of the Ceramic Society of Japan* **112**, 658–662 (2004).
 102. Amundsen, B., Rozière, J. & Islam, M. S. Atomistic simulation studies of lithium and proton insertion in spinel lithium manganates. *Journal of Physical Chemistry B* **101**, 8156–8163 (1997).
 103. Islam, M. S. *et al.* Atomic-Scale Investigation of Defects, Dopants, and Lithium Transport in the LiFePO_4 Olivine-Type Battery Material. 5085–5092 (2005).
 104. Whiteside, A., Fisher, C. A. J., Parker, S. C. & Saiful Islam, M. Particle shapes and surface structures of olivine NaFePO_4 in comparison to LiFePO_4 . *Physical Chemistry Chemical Physics* **16**, 21788–21794 (2014).
 105. Gardiner, G. R. & Islam, M. S. Anti-site defects and ion migration in the $\text{LiFe}_{0.5}\text{Mn}_{0.5}\text{PO}_4$ mixed-metal cathode material. *Chemistry of Materials* **22**, 1242–1248 (2010).
 106. Boulfelfel, S. E., Seifert, G. & Leoni, S. Atomistic investigation of Li^+ diffusion pathways in the olivine LiFePO_4 cathode material. *Journal of Materials Chemistry* **21**, 16365–16372 (2011).
 107. Tealdi, C., Spreafico, C. & Mustarelli, P. Lithium diffusion in $\text{Li}_{1-x}\text{FePO}_4$: The effect of cationic disorder. *Journal of Materials Chemistry* **22**, 24870–24876 (2012).
 108. Armstrong, A. R., Kuganathan, N., Islam, M. S. & Bruce, P. G. Structure and lithium transport pathways in $\text{Li}_2\text{FeSiO}_4$ cathodes for lithium batteries. *Journal of the American Chemical Society* **133**, 13031–13035 (2011).
 109. Kuganathan, N. & Islam, M. S. $\text{Li}_2\text{MnSiO}_4$ lithium battery material: Atomic-scale study of defects, lithium mobility, and trivalent dopants. *Chemistry of Materials* **21**, 5196–5202 (2009).
 110. Tripathi, R., Gardiner, G. R., Islam, M. S. & Nazar, L. F. (1) Tripathi, R.; Gardiner, G. R.; Islam, M. S.; Nazar, L. F. Alkali-ion Conduction Paths in LiFeSO_4F and NaFeSO_4F avorite-Type Cathode Materials. *Chem. Mater.* 2011, 23 (8), 2278–2284. Alkali-ion Conduction Paths in LiFeSO_4F and NaFeSO_4F avorite-. *Chemistry of Materials* **23**, 2278–2284 (2011).
 111. Leung, K. & Budzien, J. L. Ab initio molecular dynamics simulations of the initial stages of solid-electrolyte interphase formation on lithium ion battery graphitic anodes. *Physical Chemistry Chemical Physics* **12**, 6583–6586 (2010).
 112. Lee, S., Jung, S. C. & Han, Y.-K. First-principles molecular dynamics study on ultrafast potassium ion transport

- in silicon anode. *Journal of Power Sources* **415**, 119–125 (2019).
113. Zhao, X. *et al.* Computational screening and first-principles investigations of NASICON-type $\text{Li}_x\text{M}_2(\text{PO}_4)_3$ as solid electrolytes for Li batteries. *Journal of Materials Chemistry A* **6**, 2625–2631 (2018).
114. Zhang, Z. *et al.* Correlated Migration Invokes Higher Na^+ -Ion Conductivity in NaSICON-Type Solid Electrolytes. *Advanced Energy Materials* **9**, 1902373 (2019).
115. Noda, Y. *et al.* Research Update: Ca doping effect on the Li-ion conductivity in NASICON-type solid electrolyte $\text{LiZr}_2(\text{PO}_4)_3$: A first-principles molecular dynamics study. *APL Materials* **6**, (2018).
116. Jalem, R. *et al.* Concerted migration mechanism in the Li ion dynamics of garnet-type $\text{Li}_7\text{La}_3\text{Zr}_2\text{O}_{12}$. *Chemistry of Materials* **25**, 425–430 (2013).
117. Wang, Z. *et al.* Doping effects of metal cation on sulfide solid electrolyte/lithium metal interface. *Nano Energy* **84**, 105906 (2021).
118. Hakari, T. *et al.* Structural and Electronic-State Changes of a Sulfide Solid Electrolyte during the Li Deinsertion-Insertion Processes. *Chemistry of Materials* **29**, 4768–4774 (2017).
119. Park, C. *et al.* Molecular simulations of electrolyte structure and dynamics in lithium–sulfur battery solvents. *Journal of Power Sources* **373**, 70–78 (2018).
120. Wang, A., Kadam, S., Li, H., Shi, S. & Qi, Y. Review on modeling of the anode solid electrolyte interphase (SEI) for lithium-ion batteries. *npj Computational Materials* **4**, (2018).
121. Takenaka, N. & Nagaoka, M. Microscopic Elucidation of Solid-Electrolyte Interphase (SEI) Film Formation via Atomistic Reaction Simulations: Importance of Functional Groups of Electrolyte and Intact Additive Molecules. *The Chemical Record* **19**, 799–810 (2019).
122. Hautier, G. *et al.* Novel mixed polyanions lithium-ion battery cathode materials predicted by high-throughput ab initio computations. *Journal of Materials Chemistry* **21**, 17147–17153 (2011).
123. Frost, R. L., López, A., Scholz, R., Belotti, F. M. & Xi, Y. A vibrational spectroscopic study of the anhydrous phosphate mineral sidorenkite $\text{Na}_3\text{Mn}(\text{PO}_4)(\text{CO}_3)$. *Spectrochimica Acta Part A: Molecular and Biomolecular Spectroscopy* **137**, 930–934 (2015).
124. Chen, H. *et al.* Sidorenkite ($\text{Na}_3\text{MnPO}_4\text{CO}_3$): A New Intercalation Cathode Material for Na-Ion Batteries. *Chemistry of Materials* **25**, 2777–2786 (2013).
125. Xie, B. *et al.* Cathode properties of $\text{Na}_3\text{MPO}_4\text{CO}_3$ (M = Co/Ni) prepared by a hydrothermal method for Na-ion batteries. *Evergreen* **6**, 262–266 (2019).
126. Hautier, G. *et al.* Designing multielectron lithium-ion phosphate cathodes by mixing transition Metals. *Chemistry of Materials* **25**, 2064–2074 (2013).
127. Fujimura, K. *et al.* Accelerated Materials Design of Lithium Superionic Conductors Based on First-Principles Calculations and Machine Learning Algorithms. *Advanced Energy Materials* **3**, 980–985 (2013).
128. Fujimura, K. *et al.* Analysis of lithium-ion conduction in LISICON-based solid electrolytes by first-principles molecular dynamics simulation. in *ECS Meeting Abstracts* 1195 (IOP Publishing, 2012).

Chapter 2. Arrangement in $\text{La}_{1/3}\text{NbO}_3$ Obtained by First-Principles Density Functional Theory with Cluster Expansion and Monte Carlo Simulation

2.1 Introduction

As described in Chapter 1, conventional organic liquid electrolytes currently commonly used in lithium ion batteries have many fatal disadvantages. Therefore, in order to develop higher-performance batteries, solid electrolytes need to be used to replace traditional organic liquid electrolytes.^{1,2}

All solid-state lithium-ion batteries exhibit lower current and voltage densities than conventional lithium-ion batteries because the ionic conductivity of a solid electrolyte is low and the impedance at the solid–solid interfaces is high.^{3,4,5} Solving these problems is key to the commercialization of all solid-state batteries. Our research target material lanthanum lithium niobite, $\text{Li}_x\text{La}_{(1-x)/3}\text{NbO}_3$ (LLNO), is attractive A-site-deficient perovskite candidate for fast Li ion conduction owing to the higher concentration of vacancy sites and larger lattice than lanthanum lithium titanate LLTO.⁶

X-ray diffraction (XRD) and neutron diffraction (ND) structural characterization study results, revealed that the La atoms in this A-site deficient LLNO are arranged into alternately La rich layers (1/3 vacancies) and La poor layers (all vacancies). Across a series of compositions, Li free $\text{La}_{1/3}\text{NbO}_3$ has an orthorhombic unit cell and lattice parameter $a=3.91 \text{ \AA}$, $b=3.92 \text{ \AA}$, $c=7.91 \text{ \AA}$ (space group Cmmm) as shown in Figure.2.1⁷.

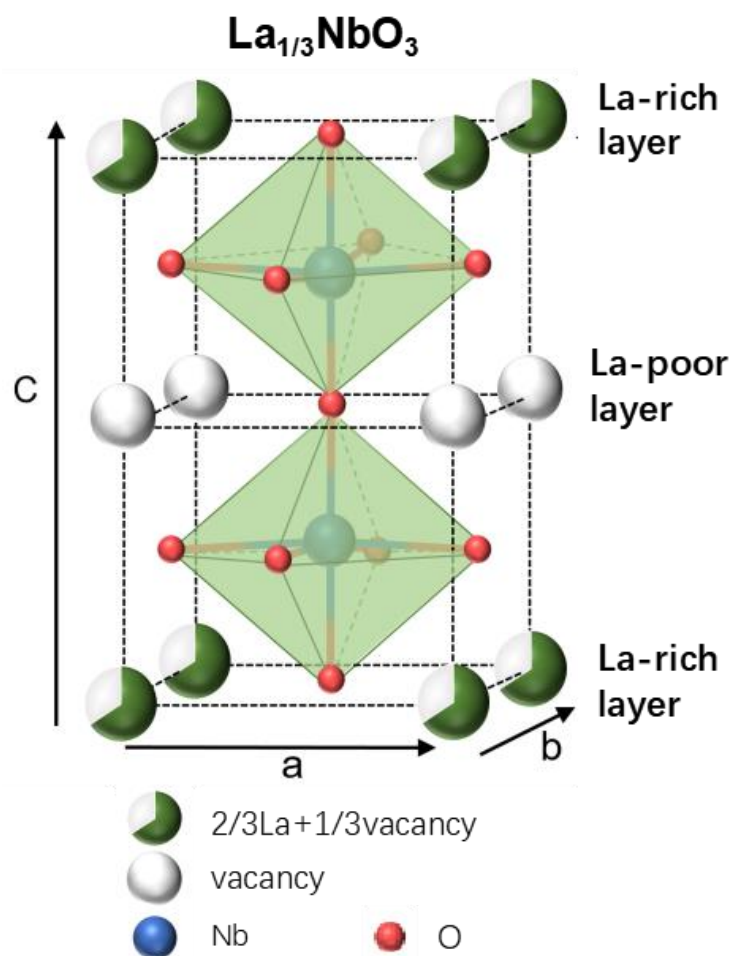


Fig 2.1 Crystal structure of La_{1/3}NbO₃ showing alternating La-rich layers (labeled A1, the ratio of La atoms and vacancies is two-thirds) and La-poor layers (labeled A2, the A-site cations are all vacancies) paralleled to (001)_p, where subscript p indicates the conventional cubic perovskite cell.

Additionally, the arrangement of La atoms in the La-rich layers is not random; a modulated structure has been reported.^{8,9} As shown in Figure 2.2, the spots $\{\omega\}$ appeared at $1/4 d^*(001)_p$ and $1/6.7 d^*(110)_p$, suggest the existence of a modulated arrangement of La/Vac along these directions. The satellite spots appeared as two sets, symmetry related by $\pi/2$ around $[001]_p$ in (b) also suggest that there is some modulate repeating units throughout these directions. Anyway, these are clearly visible evidence to prove that in the La-rich layer of LLNO, existing a quasi-periodic ordering structure.

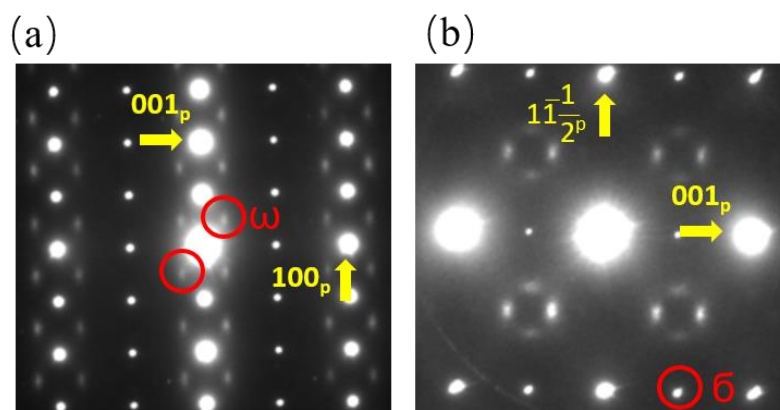


Fig 2.2 SAED patterns of $\text{La}_{1/3}\text{NbO}_3$, view direction of (a) along $[\bar{1} 1 0]_p$ and (b) is $[\bar{1} 1 4]_p$.

Based all the observations, Garcia-Martin supposed the reciprocal unit cell of LLNO in Figure 2.3.⁸ They deduced that the coherent length of the domain boundary periodicity is about 60 Å, so the shape of the microdomains is approximately square.

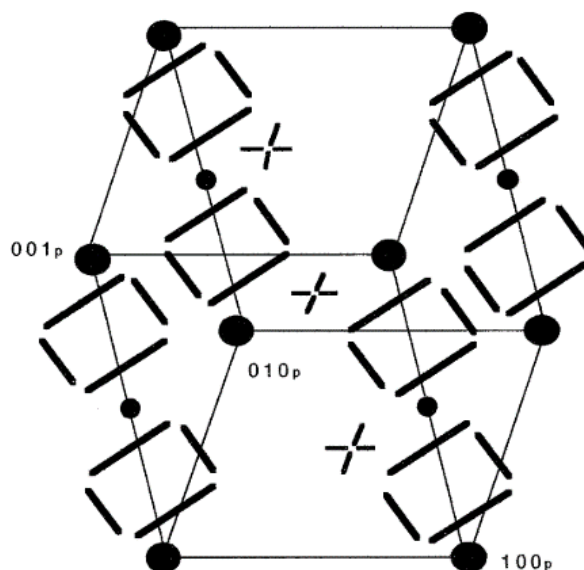


Fig 2.3 Imaginary reciprocal lattice of $\text{Li}_x\text{La}_{(1-x)/3}\text{NbO}_3$, $0 \leq x \leq 0.06$

Compared with LLTO, LLNO has more intrinsic vacancies and a larger unit cell volume, so it follows that it would have greater Li-ion conductivity. However, this assumption is inconsistent with the experimental observations, the highest observed bulk ionic conductivity of LLNO at room temperature is about $10^{-4} \text{ S cm}^{-1}$ which is smaller than that of LLTO, almost an order of magnitude difference. It is well known that the electrochemical properties of perovskite materials are strongly related to their crystal

structure and their ion arrangements^{10,11}. For example, doping a suitable proportion of alkaline earth materials in A-site can extend the lattice; decreasing the activation energy for Li ions hopping¹². Therefore, elucidating the undetermined modulated arrangement of Cations/Vacancies inside La-rich layers of LLNO may be the key to understanding the unexpectedly low conductivities observed.

Information about local atomic arrangements will facilitate analysis of the gap between theoretical and observed conductivities. It's possible to design LLNO materials with higher ionic conductivity using the description of detailed atomic arrangement obtained by computational simulation. Ab initio density functional theory (DFT) calculations are a reliable tool for calculating local atomic arrangements and energies. Some DFT computational studies successfully simulated the alternating La-rich and La-poor layers along c-axis and the resultant BO₆ octahedral tilt in LLNO, LLTO.^{13,14} However cell size limitations of DFT computations and the combinatorial expense of possible arrangements of La/Li/vacancy prevent the direct determination of long range ordering in modulated arrangements. In order to overcome these limitations, cluster expansion (CE) and Monte Carlo(MC) simulations were utilized to investigate this topic to endure these limitations^{15,16}.

In this chapter, Li-free La_{1/3}NbO₃ was used as a framework for LLNO to simulate the Cation/Vacancy modulated arrangement, a hybrid method that combined DFT cluster expansion with MC simulation was performed. Since La atoms effectively stays still during the simulation, this A-site arrangement determines the available way for Li-ion to diffuse along the vacancies in the material. The calculated arrangements are verified by comparing them (simulated electron diffraction patterns) with experimental electron diffraction (ED) data. The reporting content is basically based on the following aspects:

1. Verify the accuracy of the fitting results obtained by Cluster expansion
2. The process of using Monte Carlo approach to explore the potential modulated arrangement of La/Vac in LNO.
3. Analyze the reasons for the formation of different modulated structures and their influence on the diffusion of Li ions in LNO.
4. Verify the accuracy of our simulation result by comparing with the experimental data.

2.2 Research methods

To obtain the long-range atomic structure of La/vacancy in $\text{La}_{1/3}\text{NbO}_3$, the calculation process is divided into three parts. After that we used solid-state reaction method to prepare the $\text{La}_{1/3}\text{NbO}_3$ crystal, and crystalline phase identification was measured by XRD and TEM.

2.2.1 DFT calculation process and calculation settings

Firstly, the total energy of different A-site configurations of $\text{La}_{1/3}\text{NbO}_3$ was calculated using ab initio DFT. The Vienna ab initio simulation package (VASP) utilizing the generalized gradient approximation (GGA)¹⁷ and projector-augmented wave (PAW)¹⁸ was used. After the relaxation of the structure is completed, the energy of the optimized structures is recalculated to correct the variation of the plane wave base during the relaxation process. More explanation is available in previous research results²⁰. The computationally optimized structures reproduce the experimental results well, such as the extended X-ray absorption fine structure (EXAFS) technique. The details of computational conditions are follows,

- ✓ Cutoff energy for the plane-wave basis: 500 eV
- ✓ K-point: 1000 (i.e., N_x , N_y , and N_z , which are the number of grids in the k_x -, k_y -, and k_z -directions of the reciprocal space, were set to satisfy $N_x \times N_y \times N_z \times N_{\text{atom}} \sim 1000$, where N_{atom} is the number of atoms in each unit cell)
- ✓ Convergence test: energy difference < 3 meV/atom
- ✓ Stopping criterion: ionic relaxation energy difference < 0.1 meV

2.2.2 Cluster Expansion (CE)

Secondly, the total energy of various La/Vacancy arrangements within the NbO_3 octahedron sub lattice obtained from the DFT calculations were fitted to effective cluster interactions (ECI)¹⁹, such that the total energy of each unique $\text{La}_{1/3}\text{NbO}_3$ cell is equal to the sum of the clusters it contains. The cluster expansion formalism¹⁵ is used to fit the cluster interaction energies. According to the Eq (2-1), the total energy of $\text{La}_{1/3}\text{NbO}_3$ with arbitrary La and vacancies arrangements can be calculated by this summation of polynomials, ϕ_α is related to occupation variables σ_i which decided by La sites among cluster α , defined by Eq (2-2). For the whole A-sites in the structure, σ_i has different

values according to the occupation situation, if the site i is occupied by La ion σ_i is +1, otherwise it equal -1. In this study cluster α includes pair clusters and triplet clusters, all come from nearest neighbor then second nearest neighbor and so on. The constants J_α are the ECI obtained by the fitting results of DFT calculation. This makes it possible to calculate the total energy of large cells with complicated arrangements quickly, as a sum of the cluster energies containe.

$$E = \sum_{\alpha} J_{\alpha} \cdot \phi_{\alpha} \quad (2-1)$$

$$\phi_{\alpha} = \prod_{i \in \alpha} \sigma_i \quad (2-2)$$

2.2.3 Monte Carlo simulation (MC)

Metropolis MC calculations were performed using the well-fitted ECI results. Metropolis MC is a standard simulation technique that uses random sampling to evolve a system under canonical ensemble to find the lowest energy structure. Cells much larger than those possible in DFT can be rapidly assessed using the ECI cluster values to calculate the total energy during the MC runs. To investigate long-range ordering and minimize the specific box size effects, La/vacancy only supercells ranging from $8 \times 8 \times 8$ (171 atoms) to $15 \times 15 \times 15$ (1126 atoms) were simulated. This was done to allow the maximum possible differently ordered patterns to emerge, as the supercell dimensions dictate the form of the possible repeating La/vacancy arrangements. Each supercell was cycled through five temperature cycles (from 10000 K to 300 K, 300 K to 3000 K, 3000 K to 300 K, 300 K to 1500 K, and 1500 K to 300 K) sequentially during the MC run to obtain the most stable structure. The MC passes for equilibration and averaging time were set as 10000 each, where an MC pass corresponds to the number of attempted flips equal to the number of lattice sites in the simulation cell. Convergence was considered to be attained when the minimum energy reached at 300 K in each cycle converged. The temperature cycling process was started at a very high temperature to ensure that energy barriers due to unfavorable moves were overcome.²⁴ Because of the limitation of the MC calculation, the temperatures at which the structural transformation takes place may be higher than the actual experimental temperatures. Setting a higher simulation temperature can provides enough energy for the system to ensure that the arrangement with the lowest energy structure can be obtained. The $12 \times 12 \times 12$ supercell was found to exhibit a structure with the minimum energy per formula unit. To investigate the long range of the

modulated arrangement of the La-rich layer, the $12 \times 12 \times 12$ supercell was selected as the basic unit of the long-range order; scaled up supercells $24 \times 24 \times 24$ and $36 \times 36 \times 36$ were studied. This was to ensure coherence with the obtained low energy pattern. In this study, the EC and MC simulations were both performed using the ATAT program package.^{20,21} The selected area electron diffraction (SAED) simulation was performed using SingleCrystal 3.1 (CrystalMaker Software Ltd.)²² The crystal structure images were drawn using VESTA.²³

2.2.4 Other involved software

The selected area electron diffraction (SAED) simulation was performed using SingleCrystal 3.1 (CrystalMaker Software Ltd.)²² The crystal structure images were drawn using VESTA.²³

2.2.5 Experiment

In this chapter, to compare the simulated SAED patterns with the experimental values, $\text{La}_{1/3}\text{NbO}_3$ were synthesized by conventional solid-state method.¹³ Reaction materials La_2O_3 (99.9%) and Nb_2O_5 (99.9%) were mixed by the stoichiometric amounts. La_2O_3 powders were preheated at 1000 °C for 12 h for decarboxylation. The mixture of reagents was heated at 800 °C for 2 h and then at 1300 °C for 48 h in air with several intermittent grindings. Crystalline phase identification and lattice parameter evaluation were carried out by powder X-ray diffraction using a Rigaku Mini Flex600 diffractometer with Cu $K\alpha$ radiation. A single-phase formation was confirmed (as seen in Figure 2.4) unlike in previous studies.^{24,25} The SAED patterns of the $\text{La}_{1/3}\text{NbO}_3$ powder were obtained using transmission electron microscopy (TEM) JEOL JEM-ARM 200F.

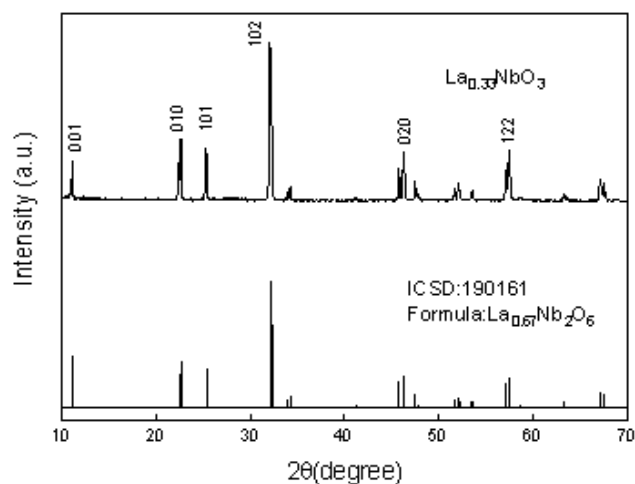


Fig 2.4 Comparison of the XRD patterns between simulated and experimentally obtained $\text{La}_{1/3}\text{NbO}_3$ perovskites. The simulation patterns are derived from the reported structure (ICSD #190161) belonging to an orthorhombic system.²⁶

2.3 Results and Discussion

2.3.1 Verify the accuracy of the fitting results obtained by Cluster expansion

2.3.1.1 Linear fit result of E_{ECI} using CE formalism compared with E_{DFT}

After finished the cluster expansion, we compared the total energy calculated using DFT(E_{DFT}) with the fitted energy (E_{ECI}) obtained using the cluster expansion formalism (see Eqs. 2-1 and 2-2) for the total 100 different La/Vacancies configurations, as shown in Figure 2.5. In this chapter, since only $\text{La}_{1/3}\text{NbO}_3$ forms the perovskite structure observed in LLNO, only one component of LNO is cluster-fitted in the process of cluster expansion. In order to facilitate the comparison of the two sets of values, the lowest energy obtained by the DFT calculation is set to zero. The ground states were correctly reproduced and predicted, as shown in Figure 2.5(b). Based on the linear fit result and the root mean square error calculated for the two sets of values (RMSE = 0.018 eV per $\text{La}_{1/3}\text{NbO}_3$) and leave-one-out cross-validation score (0.027 eV per $\text{La}_{1/3}\text{NbO}_3$), E_{ECI} obtained using the cluster expansion formalism shows a reasonable goodness of fit with E_{DFT} .

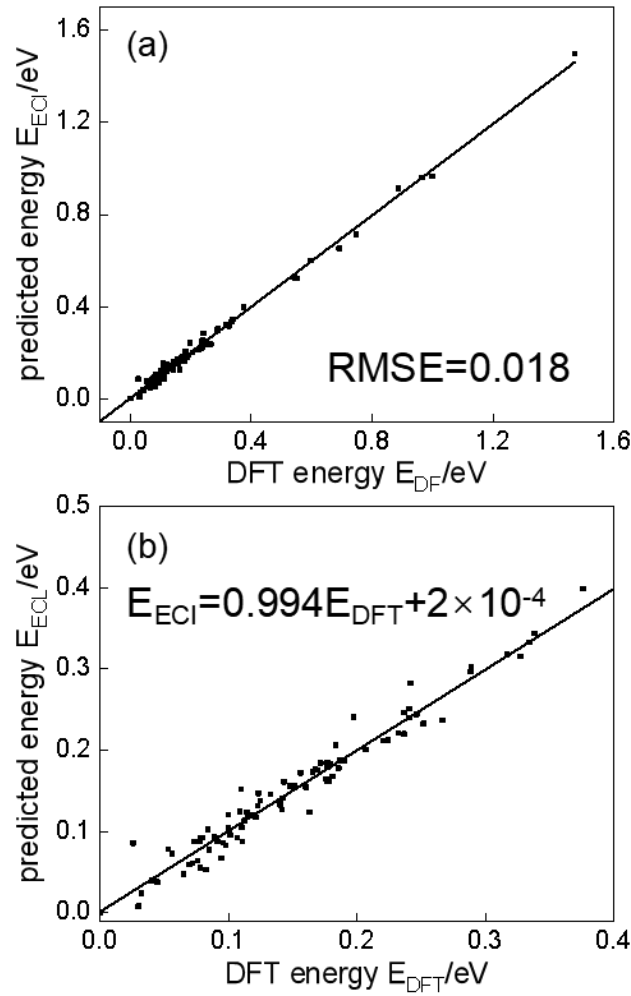


Fig. 2.5 (a) Total energy obtained by DFT calculation (E_{DFT}) versus fitting energy obtained by cluster expansion (E_{ECI}). (b) Enlarged plot around 0 eV. The solid line indicates the linear fit result obtained using the least-squares linear fit function.

2.3.1.2 The effective of clusters interaction judged by the normalized interaction distance

The ECI J_{α} of the two types of clusters is plotted as the function of the interaction distance normalized to the conventional cubic perovskite lattice parameter a_p , as shown in Figure 3. The pair and triplet clusters were indicated by the circle and cross marks, respectively. To predict the energy by converting E_{DFT} from the 100 different La/vacancy configurations, 16 pair clusters and 12 triplet clusters are used. The value of the pair clusters is positive, indicating that all two-body interactions between different species (La–vacancy) are negative and attractive, at same time, the same species (La–La or

vacancy–vacancy) are positive and repulsive. The overall trend of the pair clusters shows that the cluster energy decreases with increasing interaction distance. The cluster energy approaches zero when the interaction distance is over $3.5 a_p$ (Figure 2.6(a)). However, with the interaction distance increases, the number of clusters will also increase cubically with the increasing simulation distance. This means that although the energy of a single cluster is low, the total cluster energy may play an important role in the total energy. The normalized interaction distance plot (Figure 2.6(b)) shows that the influence of the low-value long-distance clusters can almost be ignored when the cut-off distance is greater than $4 a_p$.

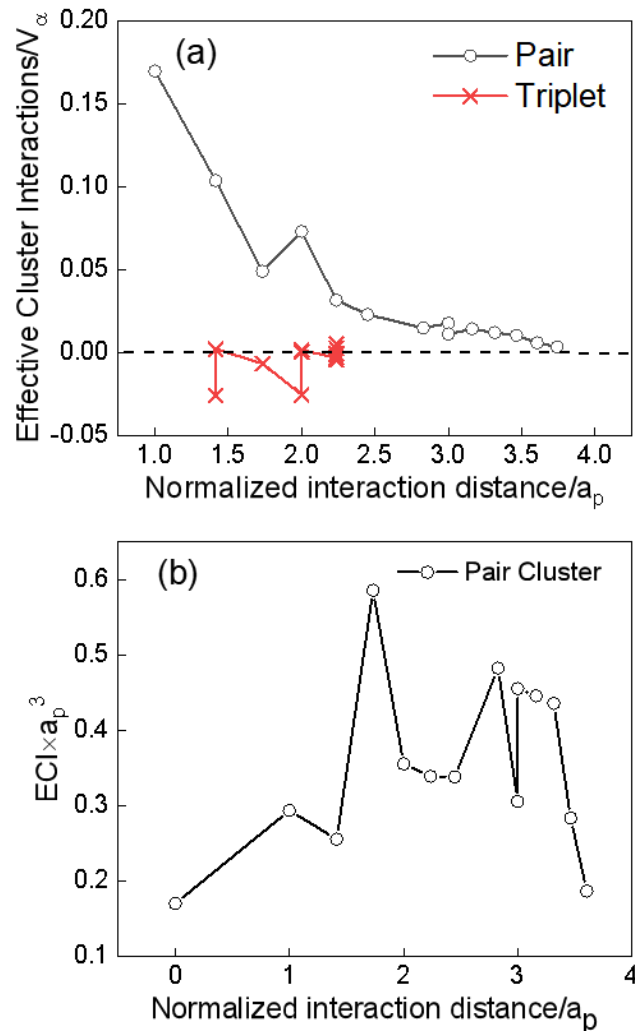


Fig. 2.6 (a) Effective cluster interaction (ECI) of two different types of clusters (circle and cross symbols represent pair and triplet clusters, respectively) versus

interaction distance (the distance is normalized with the average LLNO lattice parameter a_p). (b) Product of pair cluster ECI and cube of a_p versus normalized interaction distance.

2.3.1.3 The correlation between the energy of configuration of $\text{La}_{1/3}\text{NbO}_3$ and cell volume

Compared the cell volume and the total energy for all the different configurations of $\text{La}_{1/3}\text{NbO}_3$ involved in cluster expansion approach which calculated by DFT calculations. It has some positive correlation for all the datasets as shown in Figure 2.7(a), but magnified plot (Figure 2.7(b)) around low energy region (< 0.4 eV) is more important for MC calculations, it shows no obvious correlation between the energy and cell volume. This indicates that the total energy of $\text{La}_{1/3}\text{NbO}_3$ is more related to its atomic arrangement instead of the cell volume.

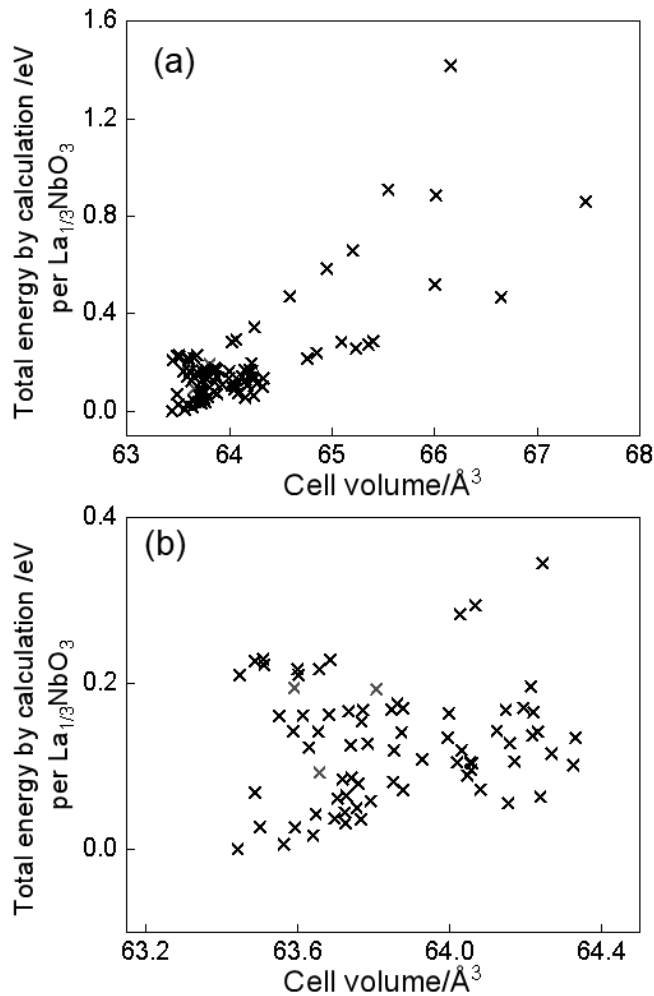


Fig. 2.7 (a) Total energy calculated by DFT calculation versus cell volumes for all the configurations obtained using the cluster expansion approach. (b) Enlarged plot of lower energy area (< 0.4 eV per $\text{La}_{1/3}\text{NbO}_3$).

2.3.2 The process of using Monte Carlo approach to explore the potential modulated arrangement of La/Vac in LNO.

2.3.2.1 Conducted MC run on various supercell sizes of LNO

The snapshots of MC derived La/vacancy arrangement in $\text{La}_{1/3}\text{NbO}_3$ with various supercell sizes after annealing from 2000K to 300 K are exhibited in Figure 2.8(a). The energy of the MC-derived odd-multiple supercells is greater than those of the even-multiple supercells. All the even-multiple supercells reproduced the alternate La-rich and La-poor layers along the c-axis, consistent with experimental results.^{7,8,9} The odd-multiple supercells cannot completely form the alternating La-rich, La-poor layers owing to the periodic boundary conditions used in the calculation. This result implies that the alternate La-rich and La-poor stacking structure significantly reduces the total energy (Figure 2.8(b)), consistent with the reported structure (Figure 2.1). If the obtained structure has alternating La-poor and La-rich layer structure, as well as there is a high ordered arrangement of La/Vacancy inside rich layer, the total energy will be reduced. The $12 \times 12 \times 12$ supercells obtained by using the MC simulation are the most stable structure, because its overall energy is the lowest. In this structure, the La-poor layer is completely empty, with the La ions occupying two-thirds of the total A sites in the La-rich layer. The La-rich layer exhibits a very highly ordered arrangement of closed squares of La surrounding the vacant sites (Figure 2.8(c)). It can be observed in the La-rich layer that the intra-layer arrangement is composed of several $4a_p \times 6a_p$ periodic small units, each of which includes 16 La ions and 8 vacancies. The site occupancy of the La ions in the small unit is the same as that in the La-rich layer, so that the entire layer can be subdivided by this small unit cell. Since in each small cell, La ions are arranged around the central vacancy, this modulated arrangement of La/Vacancy is simply called "closed arrangement" for identification.

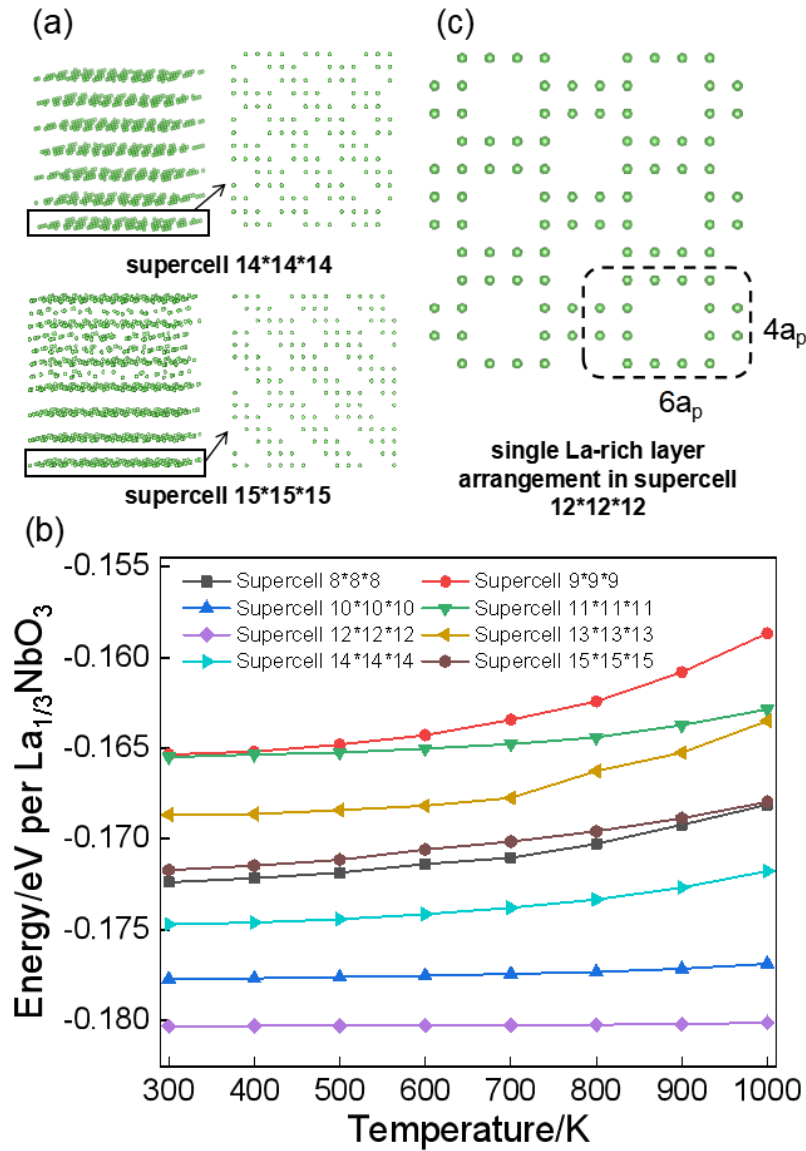


Fig. 2.8 (a) Snapshots of La/vacancy arrangements in different supercell structures of $\text{La}_{1/3}\text{NbO}_3$ in three dimensions and La-rich layer in two dimensions. (b) Variation in energy as a function of the temperature in different supercells of $\text{La}_{1/3}\text{NbO}_3$ in the low-temperature region (300–1000 K). (c) Enlarged plot of La/vacancy arrangement of the $12 \times 12 \times 12$ supercell in one of the ab planes.

2.3.2.2 Order/disorder phase transitions

The energy variation versus temperature of the system with the supercell $12 \times 12 \times 12$ is shown by the curve in Figure 2.10(a). The inset is enlarged plot of the original figure between 800 K and 300 K to show a rapid decreasing of energy in this zone.

It is obvious that the phase transition occurred induced by ordering/disordering of

La/vacancy arrangement for cooling/heating process at the temperature ranging from 1500 to 2000 K. As the overall crystal structure of the material does not change during the calculation, this order/disorder phase transition must be induced by the transition of the La/vacancy arrangement within the lattice. Figure 2.10(b) is the derivative of energy against temperature which correspond to the heat capacity at constant volume of the system, at least two phase transitions happened according to this figure, an obvious transition at around 2000K and a possible one at around 1500K (as arrows pointed in the figure). Note that the heat capacity derived from variance analysis agrees with that from the derivative of energy with respect to temperature, as shown in Figure 2.9, indicating good convergence of the present MC simulation.

The cause of occurrence of this second phase transitions can be due to the ordering/disordering arrangement variation of the La/vacancy during the MC simulation. The fact that $\text{La}_{1/3}\text{NbO}_3$ maintains the perovskite crystal structure, and the La/vacancy arrangement gradually becomes more orderly verified this phenomenon. (Figures 2.11 and 2.12).^{31,13,14}

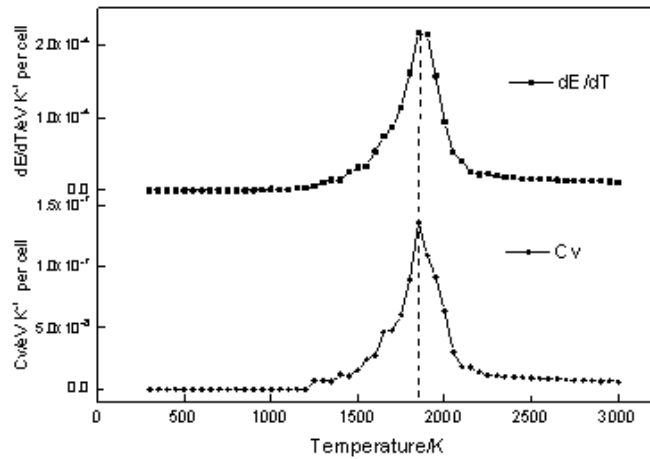


Fig. 2.9 Comparison of heat capacities derived from the variance in energy and from the derivative of energy with respect to temperature.^{28,29}

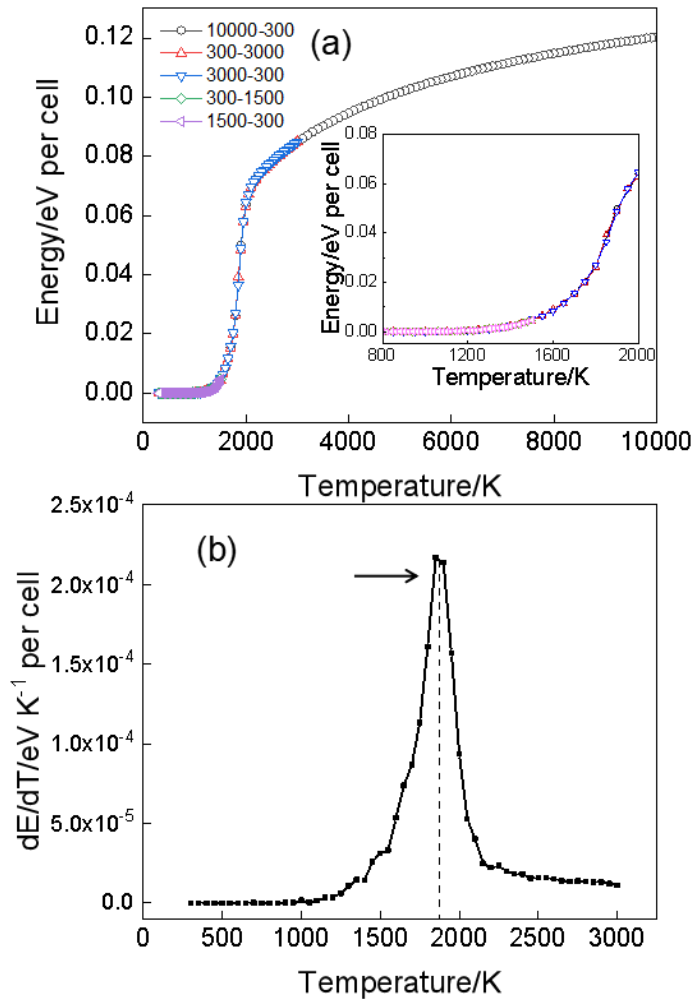


Fig. 2.10 (a) Variation in the energy as a function of the temperature in $\text{La}_{1/3}\text{NbO}_3$ (supercell $12 \times 12 \times 12$) calculated using the MC method. Different symbols in the figure indicate the different heating and cooling cycles. The inset is an enlarged plot of the original figure in the temperature range of 800–3000 K. The lowest energy of 0 eV is set as the baseline. (b) Derivative of energy with respect to temperature; the arrow in the plot indicates the second-order phase transition point.

The variation of the site occupancy of La ions in different ab planes (La-rich and La-poor) as a function of temperature as shown in (Figure 2.11). It is clear to see that the site occupancy of La ions in La-rich layer and La-poor layer remains two-thirds and zero respectively at low temperature (below 1000K). when the temperature above 1800 K, the site occupancy of La ions in La-rich layer decreases rapidly, and it accompanied with the number of La ions in La-poor layer sharply increases. This phenomenon indicates that La

ions, which were originally in a disordered state at high temperatures, undergo some sort of inter-layer transformation as the temperature of the system decreased. Combined with Figure 2.12, it indicates that this inter-layer transformation related to the alternate La-rich and La-poor layers stacking along C axis. This long-range ordering transformation can quickly reduce the energy of the system and make the system more stable. This phenomenon corresponds to the peak of the heat capacity curve in Figure 2.10(b) at about 2000K. The site occupancy of La ions shows a continuous change until about 1400K, but there is a clear slope change of the curve at around 1800K, as it was indicated in Figure 7. The difference between La-rich and La-poor layers is obvious at 1800K, although the process of structural modulation of La-rich layer shows the clear pattern at 1600K. The structural modulation of La-rich layers finishes later than the separation of La-rich and La-poor layers corresponding to the hump of the heat capacity in Figure 2.10(b) around 1500K.

To sum up, two types of order/disorder derived phase transition are observed from Figure 2.11 and 2.12. One is the disordering of the alternate La-rich and La-poor layers stacking along *c* axis which occur above 1800 K. The other phase transition occurs around 1500 K, which relates to disordering closed arrangement within *ab* plane as presented in Figure 2.9 (c)

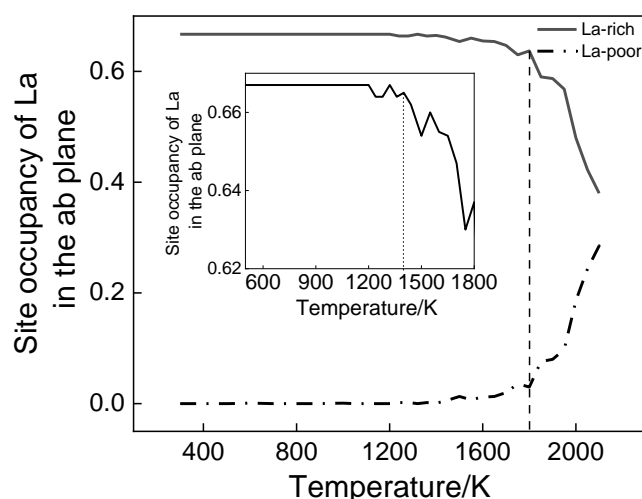


Fig. 2.11 Comparison of the variation in site occupancy of La ions in different *ab* planes as a function of temperature. The illustration is an enlarged plot.

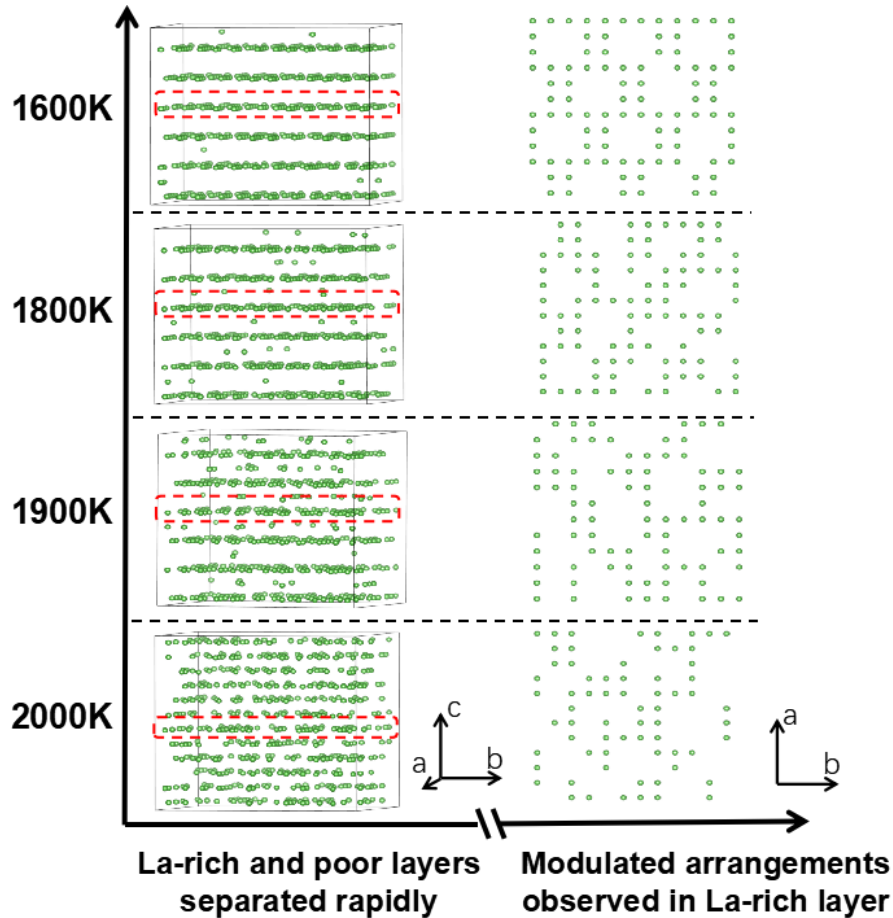


Fig. 2.12 Snapshots of different temperature structures (3D) corresponding to the rapid variation in energy shown in Figure 2.10, and the variation in La/vacancy arrangement in the La-rich layer, as marked (2D) for each temperature.

2.3.3 Analyze the reasons for the formation of different modulated structures and their influence on the diffusion of Li ions in LNO.

To investigate the other possible long-range modulated arrangement, the supercell $12 \times 12 \times 12$ which observed the closed arrangement was selected as a basic object, enlarge the 3D coordinates in equal proportions. The variation in the energy as a function of the temperature in per $\text{La}_{1/3}\text{NbO}_3$ supercell $36 \times 36 \times 36$ was shown in Figure 2.13(a). The energy shows a rapid decreasing at around 2000 K with the same feature of Figure 2.10, since the alternate layers stacking along C axis ($> \sim 1800$ K) during cooling/heating. However, at low temperature region, ~ 800 K, the curve displays differences from Figure 2.10(a) as shown in the inset in Figure 2.13(a). The energy at 300 K (~ 16 meV/ $\text{La}_{1/3}\text{NbO}_3$)

is slightly higher than the corresponding energy in the smaller $12 \times 12 \times 12$ supercell after the same cooling process (Figure 2.10). The energy drop observed at around 800 K in the subsequent heating/cooling cycle indicates energy hysteresis. Figure 2.13(b) displays the snapshots of the structure corresponding to the different energy convergence points. (The energy was indicated by the label (4) is the same as the lowest energy), two structures labeled as (1) and (4) all have the clear inter-layer arrangement but different La/Vacancy arrangement in La-rich layer. We confirmed the La/vacancy arrangement shown in Figure 2.14(b), which is the lowest energy labeled as indicated in Figure 2.13(b)(4), is the closed arrangement as presented in Figure 2.8(c). On the other hand, the atomic arrangement displayed by Figure 2.13(b)(1), showing slightly higher energy level than the closed arrangement, is more like a long-range ordered arrangement forming a striped pattern along diagonal direction (for convenience, this arrangement is called “stripe arrangement” in later). The transform process starts from the dislocation of the La ions outside the diagonal columns, as the degree of dislocation deepens, the columns is broken and the whole arrangement is changed from the diagonal to the closed one.

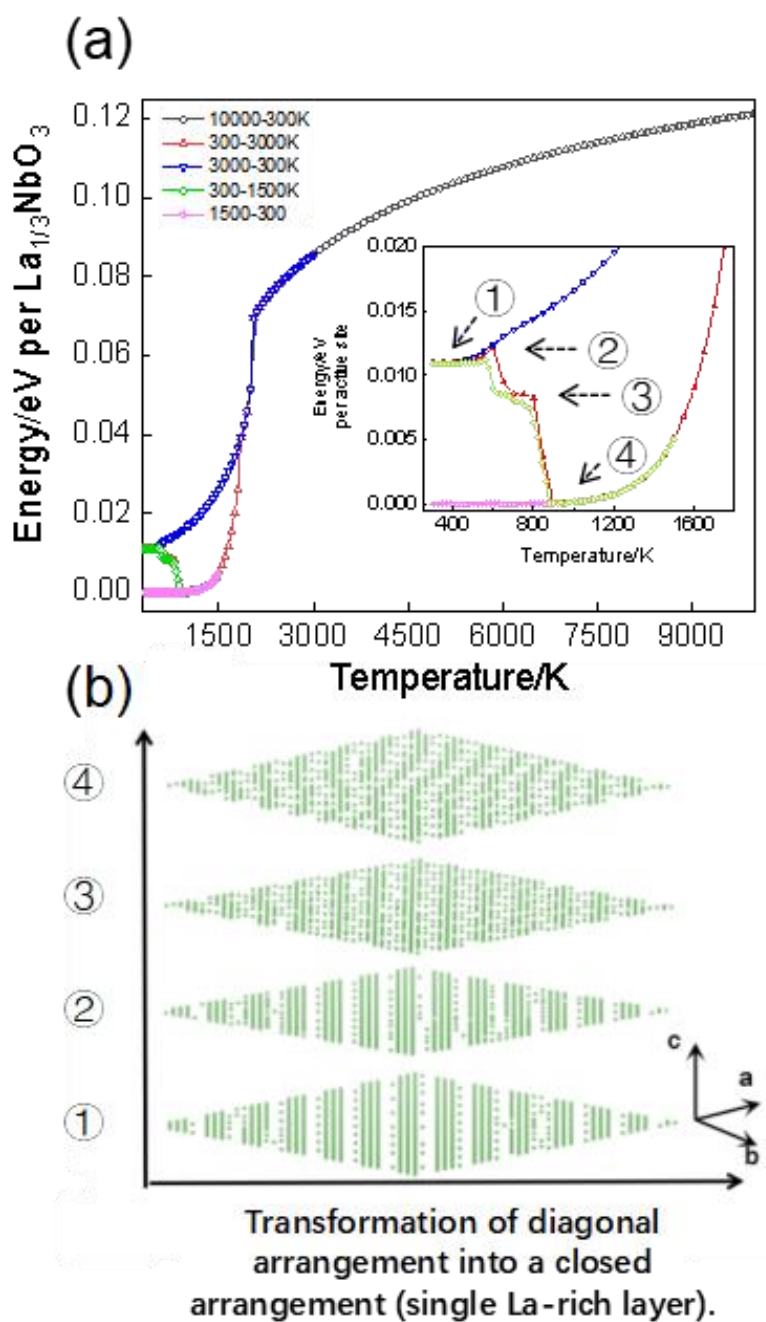


Fig. 2.13 (a) Variation in the energy as a function of the temperature in $\text{La}_{1/3}\text{NbO}_3$ (supercell $36 \times 36 \times 36$) calculated using the Monte Carlo method. The enlarged plot shows the area of interest. (b) Transformation of La-rich layer from striped arrangement to closed arrangement; each layer corresponds to the labels in (a).

From the above MC simulation results, we speculate that two low-energy stable structure arrangements: closed one and striped one, may exist in the real LNO system at the same time. So, the modulation structure of La-rich layer mentioned by experimental

studies^{8,9} should be the numberless nanodomains composed by these two arrangements. Since at diluted Li concentration regime in $\text{La}_{(1-x)/3}\text{Li}_x\text{NbO}_3$ that Li ions preferred to locate in A-site vacancies in La-rich layers¹⁶, the closed arrangement is the majority of the entire structure at room temperature and most Li ions are trapped in the center of the $4a_p \times 6a_p$ periodic units in the closed arrangement may be the reason that the Li ions conductivity in LLNO is lower than expectation as mentioned in introduction section.

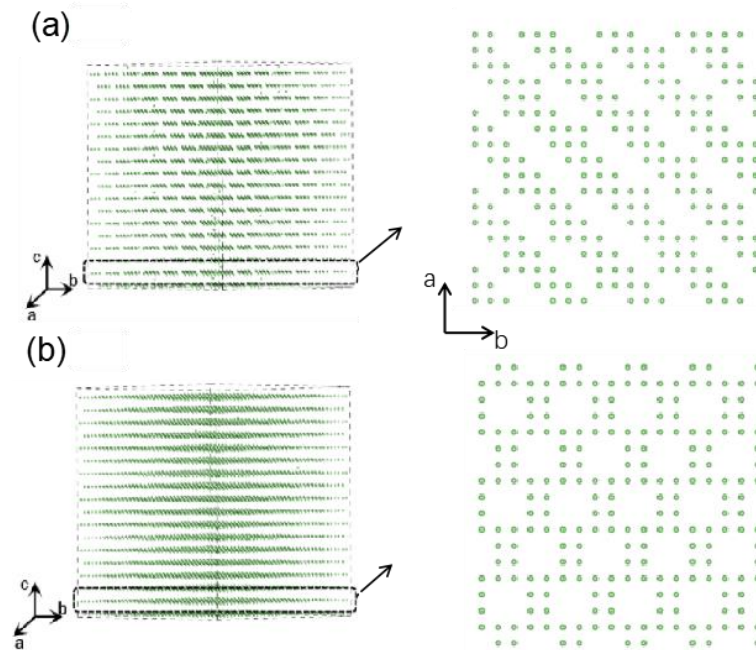


Fig. 2.14 (a) Snapshot of $\text{La}_{1/3}\text{NbO}_3$ structure corresponding to Figure 13(b1) and one-quarter original size of single La-rich layer. (b) Snapshot of $\text{La}_{1/3}\text{NbO}_3$ structure corresponding to Figure 13(b4) and one-quarter original size of single La-rich layer.

2.3.4 Verify the accuracy of our simulation result by comparing with the experimental data.

To further confirm that modulation structure of La/Vacancy arrangement revealed by this study corresponds to the real material, the experimental and the simulated SAED patterns are investigated and as shown in Figure 2.15 and Figure 2.16. Noted that the two types of SAED simulation patterns are presented derived from i) closed and ii) stripe La/vacancy arrangement, as shown in Figure 2.14(a) and (b), respectively. This simulated SAED patterns come from the La/vacancy structures derived solely, so there is no contribution of Nb and O ions. The experimental SAED patterns accord well with the previous study except for the extra spots $\{\frac{1}{2} k 0\}$ appeared at $(h/2 k/2 0)$ along $[001]_p$ zone

axis (h and k are odd) are rather faint in this study in comparison with the one in the reference^{8,9,30}. The previous paper suggested that the spots $\{\xi\}$ of $(h/2 \ k/2 \ 0)_p$ were ascribed to the NbO_6 octahedra tilted to La-poor layers. Therefore, the absence of the spots in simulated SAED patterns support the tilting of NbO_6 octahedra, since the present simulation study do not contain NbO_6 contribution.

In the both simulated SAED patterns derived from the closed and stripe arrangement structure, there are sharp reflections $\{\xi\}$ at $(0 \ 0 \ l/2)_p$ where l is odd, along observation direction $[010]_p$, these sharp reflections $\{\xi\}$ come from the alternating layers arrangement along c axis. In the patterns along the $[\bar{1}10]_p$ and $[114]_p$ directions, the spots $\{\xi\}$ indexed as $(h/2 \ k/2 \ 0)_p$ and spots $\{\zeta\}$ indexed as $((h/2 \ k/2 \ l/2)_p)$, respectively, are clearly visible in the experimental pattern (Figure 2.16). Unlike the spots $\{\xi\}$, which correspond to the in-phase octahedral tilting, the spots $\{\zeta\}$ are ascribed to antiphase octahedral tilting.^{8,31} However, neither of these two diffraction spots have been observed from my simulation results, which just shows that the sources of both are derived from the tilt of the NbO_6 octahedron, because the contribution of NbO_6 is not included in this study. According to the previous report, these diffuse spots $\{\omega\}$ are appeared around odd multiples of $(001/4)_p$ owing to some modulated structure.¹⁵ In our simulated patterns, the corresponding spots $\{\omega\}$ were also observed in the both closed and striped arrangements systems. As mentioned, present simulation only considers La/vacancy arrangements, so that the satellite spots are originated by superstructure formation, such as $4a_p \times 6a_p$ periodic units appeared in closed arrangement (Figure 2.8 (c)). Because the size of the simulation unit is very limited compared with the experimentally characterized bulk system, and it is difficult to simulate the effect of double diffraction, the streaked patterns of the diffuse spots were not reproduced in this work. What is interesting is that from our results, the position of the satellite point $\{\Phi\}$ are slightly shifted between the closed and the stripe arrangement, which indicates that the streaked pattern may be formed by the superimposition of the two arrangements. Hence, we infer that the $\text{La}_{1/3}\text{NbO}_3$ crystal is likely to consist of microdomains of closed and/or striped La/vacancy arrangements. In addition, two of the four satellite spots in the experimental SAED are reproduced in the present simulation. This can be ascribed to the formation of microdomain boundaries parallel to $(1 \ 0 \ 0)_p$ and $(0 \ 1 \ 0)_p$, as indicated in literature.³⁰

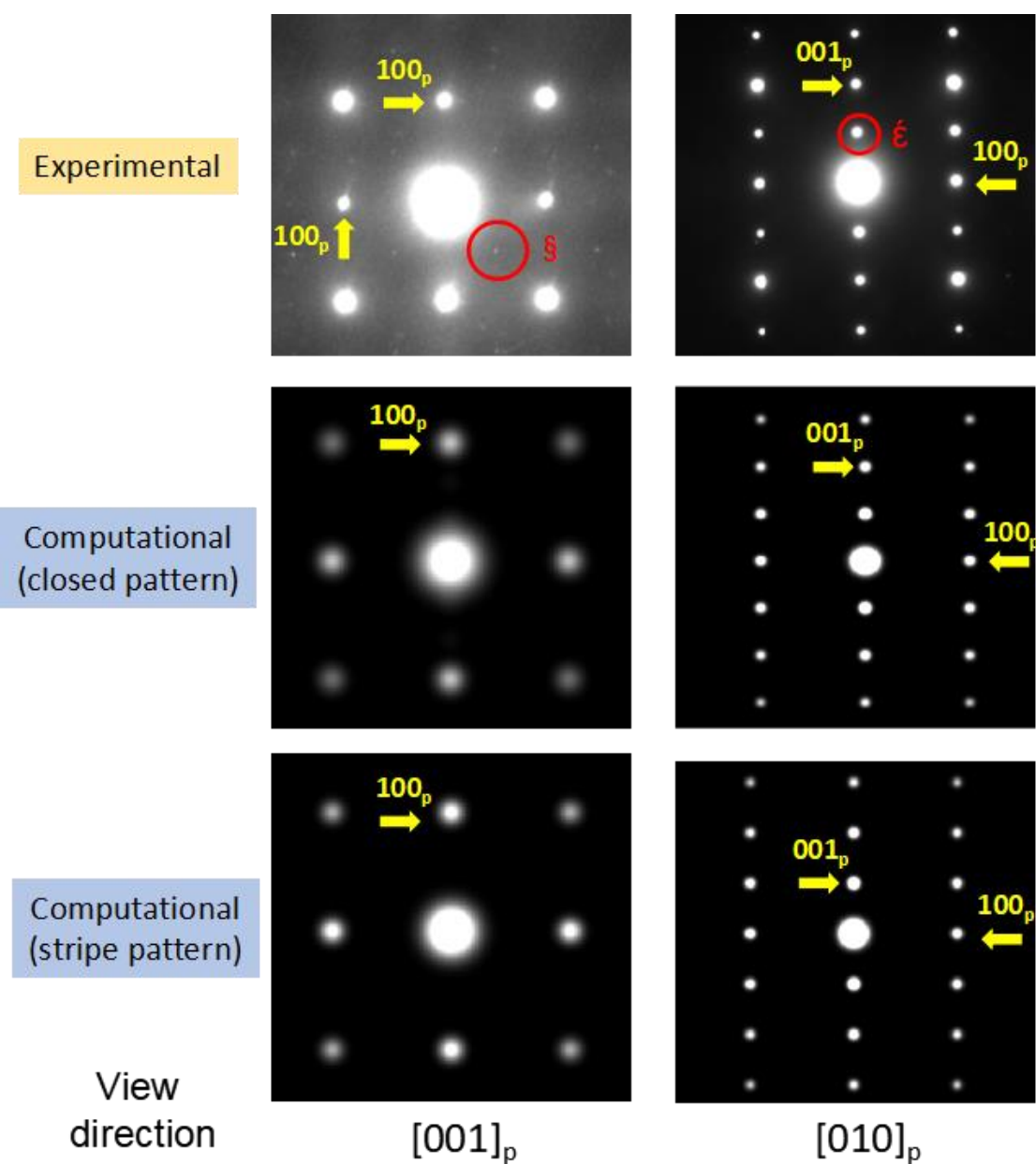


Fig. 2.15 Experimental and simulated selected area electron diffraction (SAED) patterns for $\text{La}_{1/3}\text{NbO}_3$. In the simulation, two types of La/vacancy arrangements are derived from the Monte Carlo simulations results, as shown in Figure 2.14(a) and 2.14(b), without NbO_6 contribution. Extra spots are present at $(h/2 \ k/2 \ 0)_p$ and $(0 \ 0 \ 1/2)_p$, which are labeled as $\{\S\}$ and $\{\epsilon\}$, respectively.

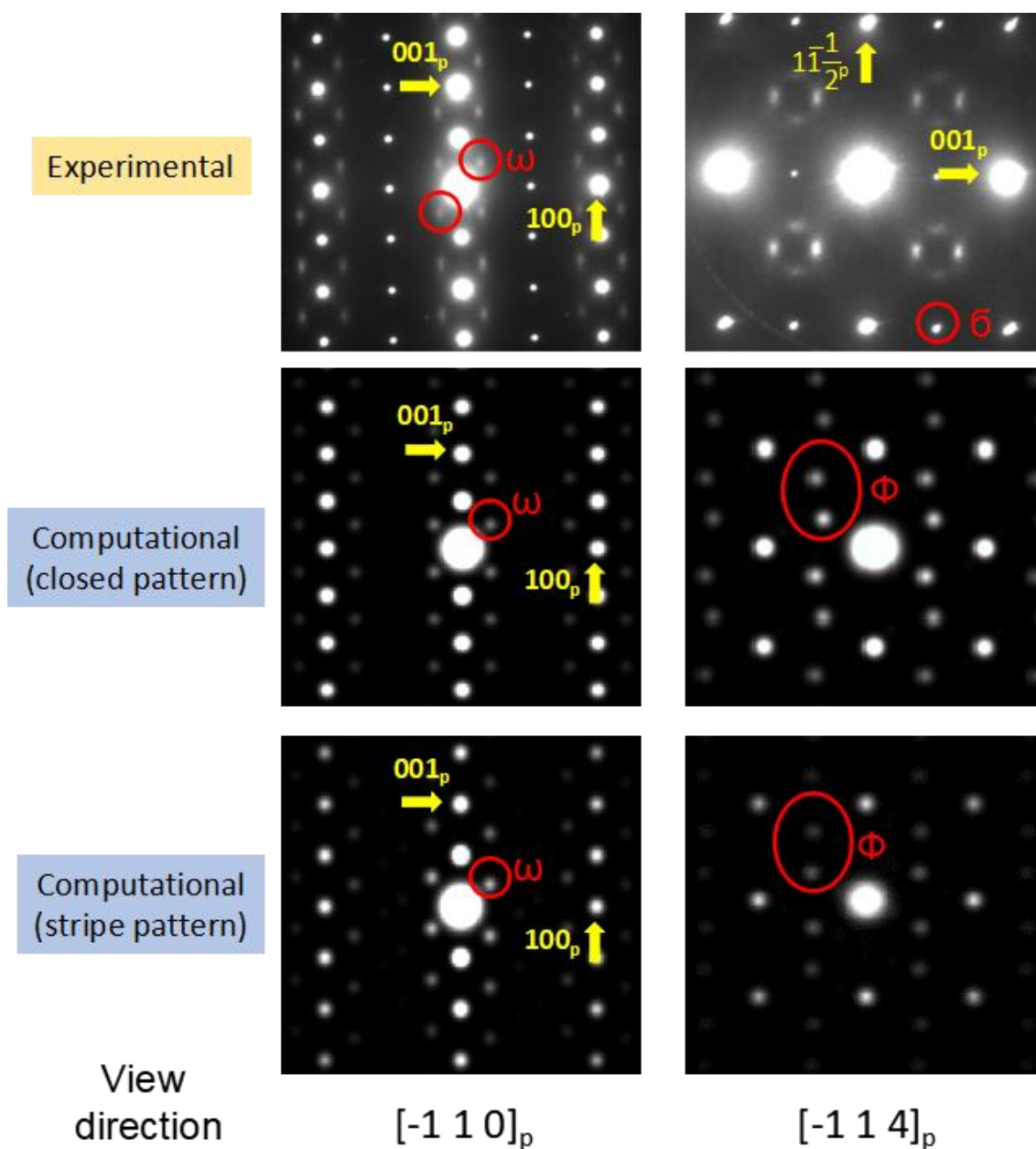


Fig. 2.16 Experimental and simulated selected area electron diffraction (SAED) patterns for $\text{La}_{1/3}\text{NbO}_3$. Extra spots are present at $(h/2\ k/2\ 2)_p$, which are labeled as $\{\delta\}$, and the labels $\{\omega\}$, $\{\Phi\}$ indicate two different kinds of superstructure spots.

2.4 Conclusion on Chapter 2

The structural features of $\text{La}_{1/3}\text{NbO}_3$ and the potential modes of the modulated structure of the La-rich layer were revealed using ab initio density functional calculations with cluster expansion and Monte Carlo simulation. The cluster expansion formalism was

suitable for calculating the total energy obtained using DFT calculation for an A-site-deficient perovskite structure. Based on MC simulation results, the structural feature of alternate La-rich and La-poor layer stacking along the c-axis was well reproduced when the supercell was even in size. The most stable La/vacancy arrangement in the La-rich layer of $\text{La}_{1/3}\text{NbO}_3$ was obtained by MC simulation with the supercell $12 \times 12 \times 12$; the arrangement was composed of several $4a_p \times 6a_p$ periodic units in which most of the La ions surrounded central vacancies, resulting in the formation of a closed arrangement. Moreover, a second potential La/vacancy arrangement with a slightly higher energy was found by simulating a $36 \times 36 \times 36$ supercell; this structural arrangement tends to exist in larger systems and at higher temperatures. The second arrangement is different from the first one in that there is no obvious ordered short-range structure, although a long-range ordered structure is observed along the diagonal direction $[1\ 1\ 0]_p$. Based on our results, we believe that these two different types of modulated arrangements will coexist in the real system, and closed arrangement with relatively low energy will account for the majority of the structure. It is foreseeable that when we dope Li-ions, most of them will occupy the center of the $4a_p \times 6a_p$ periodic units. La-ions around the corner of these $4a_p \times 6a_p$ periodic units will block the diffusion path of Li-ions, which may be the reason for the lower-than-expected Li ion conductivity in LLNO. Further study on the Li ion diffusion mechanism in the two arrangements is shown in Chapter 3.

References

1. Schwenzel, J., Thangadurai, V. & Weppner, W. Developments of high-voltage all-solid-state thin-film lithium ion batteries. *Journal of Power Sources* **154**, 232–238 (2006).
2. Li, J., Ma, C., Chi, M., Liang, C. & Dudney, N. J. Solid Electrolyte: the Key for High-Voltage Lithium Batteries. *Advanced Energy Materials* **5**, 1401408 (2015).
3. Adachi, G. Y., Imanaka, N. & Aono, H. Fast Li[⊕] conducting ceramic electrolytes. *Advanced Materials* **8**, 127–135 (1996).
4. Wang, Y. *et al.* Design principles for solid-state lithium superionic conductors. *Nature Materials* **14**, 1026–1031 (2015).
5. Takada, K. Progress and prospective of solid-state lithium batteries. *Acta Materialia* **61**, 759–770 (2013).
6. Belous, A., Pashkova, E., Gavrilenko, O., V'yunov, O. & Kovalenko, L. Solid electrolytes based on lithium-containing lanthanum metaniobates and metatantalates with defect-perovskite structure. *Ionics* **9**, 21–27 (2003).
7. Carrillo, L. *et al.* Superstructure determination of the perovskite $\beta\text{La}_{0.33}\text{NbO}_3$. *Journal of Materials Science* **35**, 3047–3052 (2000).
8. García-Martín, S. & Alario-Franco, M. Á. Modulated Structure of $\text{La}_{1/3-x}\text{Li}_3\text{NbO}_3$ $0 \leq x \leq 0.06$ Perovskite-Related Materials. *Journal of Solid State Chemistry* **148**, 93–99 (1999).
9. Gao, X. *et al.* Cation ordering in A-site-deficient Li-ion conducting perovskites $\text{La}_{(1-x)/3}\text{Li}_x\text{NbO}_3$. *Journal of Materials Chemistry A* **3**, 3351–3359 (2015).
10. Stramare, S., Thangadurai, V. & Weppner, W. Lithium Lanthanum Titanates: A Review. *Chemistry of Materials* **15**, 3974–3990 (2003).
11. Inaguma, Y., Katsumata, T., Itoh, M., Morii, Y. & Tsurui, T. Structural investigations of migration pathways in lithium ion-conducting $\text{La}_{2/3-x}\text{Li}_3\text{TiO}_3$ perovskites. *Solid State Ionics* **177**, 3037–3044 (2006).
12. Inaguma, Y., Chen, L., Itoh, M. & Nakamura, T. Candidate compounds with perovskite structure for high lithium ionic conductivity. *Solid State Ionics* **70–71**, 196–202 (1994).
13. Catti, M. First-principles modeling of lithium ordering in the LLTO ($\text{Li}_{x/2}\text{La}_{2/3-x/3}\text{TiO}_3$) superionic conductor. *Chemistry of Materials* **19**, 3963–3972 (2007).
14. Nakayama, M., Shirakawa, J. & Wakihara, M. Ab initio density functional study on changes in local structure in perovskite compound, $\text{Li}_x\text{La}_{1/3}\text{NbO}_3$. *Solid State Ionics* **177**, 1259–1266 (2006).
15. Fontaine, D. De. Cluster Approach to Order-Disorder Transformations in Alloys. in (eds. EHRENREICH, H. & TURNBULL, D.) **47**, 33–176 (Academic Press, 1994).
16. Ceder, G., Ven, A. Van der, Marianetti, C. & Morgan, D. First-principles alloy theory in oxides. *Modelling and Simulation in Materials Science and Engineering* **8**, 311–321 (2000).
17. Perdew, J. P., Burke, K. & Ernzerhof, M. Generalized gradient approximation made simple. *Physical Review Letters* **77**, 3865–3868 (1996).
18. Blöchl, P. E. Projector augmented-wave method. *Physical Review B* **50**, 17953–17979 (1994).
19. van de Walle, A. & Ceder, G. Automating first-principles phase diagram calculations. *Journal of Phase Equilibria* **23**, 348–359 (2002).
20. Van de Walle, A., Asta, M. & Ceder, G. The alloy theoretic automated toolkit: A user guide. *Calphad: Computer*

-
- Coupling of Phase Diagrams and Thermochemistry* **26**, 539–553 (2002).
21. van de Walle, A. Multicomponent multisublattice alloys, nonconfigurational entropy and other additions to the Alloy Theoretic Automated Toolkit. *Calphad* **33**, 266–278 (2009).
 22. Visualization and analysis of crystal structures using CrystalMaker software. *Zeitschrift für Kristallographie - Crystalline Materials* **230**, 559 (2015).
 23. Momma, K. & Izumi, F. *{VESTA3}* for three-dimensional visualization of crystal, volumetric and morphology data. *Journal of Applied Crystallography* **44**, 1272–1276 (2011).
 24. Nakayama, M., Ikuta, H., Uchimoto, Y. & Wakihara, M. Study on the AC Impedance Spectroscopy for the Li Insertion Reaction of $\text{Li}_x\text{La}_{1/3}\text{NbO}_3$ at the Electrode-Electrolyte Interface. *Journal of Physical Chemistry B* **107**, 10603–10607 (2003).
 25. Kawakami, Y., Ikuta, H. & Wakihara, M. Ionic conduction of lithium for perovskite-type compounds, $\text{Li}_x\text{La}_{(1-x)/3}\text{NbO}_3$ and $(\text{Li}_{0.25}\text{La}_{0.25})_{1-x}\text{Sr}_{0.5x}\text{NbO}_3$. *Journal of Solid State Electrochemistry* **2**, 206–210 (1998).
 26. Mishchuk, D. O., V'yunov, O. I., Ovchar, O. V. & Belous, A. G. Structural and dielectric properties of solid solutions of sodium niobate in lanthanum and neodymium niobates. *Inorganic Materials* **40**, 1324–1330 (2004).
 27. Klingler, M., Chu, W. F. & Weppner, W. Coulometric titration of substituted $\text{Li}_x\text{La}_{(2-x)/3}\text{TiO}_3$. *Ionics* **3**, 289–291 (1997).
 28. Newman, M. E. J. & Barkema, G. T. *Monte Carlo Methods in Statistical Physics*. (Clarendon Press, 1999).
 29. Whitfield, T. W. & Martyna, G. J. Low variance energy estimators for systems of quantum Drude oscillators: Treating harmonic path integrals with large separations of time scales. *Journal of Chemical Physics* **126**, (2007).
 30. Hu, X. *et al.* Structural changes and their effect on Li-ion conductivity upon quenching of $\text{La}_{(1-x)/3}\text{Li}_x\text{NbO}_3$ solid electrolytes. *Acta Materialia* **156**, 379–388 (2018).
 31. Reaney, I. M., Colla, E. L. & Setter, N. Dielectric and Structural Characteristics of Ba- and Sr-based Complex Perovskites as a Function of Tolerance Factor. *Japanese Journal of Applied Physics* **33**, 3984 (1994).

Chapter 3 Explore the diffusion mechanism of Li-ions in different modulated arrangements of $\text{La}_{(1-x)/3}\text{Li}_x\text{NbO}_3$ with the fitted force fields obtained via metaheuristic algorithm

3.1 Introduction

As mentioned in Chapter 2, Lanthanum lithium niobite (LLNO) was selected as another attractive candidate for fast Li-ion conduction, since there are more intrinsic vacancies in LLNO, and the unit cell volume is larger.^{1,2} Thus higher ionic conductivity is expected in LLNO than in LLTO, because LLNO has these advantages in terms of structure. However, according to the current reports, the highest bulk ionic conductivity of LLNO is about $\sim 10^{-4}$ S/cm at room temperature,³ which is much lower than that of LLTO. Similar to LLTO, there is a long-range interlayer modulated structure in LLNO, which is exhibited as an alternate La-rich layer and La-poor layer as shown in Figure 3.1 (For low Li content LLNO, both Li and La atoms are confined to the La-rich layer, leaving the La-poor layer empty.⁴ Here, we used the crystal structure of $\text{La}_{1/3}\text{NbO}_3$ to exhibit the alternate inter-layer arrangement of LLNO). However, in LLNO, due to the excessively high cation vacancy concentration, a quasi-periodic ordered arrangement of La/Vac appears in the La-rich layer, which is absent in LLTO.⁵ The previous studies have proved that there is some kind of modulated structure of La/Vac within La-rich layers.^{5,6} However, due to the limitation of conventional experimental characterization, it is hard to reveal these modulated structures on the atomic scale. Our previous work (Chapter 2) has revealed possible patterns of this modulated structure within the La-rich layer of LLNO, with the help of density functional theory (DFT) calculation, cluster expansion and Monte Carlo simulation.^{7,8} The La atoms and vacancies in La-rich layer will rearrange at low temperature by different patterns, and finally showed up as two different quasi-period ordered arrangements (one is closed pattern arrangement, the other one is stripe pattern arrangement, for more detail can check our study⁹(Chapter 2)), as shown in Figure 3.1. Due to the reason that there is barely no difference of system's energy composed by these two modulated arrangements, so we suppose that in the real LLNO system, these two

arrangement can co-exist, and this is supported by agreement between experimental and computational electron diffraction patterns.⁹ For the Li-ion conduction in perovskite-type material, the crystal structure and atomic arrangement will strongly effect the performance.^{10,11} So far, regarding the analysis of Li-ion diffusion mechanism in LLNO basically did not include the influence of this modulated arrangement within La-rich layer.

About the Li-ion diffusion process in the LLNO, as the previous studies report that the Li-ion will migrate through the O₄ window position composed by the NbO₆, this migration process mainly occurs within the La-rich layer and within La-poor layer only play a minor role. Because in previous studies, whether it is experimental characterization or computational simulation, there is no accurate description of the modulated arrangement of cation/Vac which existing in the La-rich layer, so whether the modulated structure on the La-rich layer has an effect (what kind of effect) on the Li-ion migration is not yet known.

To evaluate the Li-ion diffusion mechanism in LLNO, the following approaches are reported, molecular dynamics (MD),^{12,13} nudged elastic band method (NEB),^{14,15} kinetic Monte Carlo (KMC)¹⁶, and percolation analysis.¹⁷ Among all these methods, MD should be the most powerful one and has been widely used to evaluate the ionic migration in the solid system, since it is no need for a priori assumptions of migration path of Li. However, using the MD approach to evaluate the Li-ion diffusion mechanism in LLNO also have some requirements, the most important is an accurate description of interatomic interactions. Ab initio MD (AIMD) based on density functional theory (DFT), is the most accurate, because the description of the interaction between atoms is derived from the quantum mechanics calculations.^{18,19} However, AIMD is computationally demanding, as normally AIMD can only apply to the small system within 1000 atoms, and the simulation time on a sub-nano second level. Due to the cell size of our target LLNO systems is larger than above limitations (in this part of work, all the four simulation systems are over 7000 atoms). Thus, we need to rely on an fast empirical force-fields (FFs) to perform MD simulation (FFMD), in which the calculation accuracy depends on the potential parameters for FFs. To overcome accuracy and computational cost derived trade-off, we used MD calculations using DFT derived FF parameter sets as described below, in this study.

In this Chapter, we investigate the Li ion conduction behavior for both modulated

and disordered structures in terms of La/Vac arrangement by MD at first time based on the Chapter. 2 MC simulation results. To satisfy both fast and accurate simulation, FFMD simulations derived from density DFT by metaheuristics approach are performed to investigate migration behavior of Li in LLNO compounds. The reporting content is mainly based on the following aspects:

1. The goodness of CS algorithm performed fitted FFs for MD calculation.
2. How does the modulated arrangement of LLNO affect the Li-ion migration.

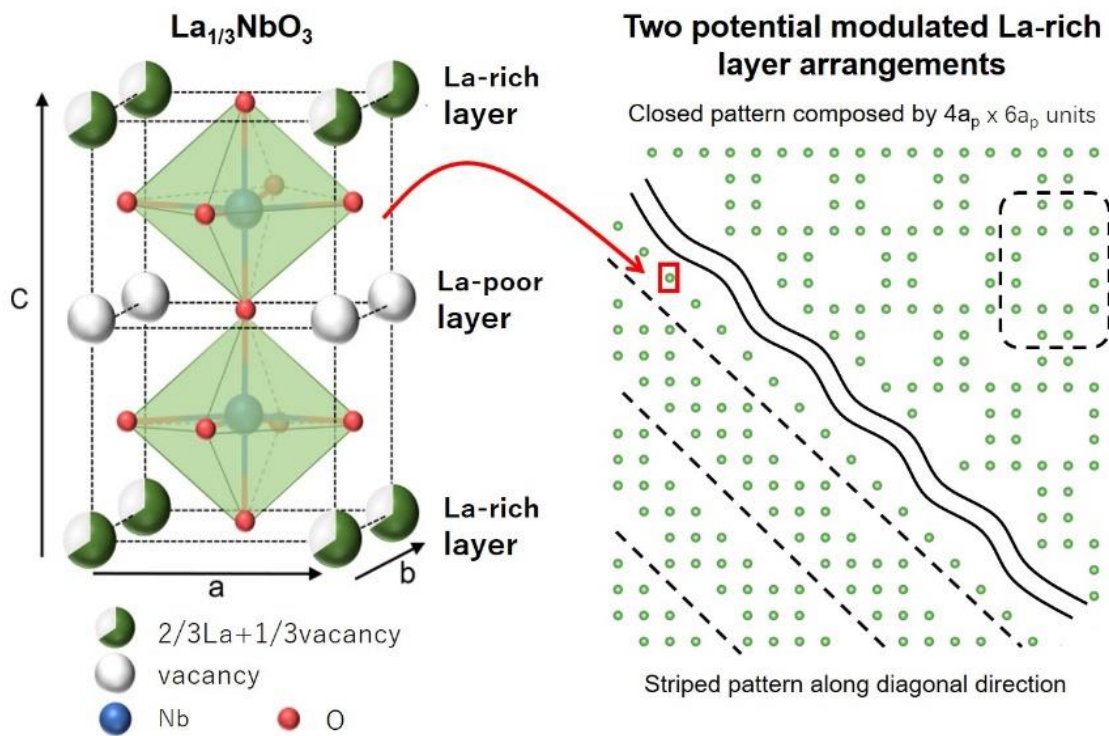


Fig 3.1 Crystal structure of $\text{La}_{1/3}\text{NbO}_3$ showing La-rich ($1/3$ vacancies) and La-poor (all vacancies) layers. Two potential modulated arrangements of La/Vac in La-rich layer of LNO revealed by our previous work.

3.2 Research Method

In this chapter, empirical FF parameters for LLNO systems are determined by two steps; 1) the radial distribution functions (RDF), angular distribution functions (ADF), and equilibrium volume are obtained by AIMD (the reference data), and 2) FF parameters are optimized to adjust above AIMD outputs by Cuckoo Search (CS) algorithm, known

as one of the metaheuristic approach. Detailed computational settings are described as follows.

3.2.1 Ab initio Molecular Dynamics (AIMD)

AIMD calculations have been performed for a smaller system $\text{Li}_6\text{La}_{10}\text{Nb}_3\text{O}_{108}$ (the snapshot of this training system structure as shown in Figure 3.2 with alternate La-rich and La-poor structure was produced to simply mimic our target system. About the AIMD calculation involved in this paper was conducted by the Vienna ab initio simulation package (VASP),²⁰ with the method of the projector augmented wave (PAW)²¹ to generate the pseudopotential. The exchange-correlation was described by generalized gradient approximation (GGA)²² and specified as the PBEsol²³ functional. In addition, the cutoff energy was set as 500 eV, and only Γ -point was used. The NPT ensemble was employed in this calculation, and the total simulation time is 1.5 ps with 1500 ionic steps, to ensure the system reach equilibration, the first 500 steps' data were abandoned. The RDF, ADF and equilibrium volume are calculated by averaging ionic configurations extracted every 10 steps. RDF and ADF profiles are smeared with the Gaussian function is fixed to 0.1 Å and 2.0 °, respectively. In the process of optimizing the force field parameters, the same system ($\text{Li}_6\text{La}_{10}\text{Nb}_3\text{O}_{108}$ with the same initial cell vectors) and the same procedure of obtaining the reference data (RDF, ADF, cell volume) were employed to ensure the data is comparable.

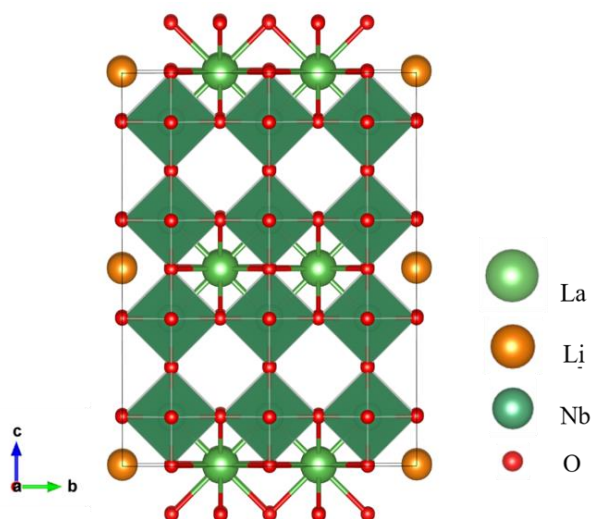


Fig 3.2 The snapshot of the structure of $\text{Li}_6\text{La}_{10}\text{Nb}_3\text{O}_{108}$, selected as the training system, performed by AIMD calculation.

3.2.2 The Fitted Force Field Model

The force field model used in this work consists of two parts, i.e. two-body potential term and three-body one. Two body one is an empirical form of FF which is similar to BVS-FF,²⁴ consisting of the screened Coulomb potential for the interaction between the same sign charges (anion-anion and/or cation-cation) and the Morse potential for the interaction between the opposite sign charges (cation-anion).

The screened Coulomb potential with the complementary error function is as below:

$$U(r_{ij}) = \frac{1}{4\pi\epsilon_0} \frac{q_i q_j}{r_{ij}} \operatorname{erfc}\left(\frac{r_{ij}}{\rho_{ij}}\right) \quad (3-1)$$

Where q_l is the charge on the atom labeled l , and r_{ij} is the magnitude of separation vector $r_{ij} = r_i - r_j$. ρ_{ij} is the sum of effective radii of ions used to evaluate the screening length and it is also the optimizing parameter, ϵ_0 is the permittivity of vacuum.

The Morse potential which used to calculate the interaction of cation and anion is of the form:

$$U(r_{ij}) = D_e \{ \exp[-2\alpha(r-r_e)] - 2\exp[-\alpha(r-r_e)] \} \quad (3-2)$$

Here D_e is the well depth defined by the dissociated atoms, and α control the ‘width’ of the potential, r is the distance between the interacting atoms, r_e is the equilibrium bond length. D_e , α , r_e are the optimizing parameters.

All potentials must have a finite range in order to be calculable, but where there is a cut-off boundary, there will be a discontinuity in the energy for most interaction terms, to avoid this discontinuity in the energy, a constant shift can be added to the potential, and to make the gradient is also zero at the cut-off distance, the procedure can be extended by adding a linear term in the distance.

$$\hat{U}(r_{ij}) = U(r_{ij}) - U(r_{\text{cut}(2b)}) - (r_{ij} - r_{\text{cut}(2b)}) \frac{dU(r_{ij})}{dr_{ij}} \quad (3-3)$$

As we mentioned above, to improve the performance of the fitted force field, it is helpful to add a description of angular between selected bonds. For the tetrahedra or octahedra that commonly exist in the SSE material, the introduction of angular potential will help to form a more accurate framework structure. Since the Stillinger-Weber(SW) potential considers the effects of bond length and bond angle when calculating the three-body interaction, it is feasible to take the form of SW potential as the angular description.

$$U(r_{ijk}) = \lambda \exp \left[\left(\frac{1}{r_{ij} - r_{\text{cut}(3b)}} \right) + \left(\frac{1}{r_{ik} - r_{\text{cut}(3b)}} \right) \right] (\cos \theta_{ijk} - \gamma)^2 \quad (3-4)$$

Where r_{ij} and r_{ik} are the bond length between the two adjacent atoms, and θ_{ijk} is the angle of this three-body configuration. The λ , γ are optimizing parameters. Since the evaluation of the three-body terms is more complicated, to increase the efficiency of calculation, $r_{\text{cut}(3b)}$ is fixed to 3.5 Å only take consideration of the nearest three-body configuration. As for $r_{\text{cut}(2b)}$, is fixed to 5.0 Å in this chapter.

3.2.3 Optimize FFs parameters by nature inspired algorithm

To optimize these FF parameters automatically, a nature inspired optimization algorithm called Cuckoo Search (CS)²⁷ was utilized in this work. As a metaheuristic algorithm, this method is based on the cuckoo's brood parasitism behavior, and the algorithm can be enhanced by the so-called Levy flight,²⁸ rather than a simple isotropic random walk. Compared with the genetic algorithm (GA), particle swarm optimization (PSO) and other algorithms, the CS algorithm has been proved with better performance in optimize efficiency and global convergence.²⁹ There are some hyper-parameter in the CS, but only the individuals number of one generation (nests number) N_n and random search fraction (the fraction of nests that cannot be inherited to the next generation) P_n are the key parameters. Previous studies have shown that $N_n=15\sim40$ and $P_n=0.25$ are sufficient for most optimization cases, and the convergence rate is not sensitive to these parameters,²⁸ so N_n was fixed to 18 and P_n was fixed to 0.25 in this part of study. The pseudo-code of CS is shown in Figure 3.3.

Cuckoo Search via Levy Flights	
1	Objective function: $f(x)$, $x = (x_1, \dots, x_n)^T$
2	Generate an initial population of n host nests
3	while ($t < \text{MaxGeneration}$) or (Stop criterion) do
4	Get a cuckoo randomly (say, i) and replace its solution by performing Levy flights
5	Evaluate its quality F_i
6	Choose a nest among n (say, j) randomly
7	if ($F_i < F_j$) then
9	Replace j by the new solution
10	end if
11	A fraction (P_n) of the worse nests are abandoned and new ones are built
12	Keep the best solution/nests
13	Rank the solution/nest and find the current best
14	Pass the current best solutions to the next generation
15	end while

Fig 3.3 Pseudo code of the cuckoo search for a minimization problem

Since the random walk (the Levy flight also can count as a special random walk) is involved in the CS algorithm, it may produce a solution that exceeds the feasible range, it is necessary to set an automatically update lower and upper bounds to limit the search space of each optimizing parameter sets. The update process of the bounds is based on the following scheme: ¹. Initialize: manually set the bounds of each parameter before the optimization procedure starts. ². Ranking: rank all the optimizing parameter sets in every N generation based on the loss function value L, and the top M sets are taken for next step. ³. Changing: take the minimum and maximum values of each optimizing parameter among these M sets and replace the upper and lower bounds with the extracted values. ⁴. Expanding: update the range of upper and lower bounds to ensure that the current best parameters will locate in bounds' center. Here N and M are the empirical parameters based on our test runs, and these two parameters are fixed to 10 and 100, respectively.

3.2.4 The loss function

In the machine learning process, configuring the loss function is an important step to ensure that the model works in the expected way. The loss function³⁰ is used as a standard to evaluate the difference between the predicted value (in this work, these predicted values obtained by FFMD using the current fitted FFs) and the true value (obtained by AIMD). Generally, the better the loss function, the better the performance of the training model. However, the loss functions used by different models are generally different. It's our purpose to quickly generate sufficiently accurate FFs, to ensure the efficiency of the evaluation process, RDFs $g(r)$, ADFs $h(\theta)$, and equilibrium volume V were selected as the evaluated objects, the loss function was defined as the sum of squared differences of all these three.

$$L = L_R + L_A + L_V \quad (3-5)$$

$$L_R = \frac{1}{N_p} \sum_p \left(\frac{\sum_{i=1}^{N_R} (g_{p_{FF}}(r_i) - g_{p_{AI}}(r_i))^2}{\sum_{i=1}^{N_R} (g_{p_{AI}}(r_i))^2} \right) \quad (3-6)$$

$$L_A = \frac{1}{N_t} \sum_t \left(\frac{\sum_{i=1}^{N_A} (h_{t_{FF}}(r_i) - h_{t_{AI}}(r_i))^2}{\sum_{i=1}^{N_A} (h_{t_{AI}}(r_i))^2} \right) \quad (3-7)$$

$$L_V = \frac{(V_{FF} - V_{AI})^2}{V_{AI}^2} \quad (3-8)$$

Here N_p and N_t represent the total number of different species of two-body and three-body terms respectively, the subscripts p and t indicate a specific species of pairs

and triples. The resolution of radial distribution is 0.05\AA , so the total sampling points N_R is fixed to 100. As for the angular distribution, sampled every degree, so N_A is fixed to 180.

In this chapter, except the AIMD calculations were carried out by VASP, all the FFMD calculation and metaheuristic optimization of FFs were performed by software NAP.³¹³²

3.3 Result and Discussion

3.3.1 The goodness of CS algorithm performed fitted FFs for MD calculation.

3.3.1.1 Check the Loss function value of the fitted FFs parameters

The loss function value L of each fitted FF parameter sets generated during the optimization has shown in Figure 3.4(a). It can be clearly found from the plot that the lower limit of the loss function continues to decrease with the CS optimization process. The CS algorithm has been performed with high efficiency, after about 100 generations, the optimal loss function value almost reached the stop criterion, and at the end of optimization, this value has converged sufficiently small ($L = 0.0093$). Figure 3.4(b) displays the distribution of some selected optimization parameters ($D_e(\text{Li-O})$, $\alpha(\text{Li-O})$, $R_e(\text{Li-O})$) with the loss function value of corresponding generation. It can be found that the range of these parameters keep shrinking during the optimization, and each parameter seem to converge in the range between the lower and upper bounds of the search space. The width of the Morse potential, $\alpha(\text{Li-O})$, are converged into two parameters, $\sim 2.15\text{\AA}$ and $\sim 2.45\text{\AA}$, during the optimization, and the present CS optimization finally determines global minimum as ~ 2.45 according to the loss function. This indicates that the CS algorithm was performed well both for global and local optimization.

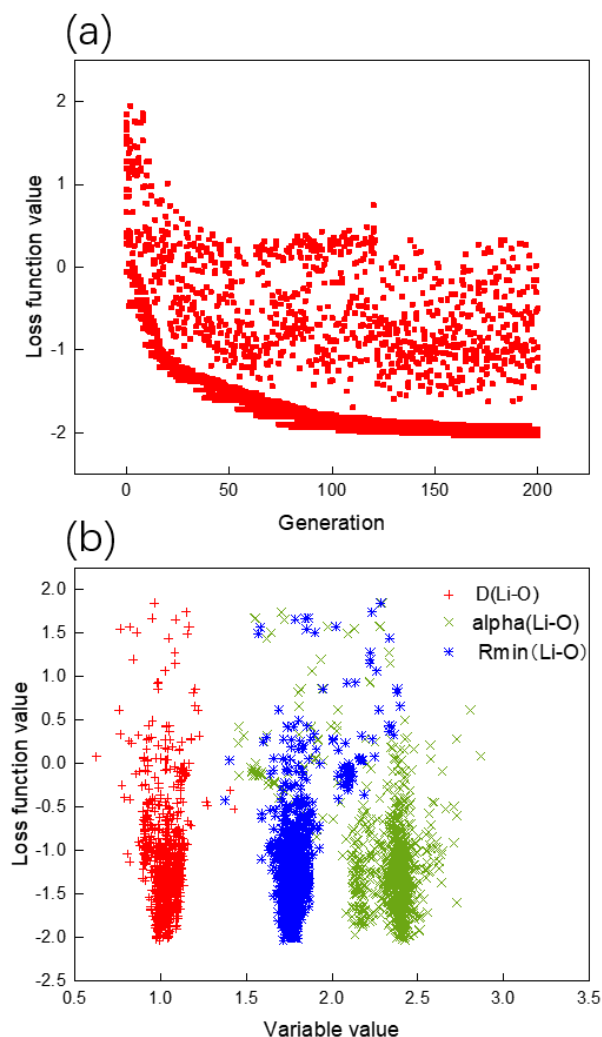


Fig 3.4 (a) The loss function value L of each fitted FFs generated during the CS optimization. (b) The distribution of selected optimization parameters $D_e(\text{Li-O})$, $\alpha(\text{Li-O})$, $R_e(\text{Li-O})$ against with the loss function value.

3.3.1.2 Comparison of the data obtained via AIMD and FFMD

The RDFs and ADFs of selected pairs interaction and three-body terms are shown in Figure 3.5(a) and 3.5(b), respectively. It's clearly to observe that the plot obtained by our fitted force field parameters almost overlap with the plot obtained by AIMD and show better consistency than the result of BVS-ff. The improvement of accuracy proves that it's worthy to introduce the angular potential to aid in forming the framework structure. Since this fitted FF show better performance on the training system ($\text{Li}_6\text{La}_{10}\text{Nb}_{36}\text{O}_{108}$), we apply it to our target system with good confidence.

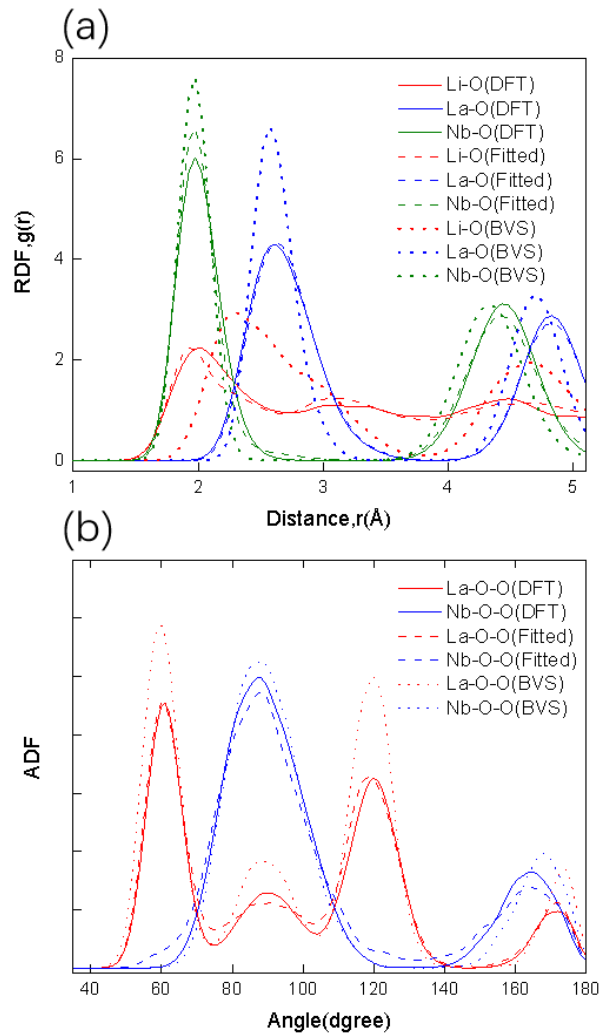


Fig 3.5 (a) RDFs of selected pairs interaction, Li-O, La-O, and Nb-O, obtained via AIMD and FFMD, which includes the fitted force field parameters optimized by Nap and another one is BVS-ff based on the previous study. (b) ADFs of selected three-body terms, La-O-O and Nb-O-O, obtained via AIMD and FFMD (fitted FF and BVS-ff).

3.3.2 How does the modulated arrangement of LLNO affect the Li-ion migration.

3.3.2.1 The ionic conductivity of Li-ion in the different modulated structures

After we obtained the fitted FF with the performance comparable to DFT calculation, the NVT-MD calculations were conducted to the perovskite-type LLNO with different modulated structures, using the fitted FF, in which the potential parameters have listed in Table 3.1. According to our previous research work⁹, there are two potential modulated structures of La/Vac in the La-rich layer, to comprehensively analyze the influence of the modulated structure on the diffusion of Li-ions in the bulk, we created the other two

systems (La-rich layer random arrangement, totally random arrangement, the detail of these modulated structures as shown in Figure 3.6.) for the purpose of comparison.

Table 3.1. The optimizing parameters of fitted FF obtained by CS. where qx indicates the nominal charge of species X, r_x^{ion} is the sum of effective radii of ions X used to evaluated the screening length, $D_{e,xo}$ is the well depth defined by the dissociated atoms, α_{xo} indicates the width of the potential, $r_{e,xo}$ is the equilibrium bond length, (subscript xo represents the cation species X and anion O). λ_{oxo} is the depth of potential well, γ_{oxo} indicates the equilibrium angle, (subscript oxo represents the triplet O-X-O).

X (qx)	r_x^{ion} (Å)	$D_{e,xo}$ (eV)	α_{xo} (Å)	$r_{e,xo}$ (Å)	λ_{oxo} (eV)	γ_{oxo}
Li (1)	1.0402	0.9952	2.4249	1.7149	---	---
La (3)	0.9619	1.2693	2.1500	2.2390	1.2753	0.4933
Nb (5)	0.8300	2.6528	2.1169	1.8110	0.8219	-0.6898
O (-2)	0.7911	---	---	---	---	---

Fig 3.6 The snapshot of LLNO structure, the first type has the alternate La-rich and La-poor layer structure including three different modulated La/Vac arrangements in La-rich layer, (1) Close arrangement, (2) Stripe arrangement, (3) La-rich layer random arrangement. The second type does not has the alternate layer structure, (4) totally random arrangement.

Figure 3.7(a) shows the simulation time dependent mean square displacement (MSD) of ions in the LLNO system with the stripe arrangement (see Figure 3.8 for more

detail of MSD data of other modulated structures), it is clear to observe that only Li-ions diffuse in the structure, and other ions hold their original position basically. This also proves that using the fitted FF obtained by CS can simulate the Li-ion migration in the LLNO system with high performance. Figure 3.7(b) displays the Arrhenius plots of LLNO system with different modulated arrangements, indicating that the La/vacancy arrangement in A-sites largely affect the ionic conductivity of Li. The activation energies of Li-ion diffusion in each different arrangements were calculated from the slope fitted to the data points. The activation energy of Stripe arrangement is 0.304 eV which is lower than other three, and compared with an experimental value, 0.325 eV.³ It can be found that the experimental value is between the closed system and the striped system value, which also proves that the real LLNO material is composed by these two modulated structures. Interestingly, both the random arrangement models for La/Li/vacancies show much lower Li ion conductivity, so that both the modulated structures promote ionic conductivity. Indeed, the Li ion conductivities of two modulated structures (closed and stripe arrangement models) are higher than those of disordered structures (La-rich random and totally random models) by a factor of 10 at 800K.

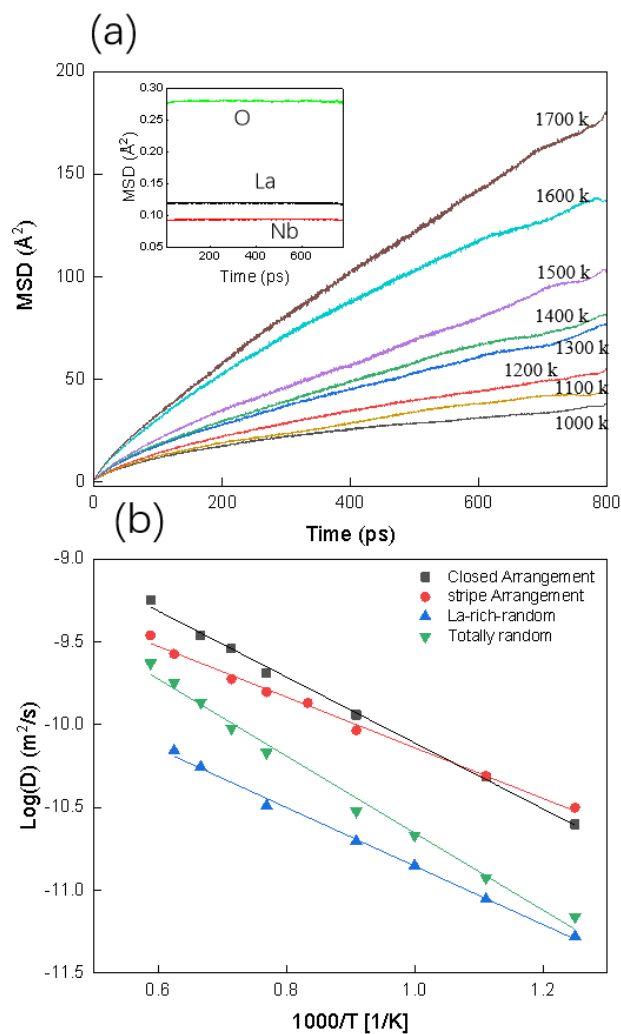


Fig 3.7(a) MSD of Li-ion in the LLNO system with the stripe arrangement of La/Vac, the data was compared at different temperatures. The illustration displays the MSDs of La, Nb and O ions at 1000 K. (b) Arrhenius plot of Li-ion diffusion coefficient vs $1000/T$, the activation energies of Li-ion diffusion in each different arrangements were calculated from the slope fitted to the data points.

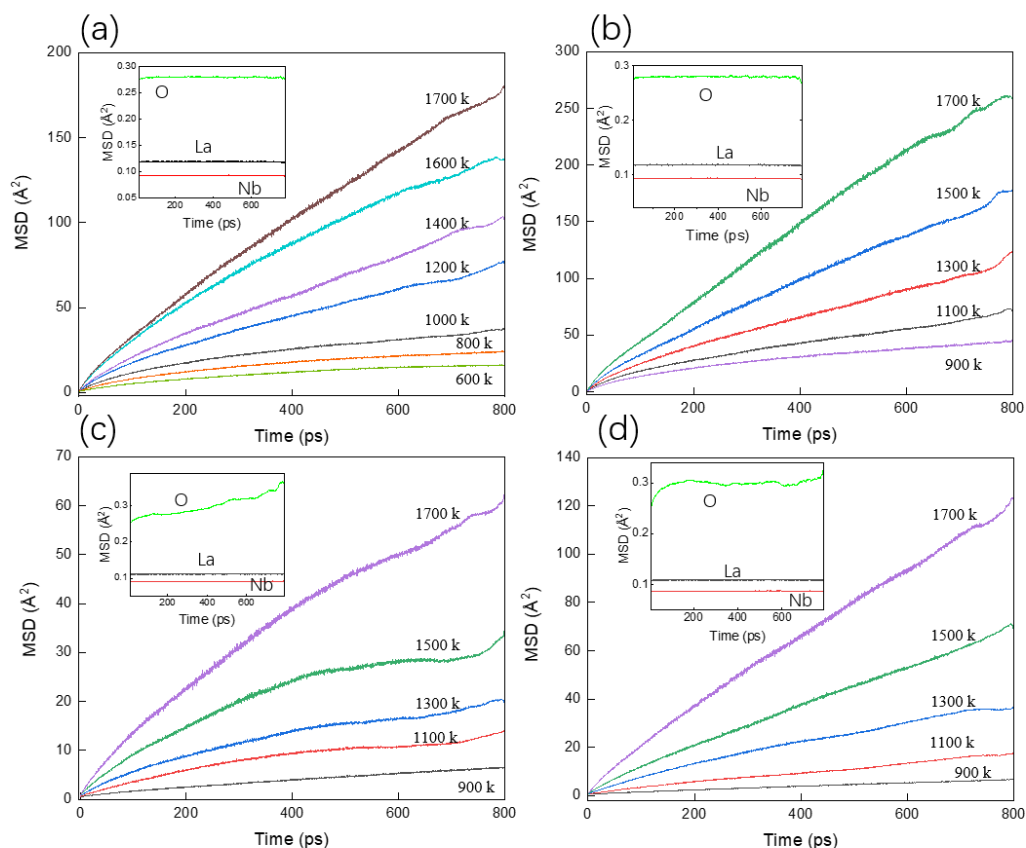


Fig 3.8(a), (b), (c), and (d) correspond to the striped arrangement, closed arrangement, La-rich random arrangement, and totally random arrangement, respectively. Each figure shows the MSDs of Li ions at different temperatures. The inset shows the MSDs of La, Nb, and O at 1000 K.

3.3.2.2 The influence of alternate inter-layer on the Li-ion migration

In the LLNO system, except the modulated arrangement of La/Vac in La-rich layer, the alternate arrangement of La-rich layer and La-poor layer along *c*-axis can also be considered as a kind of inter-layer modulated structure. This alternate inter-layer arrangement was also observed in the LLTO, and the Li and La atoms are located in both La-rich and La-poor layers, and the Li migration mainly occurs within the La-poor layers where there are more available A-site vacancies.^{5,33} In the case of LLNO with low Li content, the previous studies have confirmed that both Li and La atoms are located in La-rich layer, leaving the La-poor layer empty.⁴ Compared to the LLTO, the higher intrinsic vacancies concentration in the LLNO was attributed to the existence of La-poor layer, tracing the Li-ion diffusion trajectory is helpful to understand the influence of this

alternate layer arrangement of La/Vac in the LLNO system on the diffusion process. Figure 3.9 shows the isosurface plots of Li-ion probability density in the closed arrangement structure at different temperatures for closed arrangement system of LLNO. The yellow region represents the Li-ion diffusion pathway during the FFMD calculation, and the 2D Li-ion diffusion in LLNO is clearly visible along *ab*-plane at low temperature. In detail, the Li migration mainly occurs in the La-rich layer, and the intensity of Li-ion migration across and within the La-poor layer is very weak. Although the A-site vacancies concentration in the La-poor layer is much higher than that in the La-rich layer, the number of events that Li-ions located in the La-rich layer hop into the La-poor layer is limited during MD process at low temperature. This 2D diffusion tendency vanishes with the increasing of temperature, and Li ion migration along *c*-axis increases significantly. Likewise, selective Li occupation at La-rich layer is observed for the stripe arrangement and La-rich layer random arrangement models as well as the closed arrangement (Figure 3.9). Therefore, we infer that the La-rich/La-poor staking along *c*-axis is mainly ascribed not to the modulated arrangements of La/vacancies in La-rich layer, but to the Coulomb interactions as reported in our previous work.³⁴ Li-ion migration tends to occur within the La-rich layer at low temperature, ascribed to the NbO₆ tilting induced by the alternate inter-layer arrangement. Also, Nb atoms' modulated displacement intensifies with the Li atoms confined to the La-rich layer, which causes the bottlenecks of the O₄ window to get narrower, leading to higher migration energy barriers between the La-rich and La-poor layer.^{5,35}

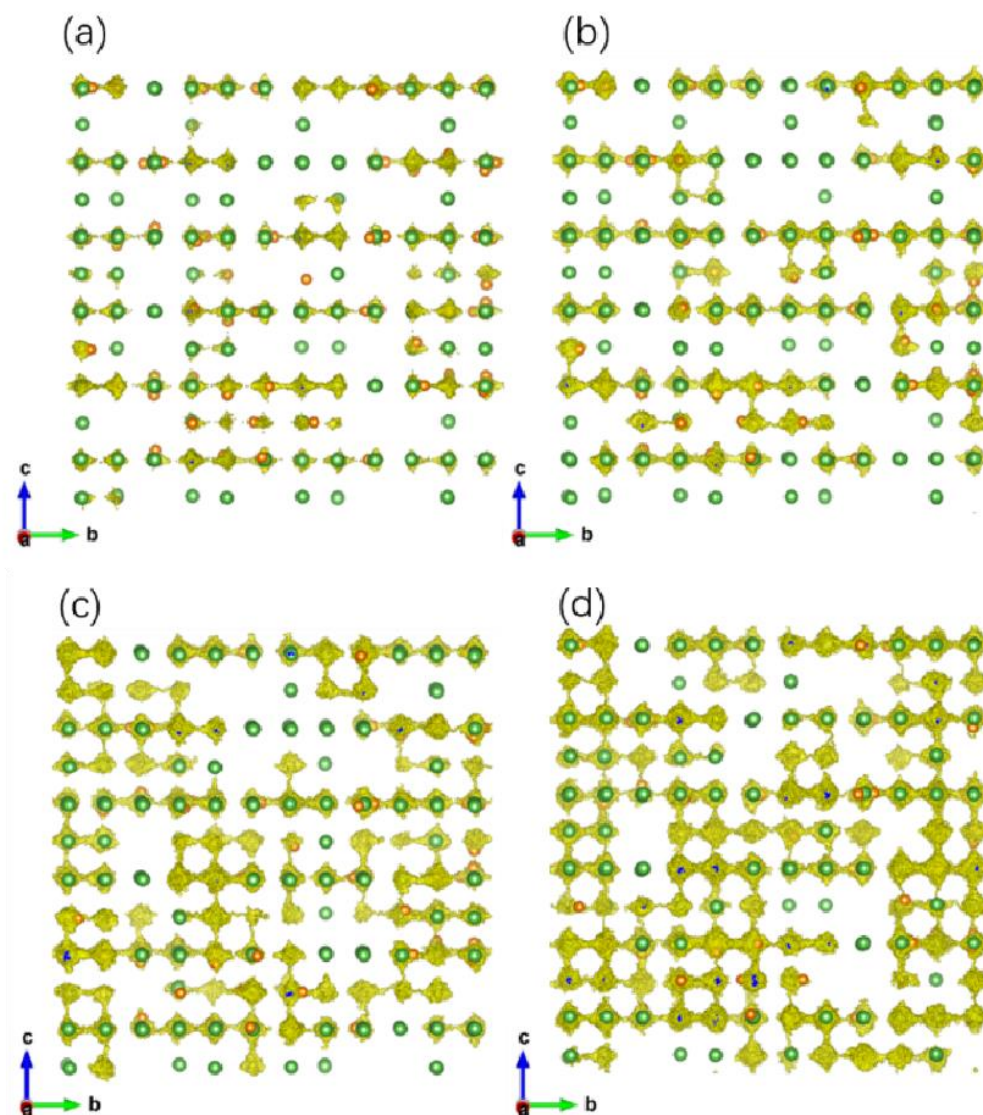


Fig 3.9 Isosurface plots of Li probability density in the closed arrangement structure of LLNO system, NbO_6 octahedrons have been deleted from the snapshot, green and orange dots represent La atoms and Li atoms. From (a) to (d) represent the simulation results under 400 K, 800 K, 1000 K, and 1400 K, respectively.

To further analyze this Li-ion migration behavior, the total diffusion coefficient D_{Li} of Li-ion was separated along a, b, c direction according to their contribution. As shown in Figure 3.10, it can be clearly found that as long as there is an alternate inter-layer arrangement in the structure, the diffusion coefficient along the c axis is about 1~2 orders of magnitude lower than that along the a and b directions at low temperature (< 400 K). The migration of Li-ions along the c-axis is enhanced with temperature. When the

simulated temperature rises to 1200 K, the diffusion coefficients of Li-ions in different directions are basically the same. This implies that the migration energy of Li along c axis is much higher than that along a or b axis. Li migration map of different arrangement structure systems as shown in Figure 3.11, the distribution of Li-ion in the structure were displayed along c axis and a axis to distinguish the difference of potential energy between La-rich layer and La-poor layer. It can be clearly seen from Figure 3.11 that the potential energy of Li-ions in the La-poor layer is higher than that in the La-rich layer. There are more high-energy dots shown in La-poor layers than La-rich layers. This potential energy gap caused by the modulated arrangement inside the LLNO may explain why the diffusion mode of Li-ions at low temperatures is closer to 2D rather than 3D.

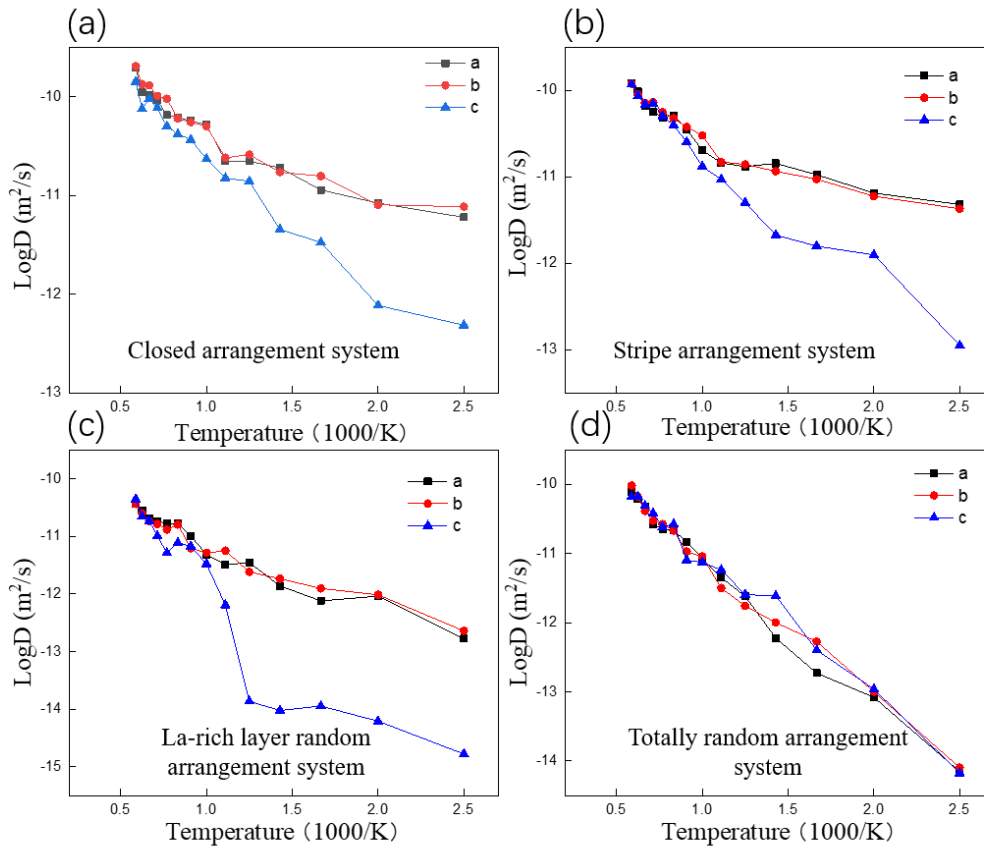


Fig 3.10 Logarithm of the diffusion coefficients of Li ions along different axes as a function of 1000/K. (a), (b), (c), and (d) represent the closed arrangement system, striped arrangement system, La-rich layer random arrangement system, and totally random structure, respectively.

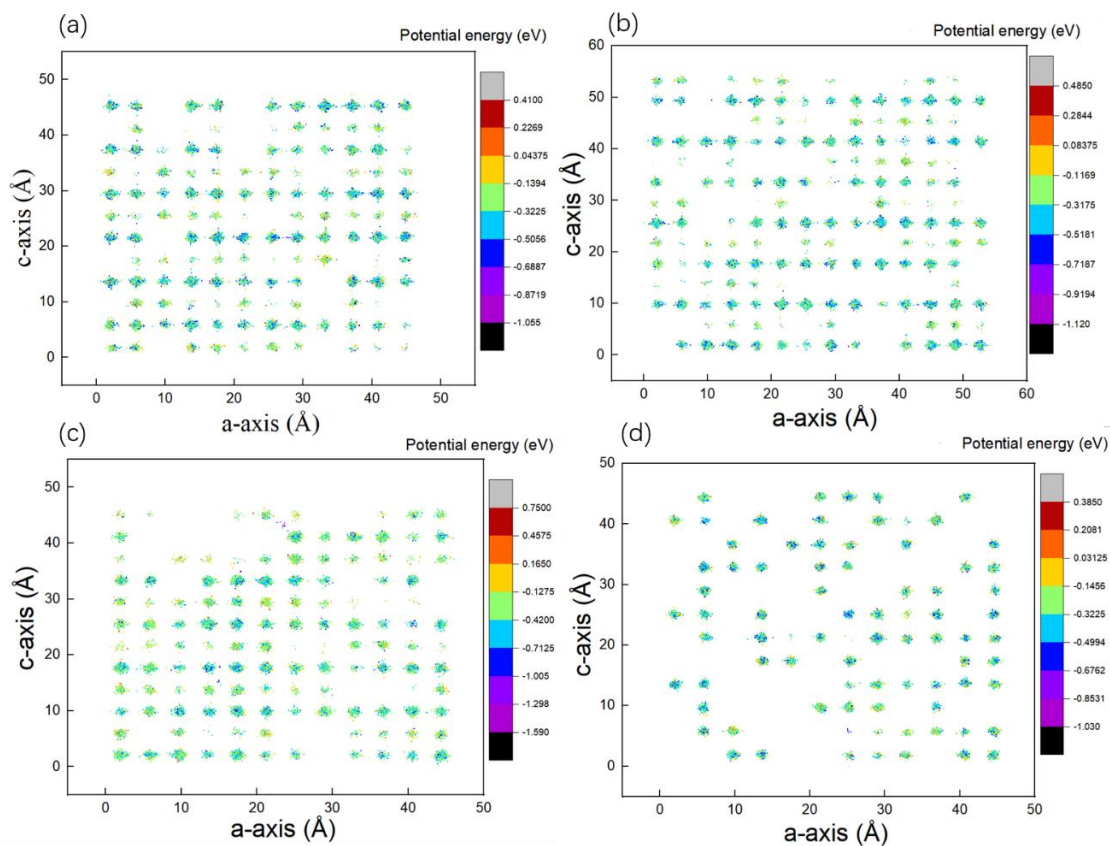


Fig 3.11 Li migration maps of different arrangement systems, from (a) to (d) correspond to Closed arrangement structure, striped arrangement structure, Li-rich random structure, and totally random structure, respectively.

Although the Li-ion in the La-rich layer cannot fully utilize the A-site vacancies in the La-poor layer due to the existence of the inter-layer modulated structure, this modulated structure does not only play a negative role in the diffusion of Li-ions. Figure 3.10(d) shows the diffusion coefficient of Li-ions along with different directions in the totally random arrangement structure, this artificially created structure does not have alternate inter-layers or special inner-layer arrangements. Contrary to expectations, the diffusion coefficient of Li-ions at low temperature does not increase with the disappearance of the alternate inter-layer arrangement, and this is much lower than the other three structures (Figure 3.7(b)). The activation energy for Li-ion conduction in this totally random structure is 0.497 eV as shown in Figure 3.7(b), which also proves that the ion conduction performance of LLNO will get worse, if there is no modulated arrangement structure in the LLNO. Consider the reasons for the formation of various modulated structures in LLNO, the energy of the LLNO system will gradually decrease

with the formation of these modulated structures, especially the modulated inter-layer arrangement, as a long-range ordering structure, it plays a major role in the stability of the LLNO system. Therefore, the complete elimination of the modulation structure reduces the structural constraints on Li-ion diffusion and enhances the utilization of the intrinsic A-site vacancies, but the consequence is that the internal energy of the system largely increases, and the stability decreases. These unfavorable factors may affect the diffusion of Li-ion in the LLNO.

3.3.2.3 The influence of modulated arrangement of La/Vac of La-rich layer on the Li-ion migration

To further analyze the 2D migration behavior at the La-rich plane, we tracked the diffusion trajectory of each Li-ion in our calculation systems. Figure 3.12(a) shows the diffusion trajectory of Li-ion in the selected region of La-rich layer in closed arrangement system of LLNO. It is found that the Li-ion diffuse freely in this closed arrangement at La-rich layer, but the surrounding La-ions obviously hinder the diffusion pathway of Li-ion. Figure 3.12(b) shows the MSD plot of Li-ion corresponding to Figure 3.12(a). Due to the restriction of this closed arrangement, the diffusion trajectory is similar to a circular ring, and the Li-ions cannot do the effective long-range diffusion in the La-rich layer of LLNO system. Similarly, 2D Li migration pathways are hindered by La ions in La-rich layer both in stripe arrangement and La-rich random arrangement. Therefore, a Li ion hopping into La-poor layer is necessary step to achieve long-distance migration except for the totally random arrangement structure. Although stripe arrangement obviously allows more distant 2D Li ion migration within La-rich layer, higher or comparable diffusivity of Li ion observed in closed arrangement (Figure 3.7(b)) is ascribed to the fact that the rate determining process is the Li ion hopping from La-rich to La-poor site. In other words, activation energies shown in Figure 3.7(b) for layered type structures mainly owe to the Li ion jump along c-axis to achieve long-range Li migration by avoiding La walls in the La-rich layer. As mentioned in Chapter 2, the appearance of modulated structure reduces the system energy significantly, and the whole structure is more stable. In Figure 3.11, we know that the jump along c-axis for La-rich/poor ordering is energetically unfavored due to the large site potential gap between two layers. So the hopping between the layers becomes the rate determining process. Nevertheless, two modulated structure models show lower activation energy and higher ionic conductivity

than the totally random model. Therefore, we infer that modulation also reduces transition state energy, make the long-range Li migration become easier.

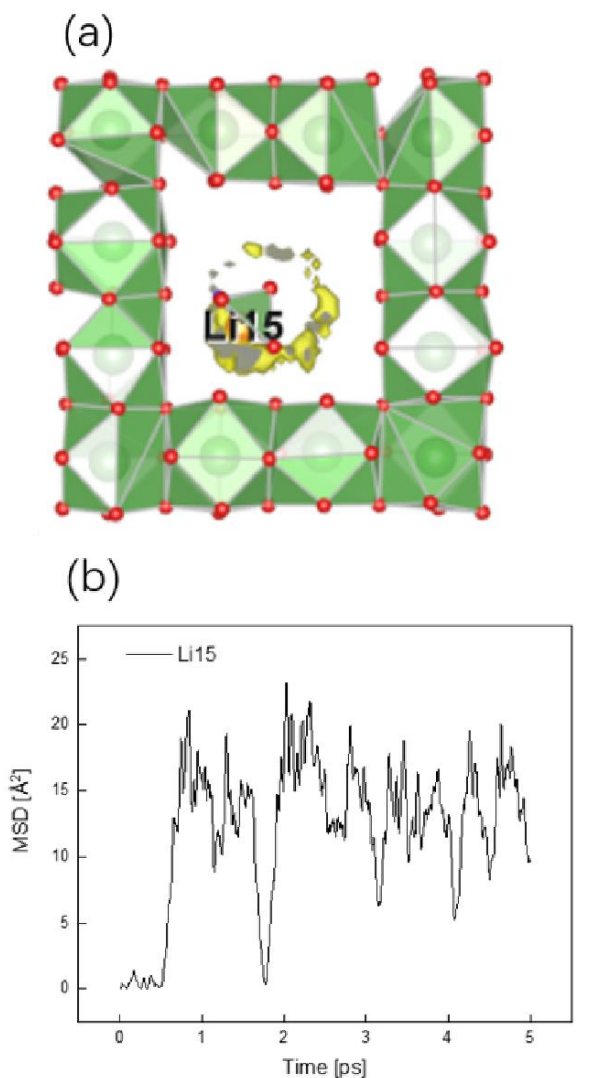


Fig 3.12 (a) The trajectory of Li-ion in the selected region of closed arrangement system of LLNO. (b) MSD plot of Li-ion in this selected region

3.4 Conclusion

In this work, the FF parameter sets for a perovskite-type material, LLNO, were determined via a metaheuristic algorithm based on AIMD outputs. The Li-ion conduction behaviors of modulated and disordered arrangements of La/Vac existing in LLNO were investigated via FFMD for the first time. The modulated arrangements in LLNO

significantly influenced the migration of Li ions. The existence of an alternating interlayer arrangement resulted in higher migration energy diffusing along the c-axis due to a large potential gap for Li ions between La-rich and La-poor layers. In addition, 2D Li migration pathways in the a-b plane were obstructed by La ions in the La-rich layer. Hopping along the c-axis was required for the long-range migration of Li and was, therefore, the rate-determining process. As a result, numerous intrinsic vacancies (mainly in the La-poor layer) became inaccessible, which is the main reason that the bulk ionic conductivity of LLNO is lower than that of LLTO. Interestingly, two of the modulated structures (closed and striped arrangements) displayed higher Li-ion conductivity than disordered structures by a factor of 10 at 800 K. In addition, the migration energy in the *ab* plane appeared to be much lower than along the c-axis. Consequently, a further improvement in the Li-ion conductivity can be achieved by eliminating La obstruction during long-distance migration.

Taking LLNO as an example, we performed molecular dynamics simulations by optimizing FFs parameters to reveal the influence between the microstructure of the material and the ion transition. Simultaneously, the research scheme of this work is also applicable to the study of other oxide and sulfide solid electrolyte materials. Provides research guidance for high-throughput material retrieval.

Reference

1. Inaguma, Y., Chen, L., Itoh, M. & Nakamura, T. Candidate compounds with perovskite structure for high lithium ionic conductivity. *Solid State Ionics* **70–71**, 196–202 (1994).
2. Mizumoto, K. & Hayashi, S. Conductivity relaxation in lithium ion conductors with the perovskite-type structure. *Solid State Ionics* **127**, 241–251 (2000).
3. Belous, A., Pashkova, E., Gavrilenko, O., V'yunov, O. & Kovalenko, L. Solid electrolytes based on lithium-containing lanthanum metaniobates and metatantalates with defect-perovskite structure. *Ionics* **9**, 21–27 (2003).
4. Carrillo, L. *et al.* Superstructure Determination of the Perovskite $\text{BLa}_{0.33}\text{NbO}_3$. *J. Mater. Sci.* **35**, 3047 (2000).
5. Gao, X. *et al.* Cation Ordering in A-Site-Deficient Li-Ion Conducting Perovskites $\text{La}_{(1-x)/3}\text{Li}_x\text{NbO}_3$. *J. Mater. Chem. A* **3**, 3351 (2015).
6. García-Martín, S. & Alario-Franco, M. Á. Modulated Structure of $\text{La}_{1/3-x}\text{Li}_x\text{NbO}_3$ $0 \leq x \leq 0.06$ Perovskite-Related Materials. *Journal of Solid State Chemistry* **148**, 93–99 (1999).
7. Fontaine, D. De. Cluster Approach to Order-Disorder Transformations in Alloys. in (eds. EHRENREICH, H. & TURNBULL, D.) **47**, 33–176 (Academic Press, 1994).
8. Ceder, G., Ven, A. Van der, Marianetti, C. & Morgan, D. First-principles alloy theory in oxides. *Modelling and Simulation in Materials Science and Engineering* **8**, 311–321 (2000).
9. Yang, Z. *et al.* Arrangement in $\text{La}_{1/3}\text{NbO}_3$ Obtained by First-Principles Density Functional Theory with Cluster Expansion and Monte Carlo Simulation. *Journal of Physical Chemistry C* **124**, 9746–9754 (2020).
10. Stramare, S., Thangadurai, V. & Weppner, W. Lithium Lanthanum Titanates: A Review. *Chemistry of Materials* **15**, 3974–3990 (2003).
11. Inaguma, Y., Katsumata, T., Itoh, M., Morii, Y. & Tsurui, T. Structural investigations of migration pathways in lithium ion-conducting $\text{La}_{2/3-x}\text{Li}_x\text{TiO}_3$ perovskites. *Solid State Ionics* **177**, 3037–3044 (2006).
12. Jalem, R. *et al.* Concerted migration mechanism in the Li ion dynamics of garnet-type $\text{Li}_7\text{La}_3\text{Zr}_2\text{O}_{12}$. *Chemistry of Materials* **25**, 425–430 (2013).
13. Ong, S. P. *et al.* Phase stability, electrochemical stability and ionic conductivity of the $\text{Li}_{10\pm 1}\text{MP}_2\text{X}_{12}$ (M = Ge, Si, Sn, Al or P, and X = O, S or Se) family of superionic conductors. *Energy and Environmental Science* **6**, 148–156 (2013).
14. Jalem, R., Aoyama, T., Nakayama, M. & Nogami, M. Multivariate method-assisted ab initio study of olivine-type LiMXO_4 (main group $\text{M}^{2+}\text{-X}^{5+}$ and $\text{M}^{3+}\text{-X}^{4+}$) compositions as potential solid electrolytes. *Chemistry of Materials* **24**, 1357–1364 (2012).
15. Jalem, R., Nakayama, M. & Kasuga, T. Lithium ion conduction in tavorite-type LiMXO_4F (M-X: AlP, MgS) candidate solid electrolyte materials. *Solid State Ionics* **262**, 589–592 (2014).
16. Van der Ven, A. Lithium Diffusion in Layered $\text{Li}_{[x]}\text{CoO}_{[2]}$. *Electrochemical and Solid-State Letters* **3**, 301 (1999).
17. Nakayama, M., Kimura, M., Jalem, R. & Kasuga, T. Efficient automatic screening for Li ion conductive inorganic oxides with bond valence pathway models and percolation algorithm. *Japanese Journal of Applied Physics* **55**, (2016).
18. Parfitt, D., Kordatos, A., Filippatos, P. P. & Chroneos, A. Diffusion in energy materials: Governing dynamics

-
- from atomistic modelling. *Applied Physics Reviews* **4**, 31305 (2017).
19. Noda, Y. *et al.* Computational and Experimental Investigation of the Electrochemical Stability and Li-Ion Conduction Mechanism of $\text{LiZr}_2(\text{PO}_4)_3$. *Chemistry of Materials* **29**, 8983–8991 (2017).
 20. Kresse, G. & Furthmüller, J. Efficient iterative schemes for ab initio total-energy calculations using a plane-wave basis set. *Physical Review B - Condensed Matter and Materials Physics* **54**, 11169–11186 (1996).
 21. Blöchl, P. E. Projector augmented-wave method. *Physical Review B* **50**, 17953–17979 (1994).
 22. Perdew, J. P., Burke, K. & Ernzerhof, M. Generalized gradient approximation made simple. *Physical Review Letters* **77**, 3865–3868 (1996).
 23. Perdew, J. P. *et al.* Restoring the density-gradient expansion for exchange in solids and surfaces. *Physical Review Letters* **100**, 1–4 (2008).
 24. Adams, S. & Rao, R. P. High power lithium ion battery materials by computational design. *Physica Status Solidi (A) Applications and Materials Science* **208**, 1746–1753 (2011).
 25. Stillinger, F. H. & Weber, T. A. Computer simulation of local order in condensed phases of silicon. *Physical Review B* **31**, 5262–5271 (1985).
 26. Jiang, J. W. Parametrization of Stillinger-Weber potential based on valence force field model: Application to single-layer MoS_2 and black phosphorus. *Nanotechnology* **26**, (2015).
 27. Yang, X.-S. & Deb, S. Engineering optimisation by cuckoo search. *International Journal of Mathematical Modelling and Numerical Optimisation* **1**, 330–343 (2010).
 28. Yang, X. S. & Deb, S. Cuckoo search via Lévy flights. *2009 World Congress on Nature and Biologically Inspired Computing, NABIC 2009 - Proceedings* 210–214 (2009). doi:10.1109/NABIC.2009.5393690
 29. Gandomi, A. H., Yang, X. S. & Alavi, A. H. Cuckoo search algorithm: A metaheuristic approach to solve structural optimization problems. *Engineering with Computers* **29**, 17–35 (2013).
 30. Grover, P. Regression Loss Functions All Machine Learners Should Know. (5AD).
 31. Kobayashi, R., Miyaji, Y., Nakano, K. & Nakayama, M. High-throughput production of force-fields for solid-state electrolyte materials. *APL Materials* **8**, (2020).
 32. Kobayashi, R. nap: A molecular dynamics package with parameter-optimization programs for classical and machine-learning potentials. *Journal of Open Source Software* **6**, 2768 (2021).
 33. Belous, A., Pashkova, E., Gavrilenko, O., V'yunov, O. & Kovalenko, L. Solid electrolytes based on lithium-containing lanthanum metaniobates. *Journal of the European Ceramic Society* **24**, 1301–1304 (2004).
 34. Nakayama, M., Imaki, K., Ikuta, H., Uchimoto, Y. & Wakihara, M. Electrochemical lithium insertion for perovskite oxides of $\text{Li}_y\text{La}_{(1-y)}\text{NbO}_3$ ($y = 0, 0.1, 0.25$). *Journal of Physical Chemistry B* **106**, 6437–6441 (2002).
 35. Auckett, J. E. *et al.* Combined experimental and computational study of oxide ion conduction dynamics in $\text{Sr}_2\text{Fe}_2\text{O}_5$ brownmillerite. *Chemistry of Materials* **25**, 3080–3087 (2013).

Chapter 4. An Efficient Experimental Search for Discovering Fast Li Ion Conductor from Perovskite-type $\text{Li}_x\text{La}_{(1-x)/3}\text{NbO}_3$ (LLNO) Solid State Electrolyte Using Bayesian Optimization

4.1 Introduction

From the perspective of the lattice structure, the transmission bottleneck, i.e., the size of the vacancy and the disorder of the A-site cation, significantly influences the ionic conductivity. Longer A-O bonds result in larger ion-transport bottlenecks and are more conducive to the migration of Li^+ in the A-site spaces. However, the radius of the A-site cation cannot be too large to avoid the counterproductive severe degeneration of the crystal structure.^{1,2} Considering the interactions between Li^+ and the framework ions, B-O distances and bond energies directly determine the binding strength of the A-site Li^+ to the O^{2-} in the framework; a B-site cation with a smaller radius beneficially strengthens B-O binding, while weakening the Li-O bond strength,^{2,3} thereby reducing the activation energy associated with Li^+ migration. To improve the Li-ion conductivity of a perovskite-type solid electrolyte through doping, any modifications are required to meet the following conditions: the size of the vacancy should match the Li^+ radius, the strengths of the bonds between Li^+ and the framework ions should be weak, and the ratio of vacancies to Li^+ should be moderate.

The structure of Lanthanum niobate $\text{La}_{1/3}\text{NbO}_3$ (LNO) is the same as LTO, they all have the ABO_3 perovskite-type structure. But LNO has a larger lattice volume and a higher intrinsic vacancies concentration,⁴ which makes it a potential solid electrolyte candidate with high ionic conductivity. However, the experimental observations are inconsistent with the hypothetical results, the highest observed bulk ionic conductivity of LLNO at room temperature is only $\sim 10^{-4} \text{ S cm}^{-1}$,⁴ which is almost an order of magnitude lower than that of LLTO. There are not many studies on improving the electrochemical performance of LLNO through doping modification compared to LLTO, so there is still room for improvement.⁵

Figure 2.1 shows the crystal structure of $\text{La}_{1/3}\text{NbO}_3$, which displays the

orthorhombic cell structure of LNO, the space group is Cmmm, and lattice parameters $a=b=3.91 \text{ \AA}$, $c=7.91 \text{ \AA}$,⁶ and the previous studies have shown that there is an alternate inter-layer structure composed of La atoms and vacancies in the A-site of LLNO.^{7,8}

In this chapter, we using doping modification to improve electrochemical performance of $\text{La}_{1/3}\text{NbO}_3$ with Li^+ and Sr^{2+} . The composition was optimized using an exhaustive experimental approach with Li_2CO_3 and Sr_2CO_3 as co-dopants to form $(\text{Li}_y\text{La}_{(1-y)/3})_{1-x}\text{Sr}_{0.5x}\text{NbO}_3$ ($0 \leq 0.5x \leq 0.15$, $0 \leq y \leq 0.3$). We synthesized and analyzed 64 samples with different compositions and characterized their physical and chemical properties through experiments. The first phase involved optimizing a promising solid electrolyte material and accumulating sufficient training data for the next step. To prove the advantages of combining information science methods with materials science, we introduced different exploration schemes to compare efficiency.

We used Bayesian optimization (BO)^{9, 10} as one of the approaches, with conventional random sampling as the other; the random sampling approach was used to approximate the trial-and-error method commonly used in experimental work. The BO-based exploration scheme has a higher exploration efficiency than the random sampling method, which shows that the introduction of this technology can improve the efficiency of screening fast lithium ion conductor materials.^{11,12} So far, the BO approach has been used several times with computational datasets. However, only a few studies use the BO method to determine the best material composition by analyzing existing experimental data.^{13,14} As an extension of this work, we also verified Bayesian optimization with multi-objective parameters. In this chapter, the reporting content is mainly based on the following aspects:

1. Characterization of the crystal phase and morphology of the prepared samples.
2. Analysis the ionic conductivity performance of the prepared samples.
3. Verification of informatics methods and evaluate the efficiency for screening the optimized composition.

4.2 Research methods

4.2.1 Using solid-state reaction to prepare the $(\text{Li}_y\text{La}_{(1-y)/3})_{1-x}\text{Sr}_{0.5x}\text{NbO}_3$ compounds

64 perovskite-type compounds with the formula $(\text{Li}_y\text{La}_{(1-y)/3})_{1-x}\text{Sr}_{0.5x}\text{NbO}_3$ and various doping concentrations ($0 \leq 0.5x \leq 0.15$, $0 \leq y \leq 0.3$) were prepared by the conventional solid-state reaction method.⁴ La_2O_3 (99.99% Wako Pure Chemical Industries, Ltd.), Li_2CO_3 (Kojundo Chemical Laboratory Co., Ltd.), Nb_2O_5 (Soekawa Chemical Co., Ltd.), and SrCO_3 (Soekawa Chemical Co., Ltd.) were used as the starting materials. Prior to mixing, La_2O_3 powder was decarboxylated by pre-heating at 1000 °C for 12 h, because Li_2CO_3 and SrCO_3 do not have moisture absorption, there is no need for pre-heating. All reagents were mixed in an agate mortar according to the stoichiometric ratio of the target product, with a small amount of ethanol added to aid grinding, and manually ground until well blended. The mixture of reagents was pressed into pellets at 120 MPa, then sintering in air at 700 °C for 2 h, and then at 1200 °C for 12 h. The prepared samples were then crushed, re-pelletized, and the sintering process was repeated.

4.2.2 XRD and SEM Characterization

The sintered samples were subjected to X-ray diffractometry (Rigaku Mini Flex 600, Japan) with Cu K α radiation to identify the crystalline phases and determine the lattice-parameters values.

Sample microstructures were characterized by field emission scanning electron microscopy (FESEM, JSM-7900F, JEOL, Japan).

4.2.3 Electrochemical analysis

The ionic conductivities of the prepared samples were measured using the AC impedance technique at various temperatures (30 °C, 60 °C, and 90 °C) in the 1 Hz to 1 MHz frequency range. The sintered samples were polished with emery paper (No. 2000) prior to testing to ensure that their tested surfaces were flat. Gold electrodes were sputtered onto both faces of each pellet sample. Ionic conductivity was calculated using equation 4-1, where L and S are the thickness and area of the sample, respectively. The activation energy, E_a , for Li-ion conduction was determined from the Arrhenius plot of Li-ion conductivity using equation 4-2, where A is the pre-exponential parameter. Impedance data were fitted by the ZView and Z-Assist software.

$$\sigma = \frac{L}{RS} \quad (4-1)$$

$$\sigma T = A \exp\left(\frac{-E_a}{RT}\right) \quad (4-2)$$

4.2.4 Measured the experimental data with the different informatics approaches

After generating the training dataset by experimentally examining all 64 samples, it was subjected to random searching and searching based on Bayesian optimization (BO). The criterion used to evaluate search-method efficiency was simply which method led to the sample with the best Li-ion conduction performance faster. Due to the randomness of the random search itself, and the uncertainty of the initial observation point in the BO search, the efficiencies of the two methods were comprehensively compared by performing 1000 independent searches. The average number of steps required to reach the best solution were used as the judging criterion. The Li-ion conductivities at various testing temperatures and the activation energy were selected as external variables ($\sigma_{30\text{ }^\circ\text{C}}$, $\sigma_{60\text{ }^\circ\text{C}}$, $\sigma_{90\text{ }^\circ\text{C}}$, and E_a), and compositions x and y in the $(\text{Li}_y\text{La}_{(1-y)/3})_{1-x}\text{Sr}_{0.5x}\text{NbO}_3$ formula were chosen as explanatory variables. The Gaussian process (GP) model is embedded in the current BO method,¹⁵ and the acquisition function adopts the expected improvement (EI) strategy. This part of calculation work, including 1000 trials, can be finished within server hours by using single core processor.¹⁶

4.3 Results and Discussion

4.3.1 Characterization of the crystal phase and morphology of the prepared samples.

4.3.1.1 Crystal phase of $(\text{Li}_y\text{La}_{(1-y)/3})_{1-x}\text{Sr}_{0.5x}\text{NbO}_3$

All the 64 sintered samples with different compositions were prepared via the solid-state reaction approach mentioned above. After step-by-step sintering, the preparation of the sample remains stable in an air environment at room temperature, and the samples are ground into powder to check their crystal characteristics; Figure 4.2 shows the powder XRD patterns of selected compositions. When the doping range between $0.06 \geq 0.5x \geq 0$ of Sr^{2+} -doped samples and the $0.25 \geq y \geq 0$ of Li^+ -doped samples, the single-phase materials of $(\text{Li}_y\text{La}_{(1-y)/3})_{1-x}\text{Sr}_{0.5x}\text{NbO}_3$ solid solutions were verified. The characteristic peaks of $\text{La}_{0.3}\text{Li}_{0.1}\text{NbO}_3$ with a perovskite structure are shown in the figure. When $0.5x \geq 0.08$ or $y \geq 0.25$, the impurity phases of SrNb_2O_6 , $\beta\text{-Sr}_3\text{La}_2\text{Nb}_{12}\text{O}_{36}$ were observed from the XRD patterns, as shown in Figure 4.2 the additional diffraction peaks. Within this doping range, all Sr^{2+} -doped samples have the same crystal symmetry as the corresponding singly Li^+ -doped perovskite system.

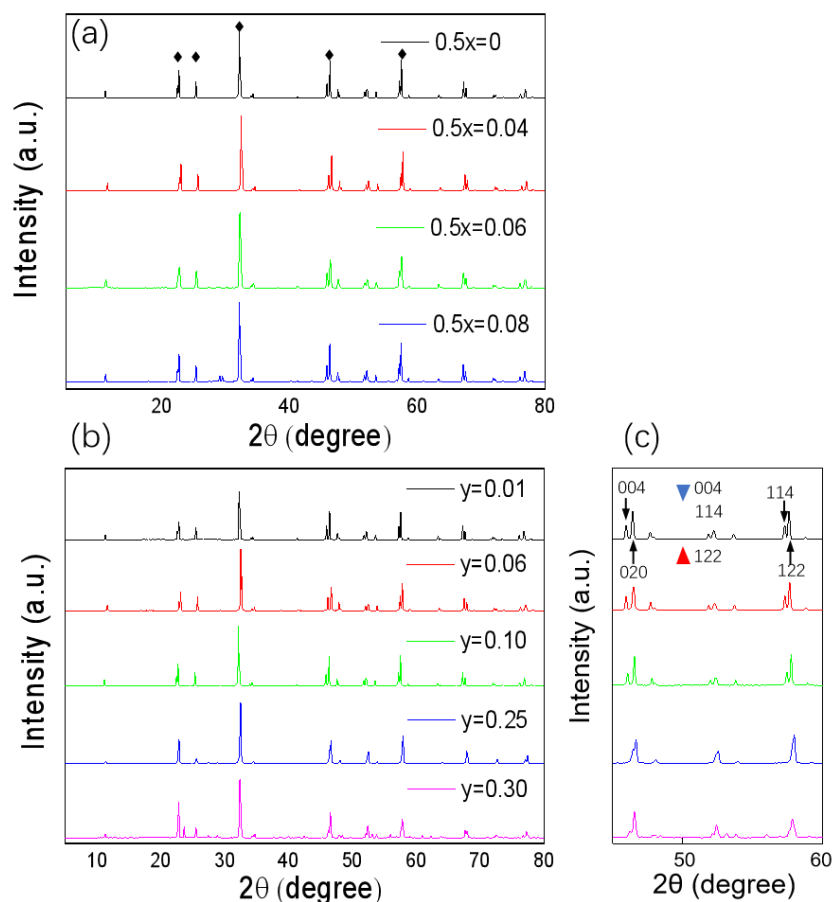


Fig. 4.2 XRD pattern of sintered samples showing the composition-dependence of the crystalline structure. (a) $(\text{Li}_{0.1}\text{La}_{0.3})_{1-x}\text{Sr}_{0.5x}\text{NbO}_3$. (b) $(\text{Li}_y\text{La}_{(1-y)/3})_1\text{Sr}_0\text{NbO}_3$. (c) Enlargement of (b) highlighting peak splitting.

In Figure 4.2(c), in addition to the reflection of the typical perovskite structure, line splitting can also be observed. As shown in Figure 4.2(b), the line splitting decreases with the increased of Li^+ dopant.¹⁷ The observed decrease in line splitting is due to a decline in the 004/020 and 114/122 peak ratios, which indicates a changed in the crystal symmetry of the perovskite system. The line splitting increases again at $y = 0.3$, which may be due to the interference of the diffraction peaks of the impurity phase. When Li^+ progressively replaces La^{3+} , a small amount of orthogonal deformation occurs in the lattice. The symmetry of the structure changes from the original orthorhombic $((\text{Li}_{0.01}\text{La}_{0.33})_{1-2x}\text{Sr}_x\text{NbO}_3)$ to tetragonal $((\text{Li}_{0.1}\text{La}_{0.3})_{1-2x}\text{Sr}_x\text{NbO}_3)$ and transforms into pseudo-cubic $((\text{Li}_{0.25}\text{La}_{0.25})_{1-2x}\text{Sr}_x\text{NbO}_3)$ eventually.¹⁸

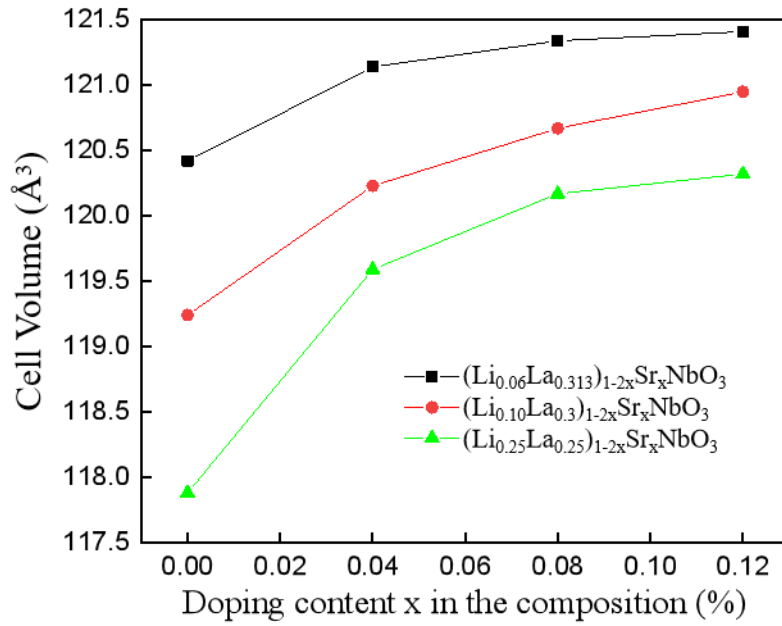


Fig.4.3 Cell volumes as function of Sr²⁺ content in the perovskite system.

The change trend of unit cell volume with Sr²⁺ doping content in the parent perovskite system is shown in Figure 4.3. The figure shows that with the increase of Sr²⁺ content in the system, in the three symmetric structures of LLNO, the unit cells volume all have increased in varying degrees. The source of the increase is that Sr²⁺ has a larger ionic radius (1.44 Å) than La³⁺ (1.36 Å). This change in lattice structure is considered to benefit Li-ion conduction² due to the expansion of the bottleneck area, as observed experimentally (see below). The XRD patterns with Rietveld refinements of some selected compositions also confirmed the increase of cell volume due to Sr²⁺ doping, the results as shown in Table 4.1 and 4.2.

Table 4.1. Structural Parameters for (Li_{0.1}La_{0.3})Sr₀NbO₃ in P4/mmm.

Reliability parameters: Rwp=12.79%, Rp=9.25%, S=1.48.

Lattice parameter: $a=b=3.91170(3)\text{Å}$, $c=7.89398(9)\text{Å}$ (Tetragonal).

Label / Ion	site	<i>g</i>	<i>x</i>	<i>y</i>	<i>z</i>	B / Å
La1/La ³⁺	1 <i>a</i>	0.582(2)	0	0	0	0.32(4)
La2/La ³⁺	1 <i>b</i>	0.018(2)	0	0	0.5	0.32(4)
Nb1/Nb ⁵⁺	2 <i>h</i>	1.0	0.5	0.5	0.2604(2)	0.74(3)
O1/O ⁻	4 <i>i</i>	1.0	0	0.5	0.2341(10)	1.74(14)

O2/O ⁻	1c	1.0	0.5	0.5	0	1.74(14)
O3/O ⁻	1d	1.0	0.5	0.5	0.5	1.74(14)

Table 4.2. Structural Parameters for (Li_{0.09}La_{0.27}) Sr_{0.05}NbO₃ in P4/mmm.

Reliability parameters: Rwp=15.20%, Rp=11.47%, S=1.52.

Lattice parameter: $a=b=3.91607(14)\text{\AA}$, $c=7.90441(31)\text{\AA}$ (Tetragonal).

Label / Ion	site	<i>g</i>	<i>x</i>	<i>y</i>	<i>z</i>	B / Å
La1/La ³⁺	1a	0.54(-)	0	0	0	0.18(5)
Sr2/Sr ²⁺	1b	0.10(-)	0	0	0.5	0.18(5)
Nb1/Nb ⁵⁺	2h	1.0	0.5	0.5	0.2617(2)	0.79(4)
O1/O ⁻	4i	1.0	0	0.5	0.2364(12)	1.70(17)
O2/O ⁻	1c	1.0	0.5	0.5	0	1.70(17)
O3/O ⁻	1d	1.0	0.5	0.5	0.5	1.70(17)

4.3.1.2 Relative density and Scanning electron microscopy

Figure 4.4 shows the changing trend between the sintered samples' relative density (the ratio of the bulk density of the sintered pellet to the theoretical density of the corresponding formula) and their compositions. The relative density is one of the important indexes to measure the sintering performance. A high degree of sintering is essential not only for mechanical stability but also for the total resistance of the bulk sample. In solid electrolytes, the grain boundary resistance usually determines the total resistance of the material,¹⁹ reducing the resistance of the grain boundary is a reasonable method to improve the bulk ionic conductivity. The higher relative density of the sintered sample indicates that the inside of the material is denser and the grain boundary is constricted, so the grain boundary resistance is reduced. The relative density of the sample increased from about 50% to 90% through Li⁺ and Sr²⁺ doping. It is clear to see that when the doping content of Li⁺ is larger 10%, the relative density will greater than 80%, Li⁺ plays a major role.

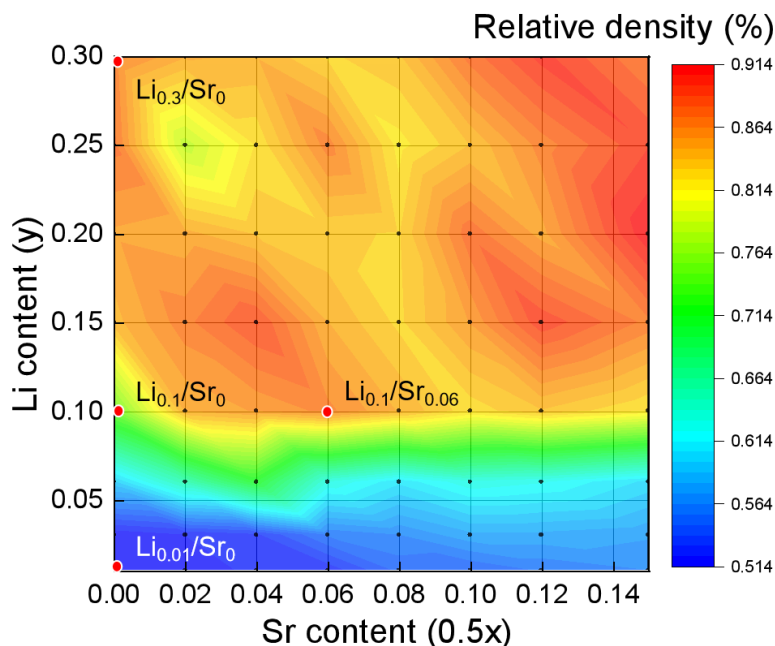


Fig. 4.4 Heatmap of relative density as a function of composition of the sintered $(\text{Li}_y\text{La}_{(1-y)/3})_{1-x}\text{Sr}_{0.5x}\text{NbO}_3$ sample. The composition shown by the red dot corresponds to the composition shown in Figure 4.5

The SEM images of selected samples with different compositions ($\text{Li}_{0.01}/\text{Sr}_0$, $\text{Li}_{0.1}/\text{Sr}_0$, $\text{Li}_{0.3}/\text{Sr}_0$, and $\text{Li}_{0.1}/\text{Sr}_{0.06}$) corresponding to the pointed data in Figure 4.4 were shown in Figure 4.5. The sample with low Li content shows distinct grain boundaries (Figure 4.5(a)). With the increase of Li^+ content, the surface morphology of the sample changed from a porous structure to a dense structure, and a small amount of cavitation appeared at the same time. Sr^{2+} doping also shows a positive effect on the sintering performance of the samples, which can be attributed to two aspects. Firstly, the setting sintering temperature was higher than the melting point of Li_2CO_3 which was selected as the Li^+ source. Therefore, during the sintering process, a small amount of liquid phase may be generated, which promotes particle rearrangement, mass-transfer processes, and reaction with other metal compounds.²⁰ Secondly, a solid solution will be formed when the LNO is doped by Li^+ and Sr^{2+} , the doping ions will enter LNO lattice, this will cause the lattice distortion and reduce the activation energy and accelerates diffusion.^{21,22} When forming the vacant or interstitial solid solutions, this effect is significant.

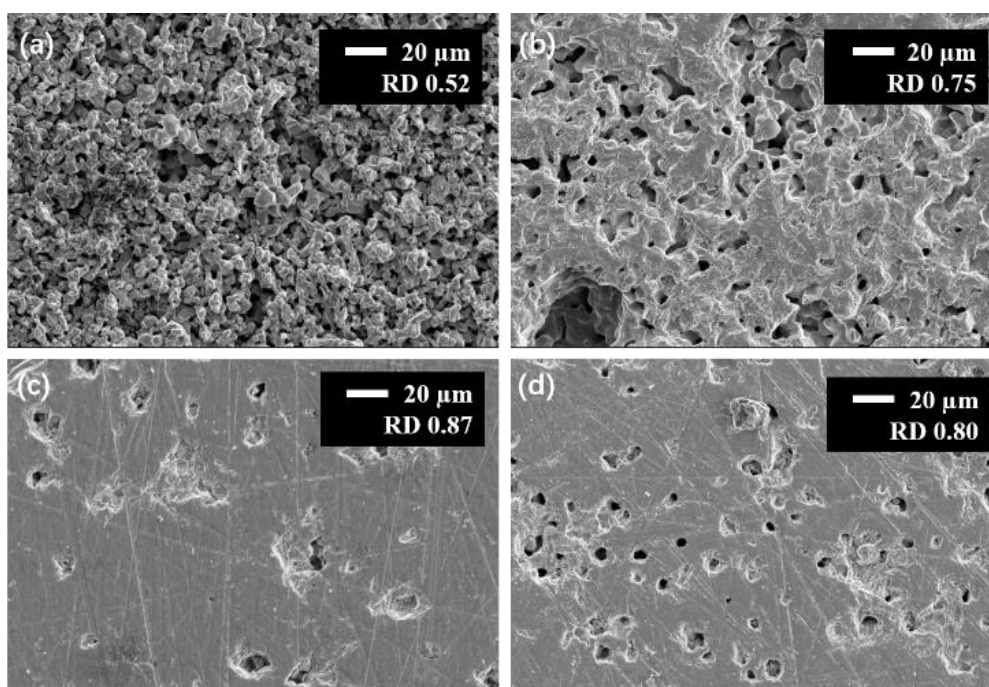


Fig.4.5 SEM images of the surfaces of sintered samples with selected compositions: (a) $\text{Li}_{0.01}/\text{Sr}_0$, (b) $\text{Li}_{0.1}/\text{Sr}_0$, (c) $\text{Li}_{0.3}/\text{Sr}_0$, and (d) $\text{Li}_{0.1}/\text{Sr}_{0.06}$.

4.3.2 Electrochemical performance of $(\text{Li}_y\text{La}_{(1-y)/3})_{1-x}\text{Sr}_{0.5x}\text{NbO}_3$

4.3.2.1 AC impedance analysis

Figure 4.6(a) shows the complex impedance spectrum (Nyquist plot) of $(\text{Li}_y\text{La}_{(1-y)/3})_{1-x}\text{Sr}_{0.5x}\text{NbO}_3$ which prepared as mentioned above, the doping sample $\text{Li}_{0.06}/\text{Sr}_{0.02}$ is selected as an example. Figure 4.7 shows the Nyquist plots of the other compositions for comparison purposes. A slightly distorted semicircle in the 1 MHz to 200 Hz range is observed in the high-frequency region and can be fitted to two semicircles attributable to bulk resistance (in the high-frequency region indicated by the red line in Figure 4.6(a)) and grain-boundary resistance (in the low-frequency region indicated by the blue line). The spike that appeared in the low-frequency region (below 200 Hz) corresponds to the ion-blocking capacitance, the source of this is originated by the interface between the electrolyte and the Au electrode. Figure 4.6(a) displays the equivalent circuit which determined by impedance analysis, the ZView and Z-Assist programs were used to drive this work. The total resistance of the sample (R_t) is the total contribution of the bulk resistance (R_b) and the grain-boundary resistance (R_{gb}). Since the frequency response characteristics of solid-state dielectric double-layer capacitors are different from those of pure capacitors, a dispersion phenomenon occurs.^{23,24} To cover this influence, when

simulating the equivalent circuit, the constant phase element (CPE) is used to replace the commonly used pure capacitor. Through this equivalent circuit, the impedance diagram obtained for the sample we tested can be fitted well, thereby refining the influence of the volume and grain boundaries on the total resistance. Except for samples with very low or very high doping content, the chi-square value of most samples is about 10^{-3} – 10^{-4} , showing goodness of fit. Figure 4.6(b) shows the Arrhenius plot of Li-ion conduction. The coefficient of determination (R^2) is an important indicator for evaluating the quality of the linear regression function. In this work, in order to more accurately evaluate the activation energy of Li-ion conduction, only well-fitted Arrhenius plots with R^2 values greater than 0.98 were used to calculate this data.

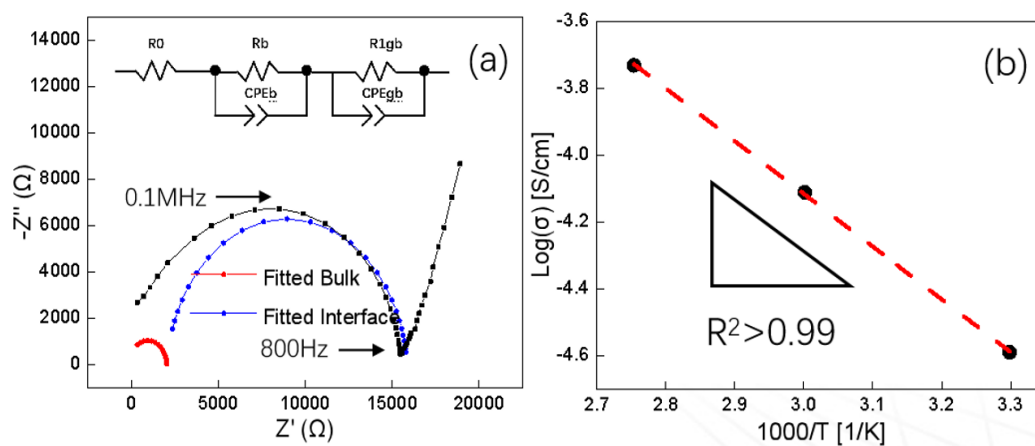


Fig. 4.6 (a) Typical complex impedance spectrum (Nyquist plot) for $\text{Li}_{0.06}/\text{Sr}_{0.02}$ at 30°C prepared by the conventional solid-state reaction method, and the equivalent circuit. (b) Arrhenius plot for Li-ion conductivity.

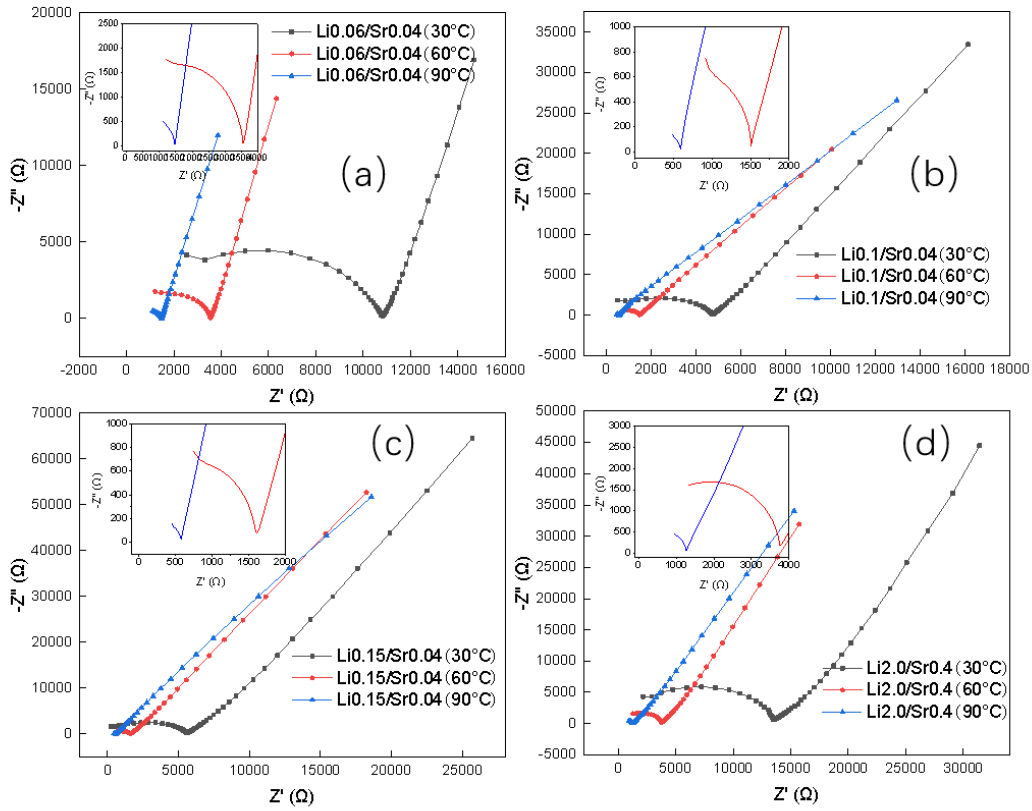


Fig.4.7 Nyquist plot for Li_{0.06}/Sr_{0.04}(a), Li_{0.1}/Sr_{0.04}(b), Li_{0.15}/Sr_{0.04}(c), Li_{2.0}/Sr_{0.04}(d), at 30°C, 60°C, 90°C.

4.3.2.2 Li-ion conductivity and activation energy of $(\text{Li}_y\text{La}_{(1-y)/3})_{1-x}\text{Sr}_{0.5x}\text{NbO}_3$

Heatmaps of Li-ion conductivity and activation energy as shown in Figure 4.8, this figure shows that the composition of the test sample $(\text{Li}_y\text{La}_{(1-y)/3})_{1-x}\text{Sr}_{0.5x}\text{NbO}_3$ significantly affects its ion conduction. Maximum Li-ion conductivities are observed at appropriate doping concentrations ($0.02 < 0.5x < 0.08$, $0.05 < y < 0.15$), which are referred to as “hot zones.” Among the test samples, the highest Li-ion conductivity at 30 °C (8.002×10^{-5} s/cm) was observed for the $(\text{Li}_{0.1}\text{La}_{0.3})_{0.92}\text{Sr}_{0.04}\text{NbO}_3$ composition, as listed in Table 4.3:

Table 4.3. Highest conductivities and activation energies of single-doped and co-doped compositions.

Composition	Li-ion conductivity at 30 °C (S/cm)	Activation energy (eV)
Li _{0.01} /Sr _{0.04}	2.46×10^{-7}	----

$\text{Li}_{0.15}/\text{Sr}_0$	2.57×10^{-5}	0.36
$\text{Li}_{0.1}/\text{Sr}_{0.04}$	8.00×10^{-5}	0.31

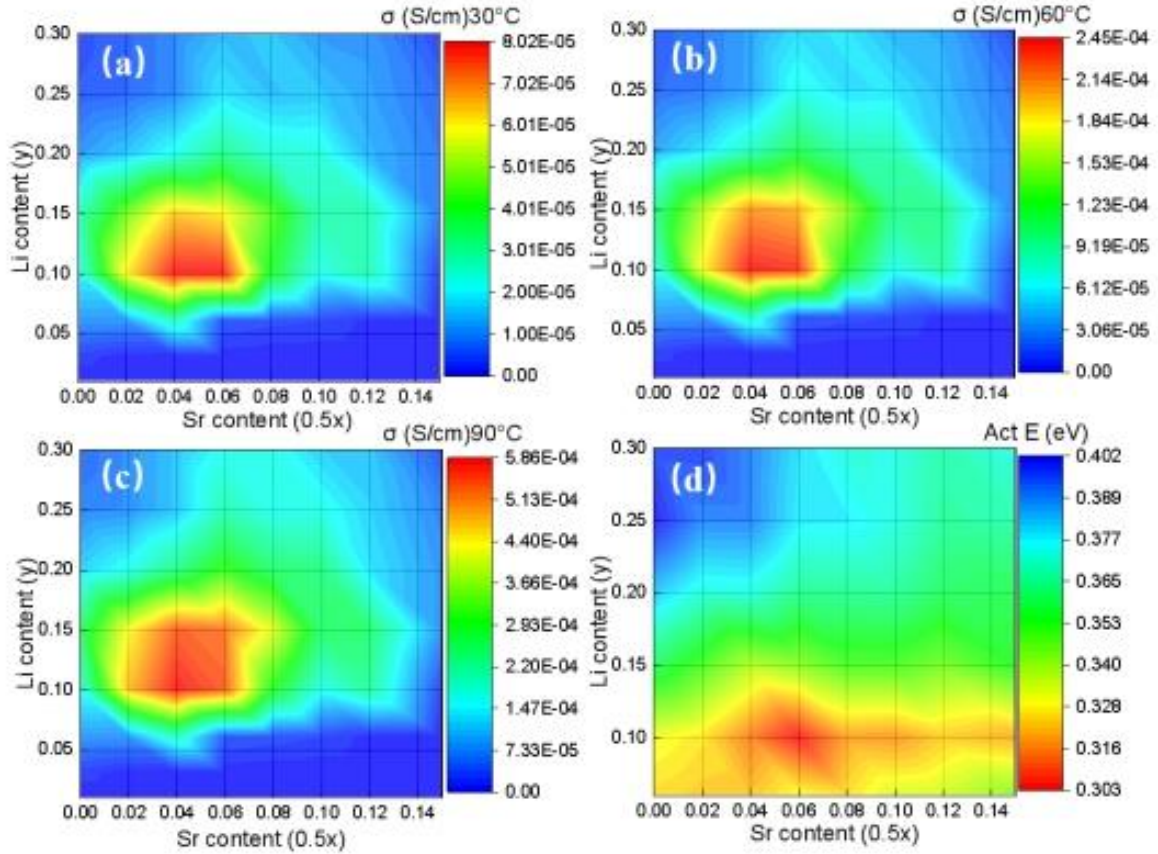


Fig. 4.8. Heat map of $(\text{Li}_y\text{La}_{(1-y)/3})_{1-x}\text{Sr}_{0.5x}\text{NbO}_3$ ionic conductivities at (a) 30 °C, (b) 60 °C, and (c) 90 °C, and (d) calculated activation energies for Li-ion conduction.

The highest conductivity of optimal composition is almost 3.5 times higher than of the single Li^+ doping composition $\text{Li}_{0.15}/\text{Sr}_0$ and about two orders of magnitude higher than that of single Sr^{2+} doping sample $\text{Li}_{0.01}/\text{Sr}_{0.04}$. The former demonstrates the highest ionic conductivity among Li^+ single-doped samples, while the latter shows the best performance among samples affected by single Sr^{2+} doping at the minimum Li^+ -doping concentration; the 1% of Li^+ doping concentration was set as the lowest exploration boundary in one dimension. It is clear to see that the heat map of activation energy has a similar hot zone to the ionic conductivity heat map ($0.02 < 0.5x < 0.08$, $y \approx 0.1$). From the relationship between the doping concentration and the electrochemical performance, it can be seen that the doping of Li-ions plays a major role in the improvement of the ionic conductivity of the LNO perovskite material. Li^+ replaces the original La^{3+} in the A-sites

of the structure because their ionic radii are quite different.

La^{3+} with a larger ion radius helps to stabilize the structure of the perovskite material, while Li-ions with a smaller ion radius diffuse through the pipe around the La^{3+} ion; through doping modification, the concentration of oxygen ion vacancies in the original perovskite structure will also increase, which improves the ionic conductivity. However, this positive effect of doping modification only works at a certain doping range. When the doping content is excessive, Li-ions will occupy all of the vacancy sites in the La-rich layer (A1) and also partially occupy the vacancies in the La-poor layer (A2).

The diffusion behaviors of LLNO is different from the LLTO, the conduction of Li-ion mainly occurs in the A1 layer at room temperature,¹⁸ based on the diffusion trajectory (The more detail can check the chapter.3), LLNO is close to a two-dimensional conductive material at low temperature. Excessive Li-ion doping not only blocks the conduction pathway composed of NbO_6 octahedra, but also severely deforms the crystal lattice and destroys the original La/Vac long-range modulated structure, as seen in our previous research.⁸ Although the achievement of single Sr^{2+} doping modification is not as significant as single Li^+ doping modification, the co-doping of Li^+ and Sr^{2+} shows better performance, indeed. Replacing La^{3+} with Sr^{2+} can lead to massive vacancies that increase the size of the Li-ion migration pathway and reduce the energy barrier for hopping. However, this replacement occurs at the same site in the structure, which will reduce the concentration of Li^+ as the consequence.

This trend is also verified by Figure 4.9, the ionic conductivity does not blindly increase with the increase of the unit cell volume. Multi-element doping modifications require material compositions to be comprehensively explored when the doping elements affect each other. Doping modification usually depends on the positive influence of the doping element on specific aspects of the system. This influence is cumulative within a certain range. Therefore, increasing the exploration of favorable system variables will greatly increase the experimental workload, but may also improve performance. Obviously, the efficiency of screening unknown components needs to be improved.

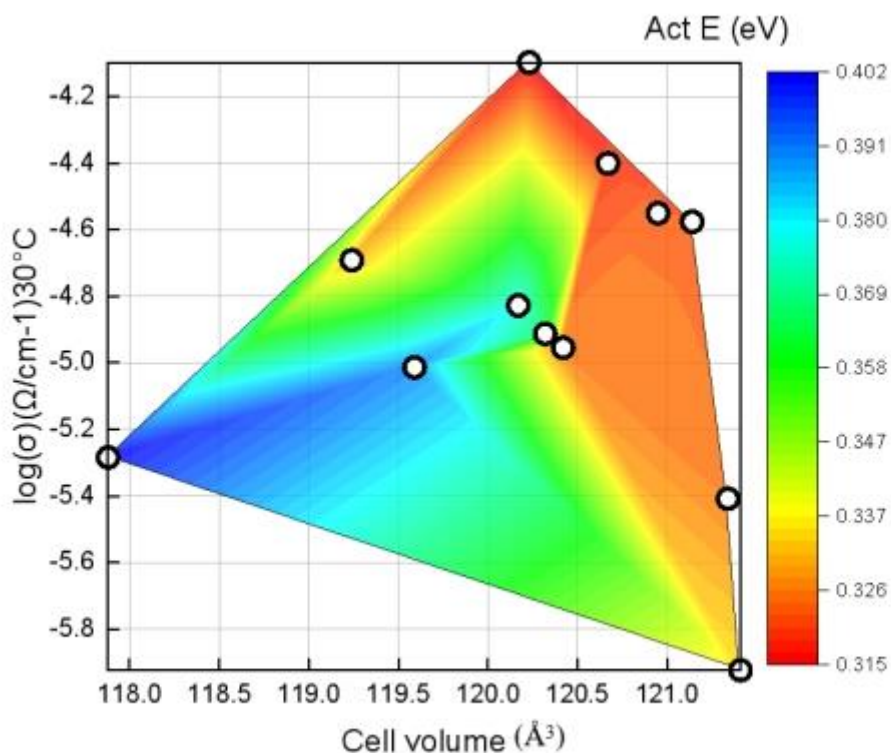


Fig.4.9 Heat map of cell volume, ionic conductivity and activation energies.

4.3.3 The use of Bayesian optimization to accelerate material screening

4.3.3.1 How Bayesian optimization approach wo predict the next observation point

In order to verify that Bayesian optimization (BO) can effectively improve the retrieval efficiency of target variables in experimental exploration, the above experimental data sets were compared based on different retrieval methods (Bayesian optimization, random sampling method). One thousand independent searches were performed using both methodologies, which revealed that BO searching provides a significantly better outcome than random searching. For the convenience of readers, we briefly introduce the principle of Bayesian optimization and why it has better performance than conventional search methods.

The BO approach is widely used to optimize hyperparameters in the machine learning area;²⁵ this method uses the prior distribution of each sampling point to learn the shape of the objective function, with the distribution updated in subsequent iterations. The testing algorithm provides a possible point by posterior distribution. Based on this idea, the BO search provides an efficient sampling approach and accelerates the rate at

which the optimized composition is arrived at. The sequential model-based optimization (SMBO) is shown in Figure 4.10

Algorithm Sequential Model-Based Optimization

```

Input:  $f, X, S, M$ 
 $D \leftarrow \text{INITSAMPLES}(f, X)$ 
for  $i \leftarrow |D|$  to  $T$  do
     $P(y | x, D) \leftarrow \text{FITMODEL}(M, D)$ 
     $x_i \leftarrow \arg \max_{x \in X} S(x, P(y | x, D))$ 
     $y_i \leftarrow f(x_i)$      Expensive step
     $D \leftarrow D \cup (x_i, y_i)$ 
end for

```

Fig. 4.10. Pseudocode of the Bayesian optimization algorithm

The input parameters include f , the “black box”, which is the objective function in our work, with compositions x and y in $(\text{Li}_y\text{La}_{(1-y)/3})_{1-x}\text{Sr}_{0.5x}\text{NbO}_3$ set as the explanatory variables (the descriptors in the GP process model), and the Li-ion conduction performance parameters set as the objective variables. X is the search space of the descriptors and D represents a data set consisting of several pairs of data, with each array represented as (x_i, y_i) . S is the acquisition function, which is used to determine x , the possible parameter that maximizes the global result, while M is the model derived by fitting the data obtained using GP regression in this part of work.

At present, the commonly used optimization algorithms inevitably have the shortcoming of falling into the local optimal solution. In order to deal with this problem, the BO method introduces a acquisition function to balance the ratio of exploration and exploitation. Exploration tends to sample in areas that have not yet been sampled, while exploitation is based on the posterior distribution, sampling in the area where the global optimal solution is most likely to be found. The reasonable next sampling point (x) should have a relatively large mean (exploitation) and also a high variance (exploration). The following are the three standard acquisition functions: the upper confidence bound (UCB), the probability of improvement (PI), and the expected improvement (EI).²⁶ Let $\mu(x)$ and $\sigma(x)$ be the predictive mean and standard deviation of the GP regression model.

We used the EI strategy to determine the next evaluated composition, which is defined as follows (equation 4-4):

$$EI(x)=\begin{cases} (\mu(x) - f(x^+))\Phi(z) + \sigma(x) \phi(z) & \sigma(x) > 0 \\ \text{Max}(0, \mu(x) - f(x^+)) & \sigma(x) = 0 \end{cases} \quad (4-4)$$

where $z(\cdot)$ is given by equation (4), $\phi(\cdot)$ is the probability density function (PDF), $\Phi(\cdot)$ is the normal cumulative distribution function (CDF), and x^+ is the best point among past sampled points.

$$z = \frac{\mu(x) - f(x^+)}{\sigma(x)} \quad (4-5)$$

4.3.3.2 Comparing the search efficiencies of the random search (black symbols) and Bayesian optimization

Figure 4.11 shows the statistics of 1000 trials, it is clear to see that the BO search only requires 20 observation steps to find the optimal solution from the data set, and the success rate is greater than 90%. In contrast, random search needs to retrieve the entire data set to ensure that the optimal solution is found. The BO method reduces the number of observation steps required by two-thirds, and the efficiency is significantly improved. No matter we explore the global maximum solution, or the global minimum solution in the target variable set, BO search shows the superiority equally. Figure 4.10(d) shows that, on average, after 16 observation steps, the probability of reaching the optimal solution is higher than 99%. The upper part of all four graphic panels clearly shows that after several observation steps, the screening efficiency of the BO method is significantly improved. This result is in line with our expectations. The superiority of the BO method comes from two aspects. On the one hand, the hyperparameters are updated as the sampling process proceeds, and subsequent hyperparameter sets are generated after the initial exploration step, which helps to speed up the screening efficiency of the search space. On the other hand, the acquisition function we adopted is based on the EI strategy, which maximizes the expectation of the modified objective function and also considers the region with large variance, which effectively avoids falling into the local optimal solution.

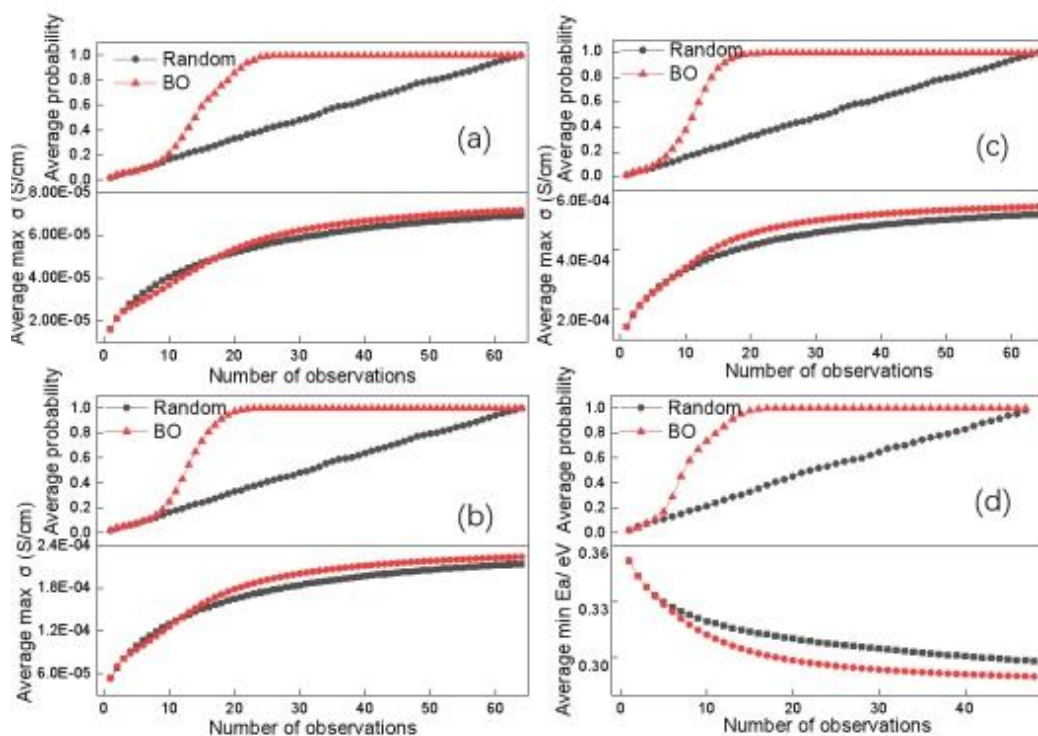


Fig. 4.11 Comparing the search efficiencies of the random search (black symbols) and Bayesian optimization (red symbols) methods using the Li-ion conductivities at (a) 30 °C, (b) 60 °C, and (c) 90 °C, and (d) the activation energy as objective variables. The upper and lower sections in each panel show the average probability and the cumulative average maximum as functions of the current observation number over 1000 optimization trials, respectively.

4.3.3.3 Bayesian optimization with multi-objective parameters

From the above the results, we already confirmed that to deal with the problem of single objective function prediction, the BO search method can improve the screening efficiency significantly. We extended this method to the multi-parameter optimization of mechanical and ion conductivity properties. For the optimization problem of multi-objective parameters, due to the potential trade-off relationship, the distribution of the objective parameters may not lead to the only optimal point (Figure 4.12). When the absolute optimal solution cannot be obtained, it is necessary to introduce a compromise concept, that is, the effective solution is also called (Pareto optimal solution), this concept means that it is impossible to improve another variable without harming other variables. Just as the Pareto optimal solution represented by the red dot in Figure 4.12, it is clear that neither mechanical properties nor ionic conductivity can be self-improved without

sacrificing the interests of the other party. To quantify the quality of a set of solutions for the prediction of a multi-objective problem, here, we used the hypervolume as the evaluation function. The hypervolume index is composed of the target variable individual in the solution set and the reference point in the search space, which corresponds to the yellow shaded area in Figure 4.12. If one solution set S is better than another solution set S' , then S will have a greater hypervolume index than S' . The extension of EI²⁷ was used as the acquisition function to evaluate the expected increase in the Pareto hypervolume.

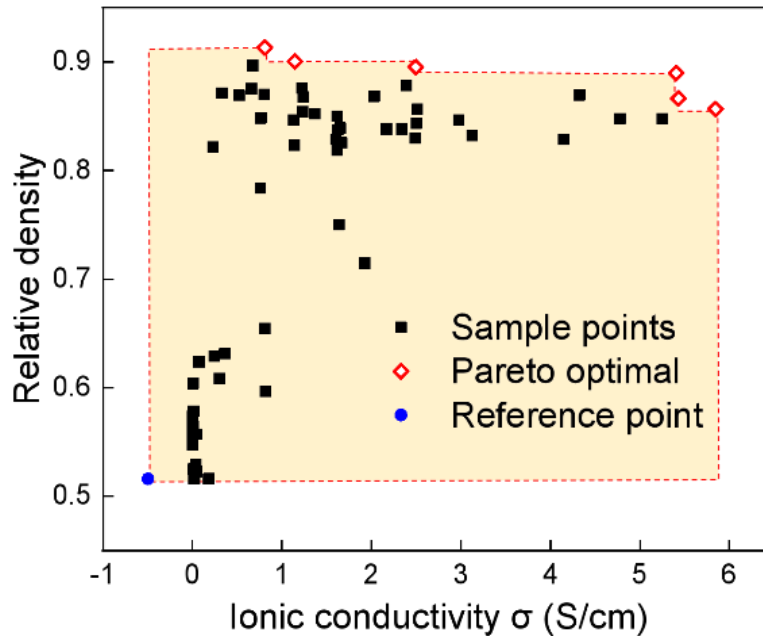


Fig. 4.12 Objective parameter distributions composed of measured values of ionic conductivity at 90 °C and relative densities. The Pareto optimal solution set contains six samples with different compositions, as represented by the red dots. The Pareto hypervolume, which is a multi-objective evaluation index, is defined by the yellow shaded region. The reference point is defined as the minimum value of each objective parameter ξ in the solution set, where $\xi = 10^{-4}$

The optimization process is displayed in Figure 4.13, as a function of observation number, this figure clearly shows the efficiency difference between these two methods. The ratio of the hypervolume of the currently observed solution set to that of the Pareto optimal solution set was defined as the relative hypervolume,²⁶ which was used to

evaluated the optimization process. By applying the multi-objective Bayesian optimization (MOBO) method, after about 20 observation steps, the relative hypervolume is greater than 0.99, the searching efficient is improved almost 100%. Obviously, by using a suitable evaluation function, the efficiency of Bayesian optimization can also be improved when dealing with multiple target variables. This method is suitable for experimental researchers to quickly make judgments when faced with the optimization of multi-objective parameters in the material development process, thereby reducing research costs.

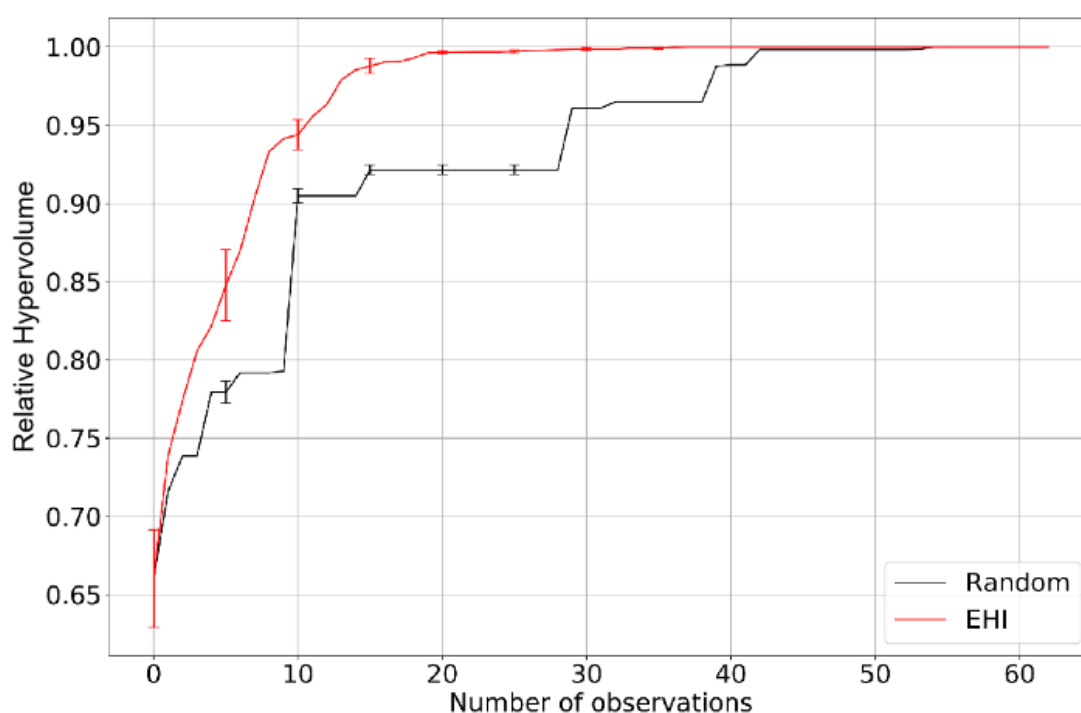


Fig. 4.13 Comparing the performance of the multi-objective Bayesian optimization process using the expected hypervolume improvement (EHI) (red line) and the random search method (black line). The optimized parameters are ionic conductivity at 30 °C and relative density.

4.4 Conclusion on Chapter 4

Based on the typical $\text{La}_{1/3}\text{NbO}_3$ perovskite-type material, we synthesized $(\text{Li}_y\text{La}_{(1-y)/3})_{1-x}\text{Sr}_{0.5x}\text{NbO}_3$ ($0 \leq 0.5x \leq 0.15$, $0 \leq y \leq 0.25$) compositions by co-doping with Li^+ and Sr^{2+} . We optimized the co-doping composition through comprehensive structural

characterization and by analyzing the electrochemical performance of the prepared samples. The highest ionic conductivity at room temperature (8.002×10^{-5} S/cm), which includes contributions from bulk and grain-boundary conduction, was observed for the $(\text{Li}_{0.1}\text{La}_{0.3})_{0.92}\text{Sr}_{0.04}\text{NbO}_3$ composition. The doped ions improve the total ionic conductivity differently. Due to differences in ionic radii, Li^+ diffuses through pipes around La^{3+} ions as the major ion-conducting carrier. In contrast, the larger Sr^{2+} ions form larger vacancies, which increase the size of the Li-ion migration pathway and reduce the energy barrier for hopping. In addition, the sintered morphologies of the obtained samples reveal that Li_2CO_3 significantly increases the relative density of the sample, which helps to reduce grain-boundary resistance, with Sr^{2+} also exhibiting a positive effect. Due to numerous influencing factors that are difficult to quantify, the compositional dependence of the Li-ion conductivity is rather complicated. Conventional experimental compositional optimization approaches rely on a large amount of repetitive work that is based on personal experience and intuition.

To improve material-screening efficiency we demonstrated the feasibility of combining Bayesian optimization, which is used in informatics, to materials science. Random searching and the BO-based search approach were both used to predict the optimal solution in a 64-sample dataset. The BO method was found to require an average of 20 observation steps to locate the optimal solution in the dataset, with a success rate in excess of 99%. Compared to the random-search method, the BO approach shortens the number of required steps by two-thirds and dramatically improves efficiency. In addition, for multi-objective optimization, we applied the MOBO approach to Pareto frontier searching using the experimental dataset, which also improved efficiency. In summary, this part of work highlights the feasibility of applying BO and related techniques to optimizing the compositions of complete compounds in materials science.

All the measured experimental data including bulk/relative densities, ionic conductivities, activation energies, cell volumes are tabulated in the Table 4.4

Table 4.4 The real density, relative density and ionic conductivity at 30 °C for all 64 sintering samples, the activation energy for 48 samples, and Cell volume for 12 selected samples.

label	Li (y)	Sr (0.5x)	bulk density(g/cm3)	relative density (%)	Ionic conductivity	Activation energy (eV)	Cell volume
-------	--------	-----------	------------------------	----------------------	-----------------------	---------------------------	----------------

					$\sigma(\Omega/\text{cm}^{-1})$ 30°C		
						(Å ³)	
1.1	0.010	0.000	2.615	0.516	2.54E-07		
2.1	0.010	0.020	2.615	0.516	1.93E-07		
3.1	0.010	0.040	2.660	0.525	2.46E-07		
4.1	0.010	0.060	2.659	0.525	1.92E-07		
5.1	0.010	0.080	2.786	0.550	1.19E-07		
6.1	0.010	0.100	2.774	0.547	1.08E-07		
7.1	0.010	0.120	2.822	0.557	7.18E-08		
8.1	0.010	0.150	2.857	0.564	3.50E-08		
1.2	0.030	0.000	2.614	0.516	2.45E-06		
2.2	0.030	0.020	2.648	0.523	7.60E-07		
3.2	0.030	0.040	2.682	0.529	7.03E-07		
4.2	0.030	0.060	2.822	0.557	7.23E-07		
5.2	0.030	0.080	2.858	0.564	3.13E-07		
6.2	0.030	0.100	2.931	0.578	2.96E-07		
7.2	0.030	0.120	2.930	0.578	2.64E-07		
8.2	0.030	0.150	2.907	0.574	1.33E-07		
1.3	0.060	0.000	3.022	0.596	1.11E-05	3.25E-01	120.42
2.3	0.060	0.020	3.317	0.655	1.09E-05	3.23E-01	
3.3	0.060	0.040	3.620	0.715	2.66E-05	3.22E-01	121.14
4.3	0.060	0.060	3.198	0.631	4.77E-06	3.30E-01	
5.3	0.060	0.080	3.083	0.608	3.90E-06	3.26E-01	121.34
6.3	0.060	0.100	3.187	0.629	3.35E-06	3.33E-01	
7.3	0.060	0.120	3.161	0.624	1.19E-06	3.35E-01	121.41
8.3	0.060	0.150	3.059	0.604	1.68E-07	3.42E-01	
1.4	0.100	0.000	3.802	0.750	2.04E-05	3.30E-01	119.24
2.4	0.100	0.020	4.297	0.848	6.05E-05	3.27E-01	
3.4	0.100	0.040	3.834	0.757	8.00E-05	3.15E-01	120.23
4.4	0.100	0.060	4.391	0.867	8.00E-05	3.04E-01	
5.4	0.100	0.080	3.783	0.747	3.98E-05	3.19E-01	120.67
6.4	0.100	0.100	3.727	0.736	2.24E-05	3.17E-01	
7.4	0.100	0.120	4.451	0.878	2.82E-05	3.23E-01	120.95
8.4	0.100	0.150	3.758	0.742	3.05E-06	3.20E-01	
1.5	0.150	0.000	4.275	0.844	2.57E-05	3.60E-01	
2.5	0.150	0.020	4.406	0.870	4.75E-05	3.49E-01	
3.5	0.150	0.040	4.509	0.890	6.41E-05	3.38E-01	
4.5	0.150	0.060	4.295	0.848	6.06E-05	3.42E-01	
5.5	0.150	0.080	4.198	0.829	4.57E-05	3.49E-01	
6.5	0.150	0.100	4.340	0.856	2.77E-05	3.49E-01	
7.5	0.150	0.120	4.537	0.895	2.83E-05	3.45E-01	

8.5	0.150	0.150	4.408	0.870	8.61E-06	3.53E-01	
1.6	0.200	0.000	4.328	0.854	1.09E-05	3.82E-01	
2.6	0.200	0.020	4.308	0.850	1.54E-05	3.73E-01	
3.6	0.200	0.040	4.247	0.838	2.21E-05	3.73E-01	
4.6	0.200	0.060	4.217	0.832	3.11E-05	3.65E-01	
5.6	0.200	0.080	4.205	0.830	2.47E-05	3.65E-01	
6.6	0.200	0.100	4.451	0.878	2.37E-05	3.66E-01	
7.6	0.200	0.120	4.318	0.852	1.41E-05	3.60E-01	
8.6	0.200	0.150	4.628	0.913	8.39E-06	3.58E-01	
1.7	0.250	0.000	4.435	0.875	5.19E-06	4.01E-01	117.88
2.7	0.250	0.020	3.970	0.784	6.47E-06	3.90E-01	
3.7	0.250	0.040	4.112	0.812	9.69E-06	3.90E-01	119.59
4.7	0.250	0.060	4.401	0.869	1.86E-05	3.78E-01	
5.7	0.250	0.080	4.149	0.819	1.49E-05	3.77E-01	120.17
6.7	0.250	0.100	4.252	0.839	1.56E-05	3.73E-01	
7.7	0.250	0.120	4.397	0.868	1.22E-05	3.66E-01	120.32
8.7	0.250	0.150	4.543	0.897	6.59E-06	3.68E-01	
1.8	0.300	0.000	4.405	0.869	4.26E-06	3.97E-01	
2.8	0.300	0.020	4.300	0.849	6.22E-06	3.97E-01	
3.8	0.300	0.040	4.289	0.847	9.64E-06	3.90E-01	
4.8	0.300	0.060	4.200	0.829	1.46E-05	3.79E-01	
5.8	0.300	0.080	4.244	0.838	1.55E-05	3.72E-01	
6.8	0.300	0.100	4.439	0.876	1.16E-05	3.73E-01	
7.8	0.300	0.120	4.564	0.901	1.12E-05	3.67E-01	
8.8	0.300	0.150	4.417	0.872	3.08E-06	3.74E-01	

Reference

1. Adams, S. & Rao, R. P. Ion transport and phase transition in $\text{Li}_{7-x}\text{La}_3(\text{Zr}_{2-x}\text{M}_x)\text{O}_{12}$ ($\text{M} = \text{Ta}^{5+}, \text{Nb}^{5+}, x = 0, 0.25$). *Journal of Materials Chemistry* **22**, 1426–1434 (2012).
2. Knauth, P. Inorganic solid Li ion conductors: An overview. *Solid State Ionics* **180**, 911–916 (2009).
3. Hu, Z. *et al.* Enhanced Li ion conductivity in Ge-doped $\text{Li}_0.33\text{La}_0.56\text{TiO}_3$ perovskite solid electrolytes for all-solid-state Li-ion batteries. *New Journal of Chemistry* **42**, 9074–9079 (2018).
4. Belous, A., Pashkova, E., Gavrilenko, O., V'yunov, O. & Kovalenko, L. Solid electrolytes based on lithium-containing lanthanum metaniobates and metatantalates with defect-perovskite structure. *Ionics* **9**, 21–27 (2003).
5. Kawakami, Y., Ikuta, H. & Wakihara, M. Ionic conduction of lithium for perovskite-type compounds, $\text{Li}_x\text{La}_{(1-x)}/3\text{NbO}_3$ and $(\text{Li}_{0.25}\text{La}_{0.25})_{1-x}\text{Sr}_{0.5x}\text{NbO}_3$. *Journal of Solid State Electrochemistry* **2**, 206–210 (1998).
6. Carrillo, L. *et al.* Superstructure determination of the perovskite $\beta\text{La}_{0.33}\text{NbO}_3$. *Journal of Materials Science* **35**, 3047–3052 (2000).
7. García-Martín, S. & Alario-Franco, M. Á. Modulated Structure of $\text{La}_{1/3-x}\text{Li}_3\text{NbO}_3$ $0 \leq x \leq 0.06$ Perovskite-Related Materials. *Journal of Solid State Chemistry* **148**, 93–99 (1999).
8. Yang, Z. *et al.* Arrangement in $\text{La}_{1/3}\text{NbO}_3$ Obtained by First-Principles Density Functional Theory with Cluster Expansion and Monte Carlo Simulation. *Journal of Physical Chemistry C* **124**, 9746–9754 (2020).
9. Jalem, R. *et al.* Bayesian-Driven First-Principles Calculations for Accelerating Exploration of Fast Ion Conductors for Rechargeable Battery Application. *Scientific Reports* **8**, 5845 (2018).
10. Nakayama, M. *et al.* Data-Driven Materials Exploration for Li-Ion Conductive Ceramics by Exhaustive and Informatics-Aided Computations. *Chemical Record* **19**, 771–778 (2019).
11. Seko, A. *et al.* Prediction of Low-Thermal-Conductivity Compounds with First-Principles Anharmonic Lattice-Dynamics Calculations and Bayesian Optimization. *Physical Review Letters* **115**, 1–5 (2015).
12. Ju, S. *et al.* Designing nanostructures for phonon transport via Bayesian optimization. *Physical Review X* **7**, 1–10 (2017).
13. Harada, M. *et al.* Bayesian-optimization-guided experimental search of NASICON-type solid electrolytes for all-solid-state Li-ion batteries. *Journal of Materials Chemistry A* **1**, (2020).
14. Brochu, E., Cora, V. M. & de Freitas, N. A Tutorial on Bayesian Optimization of Expensive Cost Functions, with Application to Active User Modeling and Hierarchical Reinforcement Learning. (2010).
15. Nazareth, J. L. *An Optimization Primer. An Optimization Primer* (Springer New York, 2004). doi:10.1007/978-1-4684-9388-7
16. Ueno, T., Rhone, T. D., Hou, Z., Mizoguchi, T. & Tsuda, K. COMBO: An efficient Bayesian optimization library for materials science. *Materials Discovery* **4**, 18–21 (2016).
17. García-Martín, S., Rojo, J. M., Tsukamoto, H., Morán, E. & Alario-Franco, M. A. Lithium-ion conductivity in the novel $\text{La}_{1/3-x}\text{Li}_3\text{NbO}_3$ solid solution with perovskite-related structure. *Solid State Ionics* **116**, 11–18 (1999).
18. Gao, X. *et al.* Cation ordering in A-site-deficient Li-ion conducting perovskites $\text{La}_{(1-x)}/3\text{Li}_x\text{NbO}_3$. *Journal of Materials Chemistry A* **3**, 3351–3359 (2015).
19. Shao, Y. *et al.* Grain boundary dominated ion migration in polycrystalline organic-inorganic halide perovskite films. *Energy and Environmental Science* **9**, 1752–1759 (2016).

-
20. Zawrah, M. F. & Shaw, L. Liquid-phase sintering of SiC in presence of CaO. *Ceramics International* **30**, 721–725 (2004).
 21. Li, R. *et al.* Realizing fourfold enhancement in conductivity of perovskite Li_{0.33}La_{0.557}TiO₃ electrolyte membrane via a Sr and Ta co-doping strategy. *Journal of Membrane Science* **582**, 194–202 (2019).
 22. Shen, L. *et al.* Preparation and characterization of Ga and Sr co-doped Li₇La₃Zr₂O₁₂ garnet-type solid electrolyte. *Solid State Ionics* **339**, 114992 (2019).
 23. Ling, M., Zhu, X., Jiang, Y. & Zhu, J. Comparative study of solid-state reaction and sol-gel process for synthesis of Zr-doped Li_{0.5}La_{0.5}TiO₃ solid electrolytes. *Ionics* **22**, 2151–2156 (2016).
 24. Gaberscek, M., Moskon, J., Erjavec, B., Dominko, R. & Jamnik, J. The Importance of Interphase Contacts in Li Ion Electrodes: The Meaning of the High-Frequency Impedance Arc. *Electrochemical and Solid-State Letters* **11**, A170 (2008).
 25. Snoek, J., Larochelle, H. & Adams, R. P. Practical Bayesian Optimization of Machine Learning Algorithms. in *Advances in Neural Information Processing Systems 25* (eds. Pereira, F., Burges, C. J. C., Bottou, L. & Weinberger, K. Q.) 2951–2959 (Curran Associates, Inc., 2012).
 26. Oliynyk, A. O. *et al.* High-Throughput Machine-Learning-Driven Synthesis of Full-Heusler Compounds. *Chemistry of Materials* **28**, 7324–7331 (2016).
 27. Emmerich, M. T. M., Giannakoglou, K. C. & Naujoks, B. Single- and multiobjective evolutionary optimization assisted by Gaussian random field metamodells. *IEEE Transactions on Evolutionary Computation* **10**, 421–439 (2006).

Chapter 5 Conclusion

The performance of the secondary battery as an energy device mainly depends on the rate-determining ability of the ion diffusion in the solid, this research is carried out at the atomic level to understand the ion diffusion process and migration mechanism in the solid. We aim to study the phenomenon of lithium ion conduction in solid oxide materials through multi-scale first-principles calculations, molecular dynamics simulations and other methods. However, the modulated microstructure exist in the material which is hard to be clearly characterized by the experiment method, but it will affect the ion conduction process, so the simulation of the crystal structure at multiple scales is very important step for the study of physical properties such as ion diffusion. To ensure fast and accurate simulations on a sub-nanosecond level with several thousand atoms system, we applied fast empirical force fields to perform MD simulations. But if we want to improve the performance of the material, it is impossible to do the exploration without the experimental methods. However, when using traditional experimental method to design and screen the new material, faced with an infinite number of potentially feasible ternary or multi-component compounds and their derivatives is inevitable, we hope to speed up the exploration of feasible compounds. Combined with informatics methods is a possible way to reduce the complexity of the mutual constraints of multiple factors involved in the exploration process. More specifically, DFT calculation combined with cluster expansion and Monte Carlo simulation in multiple scale were adopted to reveal the micro-modulated arrangement of cation/vacancy of $\text{La}_{1/3}\text{NbO}_3$ (LLNO)(Chapter 2). DFT-derived force field molecular dynamics (FFMD) simulation via a metaheuristic approach were adopted to investigate the migration behavior of Li-ion in $\text{Li}_x\text{La}_{(1-x)/3}\text{NbO}_3$ (Chapter 3). As a proof-of-concept study, we show that the Bayesian optimization (BO) method efficiently searches for the best composition and that material retrieval during experimental exploration can benefit from BO. (Chapter 4)

Conclusion on Chapter2: The structural features of $\text{La}_{1/3}\text{NbO}_3$ and the potential modes of the modulated structure of the La-rich layer were revealed using ab initio density functional calculations with cluster expansion and Monte Carlo simulation. The cluster expansion formalism was suitable for calculating the total energy obtained using DFT calculation for an A-site-deficient perovskite structure. Based on MC simulation

results, the structural feature of alternate La-rich and La-poor layer stacking along the *c*-axis was well reproduced when the supercell was even in size. The most stable La/vacancy arrangement in the La-rich layer of $\text{La}_{1/3}\text{NbO}_3$ was obtained by MC simulation with the supercell $12 \times 12 \times 12$; the arrangement was composed of several $4a_p \times 6a_p$ periodic units in which most of the La ions surrounded central vacancies, resulting in the formation of a closed arrangement. Moreover, a second potential La/vacancy arrangement with a slightly higher energy was found by simulating a $36 \times 36 \times 36$ supercell; this structural arrangement tends to exist in larger systems and at higher temperatures. The second arrangement is different from the first one in that there is no obvious ordered short-range structure, although a long-range ordered structure is observed along the diagonal direction $[1\ 1\ 0]_p$. Based on our results, we believe that these two different types of modulated arrangements will coexist in the real system, and closed arrangement with relatively low energy will account for the majority of the structure. It is foreseeable that when we dope Li-ions, most of them will occupy the center of the $4a_p \times 6a_p$ periodic units. La-ions around the corner of these $4a_p \times 6a_p$ periodic units will block the diffusion path of Li-ions, which may be the reason for the lower-than-expected Li ion conductivity in LLNO.

Conclusion on Chapter 3: As the further study on chapter 2, in this chapter, the FF parameter sets for a perovskite-type material, LLNO, were determined via a metaheuristic algorithm based on AIMD outputs. The Li-ion conduction behaviors of modulated and disordered arrangements of La/Vac existing in LLNO were investigated via FFMD for the first time. The modulated arrangements in LLNO significantly influenced the migration of Li ions. The existence of an alternating interlayer arrangement resulted in higher migration energy diffusing along the *c*-axis due to a large potential gap for Li ions between La-rich and La-poor layers. In addition, 2D Li migration pathways in the *ab* plane were obstructed by La ions in the La-rich layer. Hopping along the *c*-axis was required for the long-range migration of Li and was, therefore, the rate-determining process. As a result, numerous intrinsic vacancies (mainly in the La-poor layer) became inaccessible, which is the main reason that the bulk ionic conductivity of LLNO is lower than that of LLTO. Interestingly, two of the modulated structures (closed and striped arrangements) displayed higher Li-ion conductivity than disordered structures by a factor of 10 at 800 K. In addition, the migration energy in the *ab* plane appeared to be much

lower than along the c-axis. Consequently, a further improvement in the Li-ion conductivity can be achieved by eliminating La obstruction during long-distance migration. In this chapter, although we only take LLNO as an example, we performed molecular dynamics simulations by optimizing FFs parameters to reveal the influence between the microstructure of the material and the ion transition. At the same time, the research scheme of this work is also applicable to the study of other oxide and sulfide solid electrolyte materials. Provides research guidance for high-throughput material retrieval.

Conclusion on Chapter 4: As the extension of chapter 2 and chapter 3, we want to improve the electrochemical performance of LLNO by conventional experimental methods. Based on the typical $\text{La}_{1/3}\text{NbO}_3$ perovskite-type material, we synthesized $(\text{Li}_y\text{La}_{(1-y)/3})_{1-x}\text{Sr}_{0.5x}\text{NbO}_3$ ($0 \leq 0.5x \leq 0.15$, $0 \leq y \leq 0.25$) compositions by co-doping with Li^+ and Sr^{2+} . We optimized the co-doping composition through comprehensive structural characterization and by analyzing the electrochemical performance of the prepared samples. The highest ionic conductivity at room temperature (8.002×10^{-5} S/cm), which includes contributions from bulk and grain-boundary conduction, was observed for the $(\text{Li}_{0.1}\text{La}_{0.3})_{0.92}\text{Sr}_{0.04}\text{NbO}_3$ composition. The doped ions improve the total ionic conductivity differently. Due to differences in ionic radii, Li^+ diffuses through pipes around La^{3+} ions as the major ion-conducting carrier. In contrast, the larger Sr^{2+} ions form larger vacancies, which increase the size of the Li-ion migration pathway and reduce the energy barrier for hopping. In addition, the sintered morphologies of the obtained samples reveal that Li_2CO_3 significantly increases the relative density of the sample, which helps to reduce grain-boundary resistance, with Sr^{2+} also exhibiting a positive effect. Due to numerous influencing factors that are difficult to quantify, the compositional dependence of the Li-ion conductivity is rather complicated. Conventional experimental compositional optimization approaches rely on a large amount of repetitive work that is based on personal experience and intuition. To improve material-screening efficiency we demonstrated the feasibility of combining Bayesian optimization, which is used in informatics, to materials science. Random searching and the BO-based search approach were both used to predict the optimal solution in a 64 sample dataset. The BO method was found to require an average of 20 observation steps to locate the optimal solution in the dataset, with a success rate in excess of 99%. Compared to the random-search method,

the BO approach shortens the number of required steps by two-thirds and dramatically improves efficiency. In addition, for multi-objective optimization, we applied the MOBO approach to Pareto frontier searching using the experimental dataset, which also improved efficiency. In summary, this part of work highlights the feasibility of applying BO and related techniques to optimizing the compositions of complete compounds in materials science.

From the above studies, it is very effective and visualization to investigate the crystal structure in multiple scale and the ion diffusion process by the combination of first-principles calculation, Monte Carlo simulation, force fields molecular dynamics and other methods. Due to the limitations of traditional experimental exploration, in the future material research, the combination of material science and computational science will become closer and closer. As the direction of future development, it is foreseeable that in the next few years, the application of high-throughput calculation methods, combined with experimental research, will greatly accelerate our research and development of lithium battery materials, and deepen our understanding of various problems in lithium batteries. At the same time, the integration of different disciplines will also become more important, data mining, data analysis, optimization of material screening efficiency, and reduction of calculation costs through informatics technology will all be the hotspots in the future.

Chapter 6 Appendix

6.1 Density functional theory¹⁻⁵

6.1.1 what is density functional theory

Density represents the density of electrons, the functional means that energy is a function of electron density, and the electron density is a function of space coordinates, and the function of the function is the functional.

6.1.2 Some definitions

A wave function in quantum mechanics describes the quantum state of a set of particles in an isolated system.

Operator: Does a mathematical operation on a variable.

Quantum mechanical operator: Any observable in quantum mechanics is represented by an operator.

Ground state: The most stable state of a system ----- lowest energy

6.1.3 Many particle problem in solids

Find the ground state for a collection of atoms by solving the Schrodinger equation

$$\hat{H}\psi(\{r_i\}, \{R_I\}) = \hat{E}\psi(\{r_i\}, \{R_I\}) \quad (6-1-1)$$

If we are interested in finding the ground state of a set of particles, the way is to solve the many body Schrodinger equation, when we have the wave function, which describes our system of atoms or nuclei and electrons, and the hamiltonian \hat{H} which will apply to the wave function, it is just an operator can divided into energy terms \hat{T} , kinetic energy operator, and \hat{V}_{Coloumb} which includes all Colombo interactions.

$$\hat{H} = \hat{T} + \hat{V}_{\text{Coloumb}} \quad (6-1-2)$$

\hat{T} : kinetic energy operator

$$\hat{V}_{\text{Coloumb}} = \frac{q_i q_j}{|\vec{r}_i - \vec{r}_j|} : \text{pair of charge particles}$$

6.1.4 The Born Oppenheimer approximation

To solve the many-body Schrodinger equation is to complicate, we apply the Born Oppenheimer approximation, the basic idea of this approximation is that the nuclei are big and heavy, electrons are small and fast which means we can decouple the dynamics of the nuclei and the electrons, making solving the ground state of the electrons possible

by fixing a set of atomic positions.

$$m_{\text{nuclei}} \gg m_e \quad (6-1-3)$$

$$\psi(\{r_i\}, \{R_I\}) \rightarrow \psi_N(\{R_I\})^* \psi_e(\{r_i\}) \quad (6-1-4)$$

The many-particle problem in solids with the help of Born Oppenheimer approximation can transform into solving the Schrodinger equation for electrons, which greatly reduced the number of variables.

$$\hat{H} \psi(r_1, r_2, r_3 \dots r_N) = E \psi(r_1, r_2, r_3 \dots r_N) \quad (6-1-5)$$

Right now the Hamiltonian only consists of terms which include electrons, kinetic energy at terms, potential terms which include the electrons are interaction with the nuclei which is only considered as an external potential, and electron electron repulsion.

$$\hat{H} = -\frac{\hbar}{2m_e} \sum_i^{N_e} \nabla_i^2 + \sum_i^{N_e} V_{\text{ext}}(r_i) + \sum_{i=1}^{N_e} \sum_{j>1} U(r_i, r_j) \quad (6-1-6)$$

For a system of N electrons, each electron contains three space coordinates, and this equation contains 3N variables, which makes it very difficult to really solve it.

6.1.5 Density functional theory—from wavefunctions to electron density

Here we need to approach the density functional theory, the electron density is actually a true observable, which in principle can be measured from the wave function that will reduce the variables from 3N to 3 spatial dimensions.

$$n(r) = \psi^*(r_1, r_2, r_3 \dots r_N) \psi(r_1, r_2, r_3 \dots r_N) \quad (6-1-7)$$

If we want to further simplify the problem, we still need to apply another idea, Hatree-Fock approximation which make the multi-electron system is simplified to a single-electron system, and the solution becomes possible. Specific, the j^{th} electron is treated as point charge in the field of all the other electrons.

$$\psi(r_1, r_2, r_3 \dots r_N) = \psi_1(r_1)^* \psi_2(r_2)^* \psi_3(r_3)^* \dots \psi_N(r_N) \quad (6-1-8)$$

Define the electron density in terms of the individual electron wave functions:

$$n(r) = 2 \sum_i \psi_i^*(r) \psi_i(r) \quad (6-1-9)$$

6.1.6 Hobenberg and Kohn—the heart of DFT

Here we are approaching the heart of the DFT theory, which based on two very fundamental theorems.

Theorem 1: The ground state energy E is a unique functional of the electron density.

$$E = E[n(r)] \quad (6-1-10)$$

Theorem 2: The electron density that minimized the energy of the overall functional

is the true ground state electron density.

$$E[n(r)] > E_0[n_0(r)] \tag{6-1-11}$$

Based on the idea of Hohenberg-Kohn theorem, the energy functional can be divided into two main parts, the one is known and the other is unknown.

$$E[(\Psi_i)] = E_{\text{Known}}[(\Psi_i)] + E_{\text{XC}}[(\Psi_i)] \tag{6-1-12}$$

$$E_{\text{Known}}[(\Psi_i)] = -\frac{\hbar}{2m_e} \sum_i^{N_e} \int \Psi_i^* \nabla^2 \Psi_i d^3r + \int V(r)n(r)d^3r + \frac{e^2}{2} \iint \frac{n(r)n(r')}{r-r'} d^3r d^3r' + E_{\text{ion}} \tag{6-1-13}$$

$E_{\text{XC}}[(\Psi_i)]$: exchange-correlation functional

$E_{\text{XC}}[(\Psi_i)]$ includes all quantum mechanical terms, which is not known, needs to be approximated, and simplest XC-functionals LDA, Local density approximation; GGA, Generalized gradient approximation.

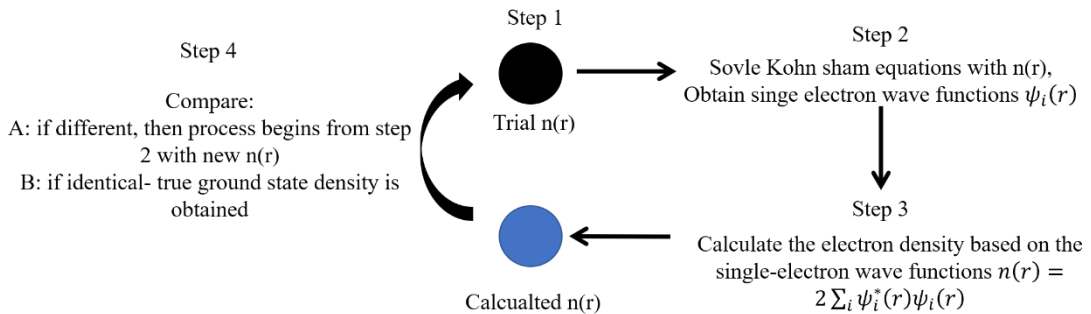
6.1.7 The Kohn sham scheme

Solve a set of single-electron wave functions that only depend on three spatial variables, $\psi(r)$

$$\left[-\frac{\hbar}{2m} \nabla^2 + V(r) + V_H(r) + V_{\text{XC}}(r) \right] \psi_i(r) = \epsilon_i(r) \psi_i \tag{6-1-14}$$

The first thing is to consider the single electron wave functions and they are not interacting, the interactions are sort of implicitly accounted for in these potentials, the hamiltonian for the single electron wave functions is the external potential and then the Hartree potential enhance the \hat{H} , which is just an electron interacting with the electron density, then this exchange correlation potential which has to be approximated.

Self-consistency scheme:



6.1.8 Approximation of exchange correlation potential

It is an approximation used in one of the exchange-related energy functionals of density functional theory. This approximation considers that the exchange correlation energy functional is only related to the value of the electron density at each point in space (and has nothing to do with its gradient, Laplace, etc.). Although there are many methods that can reflect the local density approximation, the most successful in practice is the functional based on the uniform electron gas model.

$$E_{XC}^{LDA}(n) = \int n(r)\epsilon_{xc}(n)dr \quad (6-1-15)$$

It is simply a function of electron density. Exchange related energy can be decomposed into exchange items and related items:

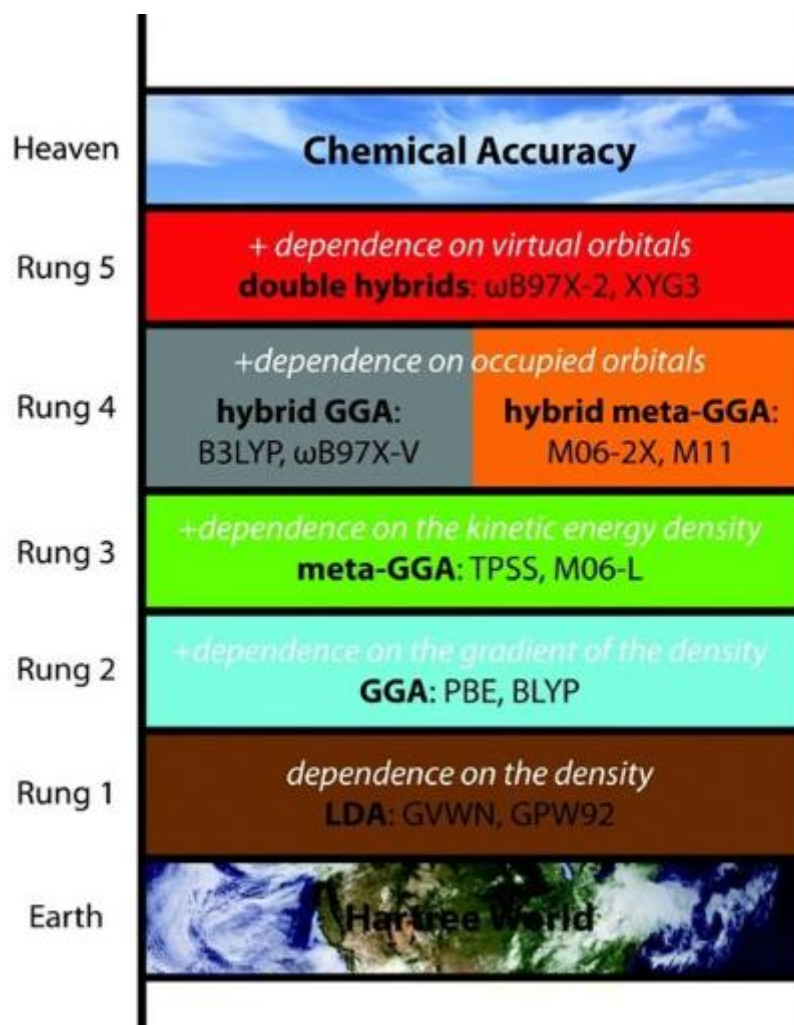
$$E_{xc} = E_x + E_c \quad (6-1-16)$$

The problem then becomes to find expressions for exchange terms and related terms separately. For the uniform electron gas model, the exchange term has a simple analytic formula, and the related term only has an accurate expression under special circumstances. Different approximations of related effects can result in different E_c . For practical functionals, the form of the energy density term of the correlation action is always very complicated.

This is considered to be suitable when the change in electron density in the substance is small, and the calculation result shifts when it becomes a strongly electron correlation system such as a transition metal oxide or a lanthanoid compound. Therefore, an approximation was devised that considers the first derivative of the electron density in addition to the mean field of the exchange correlation potential in this LDA, and this is called Generalized Gradient Approximation (GGA).

6.1.9 Summary of DFT

The core idea of density functional theory: through approximation, an easy-to-calculate, non-interactive but inaccurate result is separated, and then all errors are separately collected into the exchange correlation functional for analysis. Therefore, the choice of the exchange correlation functional term E_{xc} is very important, because it will directly determine the accuracy of the calculation result. Regarding the choice of exchange correlation functionals, you can use a diagram called Jacob's Ladder (as shown in Figure 6.1) to understand intuitively.

Fig 6.1 Jacob's Ladder⁶

The density functional theory should still be viewed from a critical perspective: it is not omnipotent. From a practical perspective, although density functional theory has become one of the basic tools in the research fields of physics, chemistry, materials, etc., with sufficiently high calculation accuracy, it cannot actually find the exact solution of Schrödinger's equation because of the exchange the precise form of the correlation functional can never be given accurately, which makes the calculated result and the actual result inevitably have errors. In addition, in the following important situations, density functional theory cannot give a good physical exact solution:

Calculation of electronic excited state. Although density functional theory can certainly be used to predict the properties of electronic excited states, strictly speaking, the accuracy of this prediction is not guaranteed in theory, because the Hohenberg-Kohn theorem is for the ground state.

Calculation of the band gap of semiconductor and insulator materials. Using the existing functional standards, the accuracy of the band gap calculated by the density functional theory is limited, and an error greater than 1 eV generally exists compared with the experimental data. How to use density functional theory to accurately deal with this problem is still an active research field.

Calculation of van der Waals forces between atoms and molecules. Density functional theory can hardly give accurate results in this situation. One explanation is that van der Waals force is a direct result of long-range electronic correlation effects. To solve this problem, more advanced wave function methods must be used instead of density functional theory.

Calculation of a large number of atoms. This is actually a problem of calculation cost. At present, the calculation amount of density functional theory is usually around dozens of atoms. From a physical point of view, even a drop of water contains atoms of an ultra-high order of magnitude. If you want to solve all atoms directly and "simple and rude", you need to rely on computer technology or program efficiency to have very huge progress and breakthroughs. It's hard to ask for. Therefore, how to connect the calculation results of a very small number of atoms with real materials with physical relevance is also a problem that researchers who use density functional theory must understand.

6.2 Monte Carlo method⁷⁻¹³

6.2.1 Monte Carlo method and history

Monte Carlo is a city in Monaco on the Mediterranean coast. It is a world-famous casino. The calculation method is named after this place, which shows that the algorithm is closely related to randomness and probability. In fact, Monte Carlo method is also called random simulation method, random sampling technique or statistical testing method.

The random sampling method can be traced back to the Buffon random needle injection experiment in the second half of the 18th century. Buffon discovered the relationship between the probability of random needle injection and π . However, the paper published by Metropolis and Ulam in 1949 is generally regarded as the symbol of the birth of the MC method. The 1940s was the age of the advent of electronic computers and

the age of the development of the atomic bomb. The development of the atomic bomb involves a large number of complex theoretical and technical issues, such as physical processes, neutron transport and radiation transport. Scientists combined the random sampling method with computer technology when solving problems such as neutron transportation, which resulted in the Monte Carlo method.

6.2.2 The basic idea of Monte Carlo method

The basic idea of the Monte Carlo method is to establish an appropriate probability model or random process in order to solve a certain problem so that its parameters (such as the probability of an event, the mathematical expectation of random variables, etc.) are equal to the solution to the problem. Then carry out repeated random sampling tests on the model or process, and carry out statistical analysis on the results, and finally calculate the required parameters to obtain an approximate solution to the problem. Monte Carlo method is a stochastic simulation method, but it is not limited to simulating randomness problems, but can also solve deterministic mathematical problems. For random problems, you can directly conduct random sampling tests according to the probability law of actual problems, that is, direct simulation methods. For the deterministic problem, the indirect simulation method is used, that is, the solution of the deterministic problem is obtained through statistical analysis of the results of random sampling.

The Monte Carlo method is mainly used to solve the problem of determinism in the field of mathematics, while in materials science, it is mainly to solve the problem of randomness. Here is a simple example to illustrate the Monte Carlo method to solve deterministic problems.

If it is required to solve a definite integral:

$$I = \int_a^b f(x)dx \quad (6-2-1)$$

First, transform the integral to construct a new integrand function $g(x)$ so that the function satisfies the following conditions:

$$g(x) \geq 0$$

$$\int_{-\infty}^{\infty} g(x)dx=1 \quad (6-2-2)$$

Obviously, $g(x)$ is the probability density function of the continuous random variable ξ , so the formula (6-2-1) becomes a probability integral whose integral value is equal to the probability $P_r(a \leq \xi \leq b)$

$$I = P_r(a \leq \xi \leq b) \quad (6-2-3)$$

This step is the process of transforming an integral into a probability model, and then repeated random sampling experiments, using the statistical average of the sampling results as the approximate value of the probability to obtain the integral. The specific test steps are as follows:

Generate a random variable value x_i that obeys the given distribution function $g(x)$.

Check whether x_i fall into the integration area ($a \leq x \leq b$). If the condition is met, record it once.

Repeat the above test. Assuming that after N trials, the total number of times that x_i falls into the integration region is m , then the integral value is approximately expressed as:

$$I \approx \frac{m}{N} \quad (6-2-4)$$

6.2.3 Monte Carlo simulation of randomness problems

The method of random experiment is used to directly simulate the random process and solve the random problem. This is the so-called direct Monte Carlo simulation. Such as simulation of Brownian motion, diffusion process, organic polymer morphology, grain growth and other random problems.

Markov chain

For simple sampling, each sampling is independent. As in the random walking process, each walking step has nothing to do with the previous step, and it has nothing to do with the initial position. The essence of importance sampling Monte Carlo method is that each sampling experiment is not completely independent, but has a certain probability relationship with the previous or all previous sampling results, such as non-returning random walking and self-avoiding random walking.

Suppose the state sequence (random variable sequence) of a system $x_0, x_1, \dots, x_n, \dots$, if for any state x_n is only related to the previous state x_{n-1} and has nothing to do with the initial state, the probability of state n is:

$$p(x_n | x_{n-1}, \dots, x_1, x_0) = p(x_n | x_{n-1}) \quad (6-2-5)$$

Call this sequence Markov chain. The Markov chain is a random walking state. The probability of walking from state i to state j in a single walk is called transition probability.

$$p_{ij} = p(x_j | x_i) = p(x_i \rightarrow x_j) \quad (6-2-6)$$

Assuming that all possible states are N , the $N \times N$ matrix formed by p_{ij} is called transition matrix p , and the sum of the elements in each row of the matrix is equal to 1. The important property of the Markov chain is that regardless of the initial state, the final state (a sufficient number of time steps) will follow a certain unique distribution, which is called the limit distribution x_{lim} .

$$x_{lim} = x_{lim} \times p \quad (6-2-7)$$

In other words, the state no longer changes after the limit state is multiplied by the transition probability, which means the system reaches an equilibrium state. Therefore, the Markov chain is of great significance in the equilibrium Monte Carlo simulation. For example, for the canonical ensemble, the temperature is constant, and the state of the system corresponds to the heat balance distribution, which means the limit probability of the Markov chain is proportional to the Boltzmann factor:

$$p(x_i) \propto \exp \left[-\frac{H(x_i)}{KT} \right] \quad (6-2-8)$$

In the formula, H is the Hamiltonian of the system, this shows that the probability of each state of the system depends on the temperature and Hamiltonian of the system, which is the core of the Metropolis Monte Carlo method.

Here give a sample example of Markov chain, and how does the transition probability work.

Consider a Two-level system, and the transition matrix $p \begin{pmatrix} 0.5 & 0.5 \\ 1 & 0 \end{pmatrix}$, assume the initial state $x_1 = (1 \ 0)$, so the state x_2 should be

$$x_2 = (1 \ 0) \begin{pmatrix} 0.5 & 0.5 \\ 1 & 0 \end{pmatrix} = (0.5 \ 0.5) \quad (6-2-9)$$

By the same way, state x_3 will equal $(0.75 \ 0.25)$, this recursion can get the limit state $x_{lim} = \begin{pmatrix} 2 & 1 \\ 3 & 3 \end{pmatrix}$

$$\begin{pmatrix} 2 & 1 \\ 3 & 3 \end{pmatrix} \begin{pmatrix} 0.5 & 0.5 \\ 1 & 0 \end{pmatrix} = \begin{pmatrix} 2 & 1 \\ 3 & 3 \end{pmatrix} \quad (6-2-10)$$

The result shows that $\begin{pmatrix} 2 & 1 \\ 3 & 3 \end{pmatrix}$ is the limit state. The sequence $(x_1, x_2, \dots, x_{lim})$ is a Markov chain. It can be proved that the initial state $(0 \ 1)$ can also reach limit state by the same transition matrix, which means the limit distribution of Markov chain has nothing

to do with the initial state.

Metropolis Monte Carlo method

Monte Carlo methods are mainly divided into simple random sampling methods and important random sampling methods. Simple sampling is sampling with an even distribution, and each sampling is completely independent. As mentioned in the previous section on the integral problem, many problems are difficult to solve with simple sampling methods, and important random sampling can obtain good results.

The Metropolis Monte Carlo method is an important random sampling method. Metropolis et al. proposed a method based on the establishment of a Markov process. The essence of this method is that the states of the system are not selected independently of each other. Instead, build a Markov process, in which each state x_{i+1} is obtained from the previous state x_i through an appropriate transition probability $W(x_i \rightarrow x_{i+1})$, moreover, this probability can make the distribution function $p(x_i)$ of the state produced by the Markov process tend to the desired equilibrium distribution under the limit of $M \rightarrow \infty$.

$$p_{\text{eq}}(x_i) = \frac{1}{Z} \exp \left[-\frac{H(x_i)}{k_B T} \right] \quad (6-2-11)$$

The sufficient conditions to meet the above requirements are:

$$p_{\text{eq}}(x_i) W(x_i \rightarrow x_j) = p_{\text{eq}}(x_j) W(x_j \rightarrow x_i) \quad (6-2-12)$$

$$\frac{W(x_i \rightarrow x_j)}{W(x_j \rightarrow x_i)} = \exp \left[-\frac{dH}{k_B T} \right] \quad (6-2-13)$$

The ratio of the transition probabilities of the two states forward and reverse depends only on the energy difference between the two states $dH = H(x_j) - H(x_i)$. The form of transition probability W usually takes the following forms.

$$W(x_i \rightarrow x_j) = \begin{cases} \frac{1}{t_s} \exp \left(-\frac{dH}{k_B T} \right), & dH > 0 \\ \frac{1}{t_s}, & \text{other conditions} \end{cases} \quad (6-2-14)$$

In the formula, t_s is an arbitrary factor. When the dynamic process is not considered, t_s can be taken as 1. When discussing dynamics, t_s is the unit of "Monte Carlo time", and W is called "transition probability per unit time".

The specific steps of Metropolis Monte Carlo method are as follows:

- (1) Establish a model of the relationship between system state and energy.

(2) Starting from the initial state, establish a new state through simple sampling. (3) According to the Hamiltonian ΔH of the old and new states, judge the accept or not of the new state. There are three situations for judging the rejection:

1. $\Delta H < 0$, accept the new state and continue for step (2);

2. $\Delta H > 0$, not directly judge, but to further judge and draw a random number ξ

$$\xi \begin{cases} \leq \exp\left(-\frac{\Delta H}{k_B T}\right), \text{ accept new state} \\ > \exp\left(-\frac{\Delta H}{k_B T}\right), \text{ refuse new state} \end{cases}$$

3. If the new state is rejected, take the original state as the new state, repeat step (2), and record it once.

If the number of particles in the system is M , one particle is randomly selected for each new state sampling, not every particle is performed one by one. As long as the quality of the pseudo-random number is high enough, the probability of each particle being sampled is equal. When the number of sampling reaches the total number of particles M in the system, the process is called a Monte Carlo step (MCS). The relationship between system configuration and energy is an important part of the Monte Carlo method for random simulation.

6.2.4 Energy model of Monte Carlo method

The Monte Carlo method first establishes an appropriate model of the relationship between system configuration and energy according to the process to be simulated. After randomly selecting a new configuration of the system, calculates the energy change before and after the system configuration change to determine the new configuration. The relationship model between system configuration and energy plays an important role in the Monte Carlo method. The Monte Carlo method is mainly to simulate the state of the system, not the process, so the energy relationship is different from the potential function of molecular dynamics. The potential function is the relationship between the relative distance between particles and energy, and the relationship between configuration and energy in the Monte Carlo method is only a function of the particle state. Sometimes the relationship is only a qualitative description. The absolute value of energy is not important, as long as it can be described qualitatively. The energy difference between the two configurations is sufficient.

Ising model

In this model, the system is composed of regular lattice points, and each lattice point has a particle (atom or molecule), and each particle has only two states, and the two states contribute equally to the energy of the system, but the sign is opposite. Then the relationship between system energy and state is:

$$H_{\text{Ising}} = -J \sum_{\langle i,j \rangle} S_i S_j - B \sum_i S_i, S_i = \pm 1 \quad (6-2-15)$$

In this formula, J is the effective interaction energy of the particles, S_i is the state value of particle i , and B is the energy generated by the action of a certain intensity thermodynamics field on the particle i . It can be seen from the above formula that the energy of the system is composed of two parts, one is the contribution of the particle pair interaction, and the other is the effect of the external field on the particle. Both parts are related to the state value S_i of the particle. The most typical application of the Ising model is the magnetic moment simulation model in solids. The state S_i of the lattice point is ± 1 , which represents spin-up and spin-down, respectively. The first term of the energy model represents the interaction energy between each magnetic moment, and the second term represents the effect of the external magnetic field on each magnetic moment.

Heisenberg model

From equation (6-2-15), it can be seen that the Ising model can only consider simple binary problems, but certain properties of the particles at the grid point position have directionality and the directionality of these particles cannot be described by simple binary values. At this time, the interaction of its particles cannot use the Ising model. At this time, the interaction between particles should consider its vector relationship, and the energy model must be able to consider the problem of any vector angle. Heisenberg proposed an amendment to the Ising model:

$$H_{\text{heis}} = -J \sum_{\langle i,j \rangle} S_i^z S_j^z - J_{\perp} \sum_{\langle i,j \rangle} (S_i^x S_j^x + S_i^y S_j^y) - B \sum_i S_i^z, S_i = \pm 1 \quad (6-2-16)$$

Lattice gas model

The lattice nodes considered by the Ising model and Heisenberg model must have particles that must be considered, but vacancies cannot be considered, or although there are particles occupying the node, the particles do not interact with surrounding particles, such as not having magnetism, etc. Happening. The lattice gas model solves this problem well

$$H_{\text{gas}} = -J_{\text{int}} \sum_{\langle i,j \rangle} t_i t_j - \mu_{\text{int}} \sum_i t_i, t_i = 0,1 \quad (6-2-17)$$

J_{int} is the nearest neighbor interaction energy, it only includes the situation where the

nearest neighbor lattice points are occupied, μ_{int} is the chemical potential, which determines the number of atoms on each lattice point. The lattice gas Hamiltonian is a conventional two-state operator, so the lattice gas model can be converted to the usual Ising model.

6.2.5 Summary of Monte Carlo method

The MC method is generally based on simpler criteria, such as the principle of least energy, etc. It only uses random sampling to achieve the goal, and does not strictly simulate the realization process, it only considers the state and does not mind the process. Therefore, the calculation method and program structure are very simple, less restricted by complex conditions, and highly adaptable. Since the convergence speed and accuracy of the MC method have nothing to do with the dimensionality of the problem, the specialty of this method is to solve multi-dimensional problems, but the calculation efficiency of the MC method is low.

The Metropolis MC method establishes a relationship between the states of the system by establishing a Markov process, rather than being completely independent. Each state is obtained from the previous state through an appropriate transition probability. Therefore, the Metropolis MC method can not only change the system in the direction of energy reduction, but also increase the energy of the system with an appropriate probability, thereby overcoming the barrier and making the system develop to a lower energy level instead of staying at the local minimum value of energy.

The MC energy model is very different from the MD potential function. The MC energy model only considers the energy change caused by the state change, while the MD potential function can describe the relationship between the particle position and the force, and then can calculate the particle's movement direction and velocity.

6.3 Molecular Dynamics

6.3.1 What is Molecular Dynamics

Molecular Dynamics simulation is to use computer methods to represent statistical mechanics, as an auxiliary means of experiment. The molecular dynamics simulation method is a deterministic method. It determines the transformation of configuration according to the internal dynamics of the system and tracks the individual movement of

each particle in the system; then according to the laws of statistical physics, the microscopic quantities are given (Molecular coordinates, velocity) and macroscopic observable measurements (temperature, pressure, specific heat capacity, elastic modulus, etc.) to study the material properties.

The molecular dynamics method first needs to establish the motion equations of a group of molecules in the system, and by solving the motion equations of all particles (molecules), to study the basic processes of the system related to microscopic quantities. The rigorous solution of this kind of multi-body problem requires the establishment and solution of the Schrödinger equation of the system. According to the Born Oppenheimer approximation, the movement of electrons is dealt with separately from the movement of the nucleus, the movement of electrons is dealt with by the method of quantum mechanics, and the movement of the nucleus is dealt with by the classical dynamics method.

6.3.2 Basic idea of molecular dynamics

The laws of classical mechanics

The movement of particles in the system treated in molecular dynamics obeys Newton's equation:

$$F_i(t) = m_i a_i(t) \quad (6-3-1)$$

The force $F_i(t)$ on the atom I can be directly used as the first derivative of the potential energy function with respect to the coordinate r_i , $F_i(t) = -\frac{\partial U}{\partial r_i}$, where U is the potential energy function. Therefore, for each particle of the N particle system:

$$\begin{cases} m_i \frac{\partial v_i}{\partial t} = F = -\frac{\partial U}{\partial r_i} + \dots \\ r(t) = v(t) \end{cases} \quad (6-3-2)$$

In these equations, v is the velocity vector and m_i is the mass of the particle. The solution of these equations generally requires numerical methods (analytic methods can only solve the simplest potential function form, which is meaningless in actual simulation). These numerical solutions produce a series of position and velocity pairs $\{x^n, v^n\}$, n represents a series of discrete time, $t = n\Delta t$, Δt represents the time interval (time step). To solve this system of equations, the initial coordinates and velocity of each particle in the system must be given.

6.3.3 Molecular dynamics method work scheme

Given the coordinates and speed at time t and other dynamic information, then the

coordinates and speed at time $t + \Delta t$ can be calculated. Δt is the time step, which is related to the integration method and the system. Figure 6.2 shows working scheme. The input of information (parameters) is to set the potential function representing the interaction force between atoms or molecules. If the properties of the thermodynamic equilibrium state are considered, physical environmental conditions such as temperature and pressure need to be set.

The criteria for a good integration algorithm in molecular dynamics mainly include:

- a) Fast calculation speed
- b) Need less computer memory
- c) Allow longer time steps
- d) Show better energy conservation

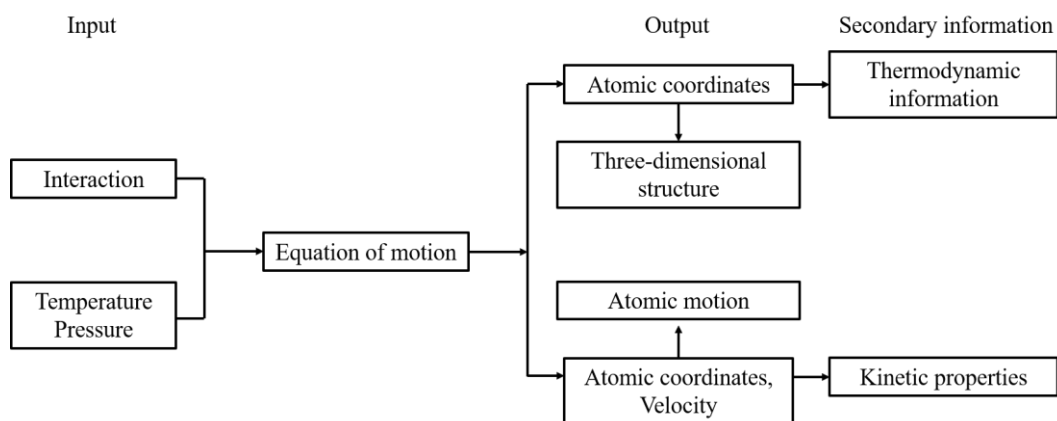


Fig 6.2 Molecular dynamics method work scheme

6.3.4 The scope of application of molecular dynamics

The molecular dynamics method only considers the motion of the nucleus in the multi-body system, while the motion of the electron is not considered, and the quantum effect is ignored. The classical approximation is more accurate in a wide range of material systems; however, it is not applicable to chemical reactions involving charge redistribution, bond formation and breaking, dissociation, polarization, and chemical bonds of metal ions. In this case, quantum mechanics methods are required. The classical molecular dynamics method (MD) is also not suitable for low temperature, because the energy gap between discrete energy levels given by quantum physics is larger than the thermal energy of the system, and the system is limited to one or several low energy states. When the temperature increases or the frequency related to motion decreases (with a longer time scale), the discrete energy level description becomes unimportant. Under such

conditions, higher energy levels can be described by thermal excitation.

The preliminary estimation of the frequency of the Newtonian physical characteristic motion can be carried out according to the simple harmonic analysis.

$$\left\{ \begin{array}{l} \frac{h\gamma}{k_B T} \gg 1, \text{ Not applicable to classic sports} \\ \frac{h\gamma}{k_B T} \ll 1, \text{ applicable to classic sports} \end{array} \right. \quad (6-3-3)$$

h - Planck's constant, γ - vibration frequency, the classical method is not suitable for relatively high frequency motion. At 300k, $k_B T=2.5$ J/mol, from Table.6.1 can be seen that these problems cannot be dealt with classical theory.

Table 6.1 T=300k High frequency vibration mode and its ratio¹⁴

Vibration mode	Wave ($1/\lambda$) cm^{-1}	Frequency γ	$\frac{h\gamma}{k_B T}$
O-H stretch	3600	1.1×10^{14}	17
C-H stretch	3000	9.0×10^{13}	14
O-C-O asym.stretch	2400	7.2×10^{13}	12
C=O (carbonyl) stretch	1700	5.1×10^{13}	8
C-N stretch	1250	3.8×10^{13}	6
O-C-O bend	700	2.1×10^{13}	3

6.3.5 Flow chart of molecular dynamics operation

Initial system setup

From Figure 6.3 It can be seen that in order to perform molecular dynamics calculations, you must first establish a calculation model, set the initial coordinates and initial speed of the calculation model; select the appropriate time step; select the appropriate interaction potential function between atoms to calculate the force ; Select the appropriate algorithm, boundary conditions and external conditions; calculate; perform statistical processing on the calculated data.

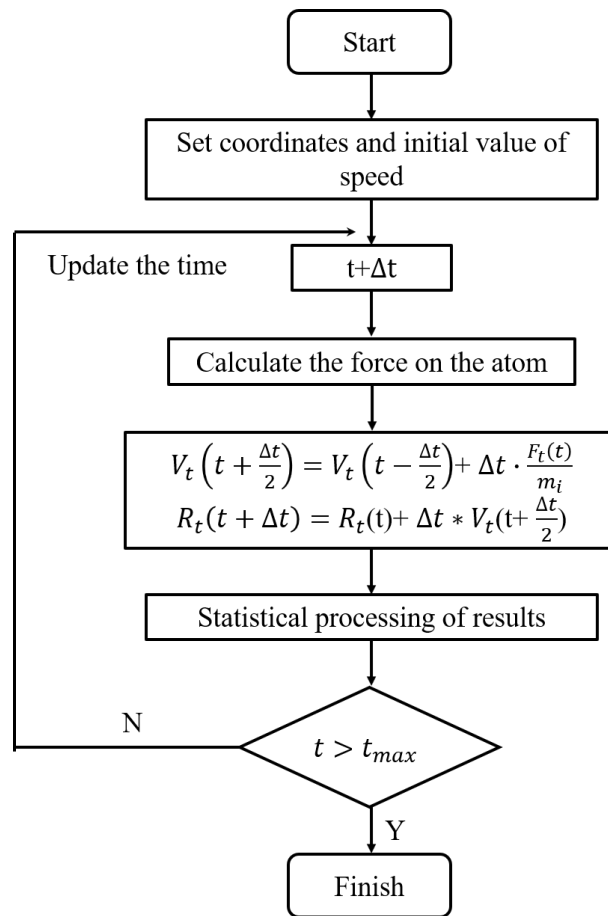


Fig 6.3 Flow chart of molecular dynamics operation

Molecular dynamics is composed of three main parts: initialization, equilibrium, and result analysis. The initial coordinates can be obtained from the crystal structure, the initial velocity vector is set according to the pseudo-random number, so that the total kinetic energy of the system corresponds to the target temperature. According to the classic energy equalization theorem, the energy of each degree of freedom is $k_B T/2$ in thermal equilibrium. N_F is the total number of degrees of freedom of the system.

$$\langle E \rangle = \frac{1}{2} \sum_{i=1}^{3N} m_i v_i^2 = N_F k_B T/2 \quad (6-3-4)$$

After the initial coordinates and initial speed of the system are set, before proceeding to simulate the properties of the system, the system must first be brought into equilibrium. In this process, kinetic energy and potential energy are transformed into each other. When the kinetic energy, potential energy, and total energy fluctuate only around the average value, the system reaches equilibrium (corresponding to the microcanonical ensemble).

Force calculation method

More than 90% of the calculation time spent in molecular dynamics simulation is

used to calculate the force acting on the atom, and the time used is roughly proportional to the square of the number of atoms. For short-range forces, the cut-off radius method is used, which means only the forces within the force range are calculated, which greatly reduces the amount of calculation; for long-range forces such as Coulomb force, it is necessary to find an approximate treatment method to reduce the amount of calculation. Ewald summation method is a commonly used one.

1. Cut-off radius method¹⁵

Pre-select cut-off radius r_c , only calculated the force between particles in the sphere with the r_c . $L > 2r_c$ (L is the length of the periodic box of MD). When the number of particle of system is too large, the Verlet algorithm can be used.

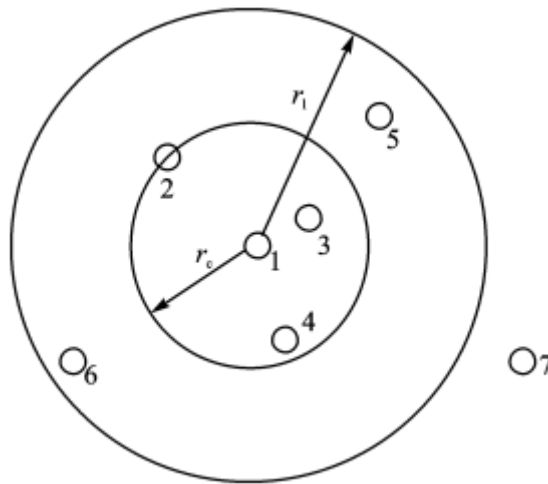


Fig 6.4 Neighborhood list

Figure 6.4 can be established for each particle in the system. r_c is the truncation radius and r_1 is the neighborhood radius. When calculating the force of particle 1, only calculate the sum of the forces on particle 1 of the three particles 2, 3, and 4 within the truncation radius, and the effects of other particles are ignored. During the calculation process, this table needs to be updated every certain number of steps.

2. Ewald summation¹⁶

The Ewald summation method was developed by Ewald in 1921 when he was studying the energy of ionic crystals. In this method, a particle interacts with all other atoms in the simulated box and mirror particles in periodic cells. The Coulomb potential between charges is:

$$U = \frac{1}{2} \sum_{i=1}^N \sum_{j=1}^N \frac{q_i q_j}{4\pi\epsilon_0 r_{ij}} \quad (6-3-5)$$

r_{ij} is the distance of charge i and charge j , There are 6 boxes at L from the center box.

$$U = \frac{1}{2} \sum_{n \text{ box}=1}^6 \sum_{i=1}^N \sum_{j=1}^N \frac{q_i q_j}{4\pi\epsilon_0 |r_{ij} + r_{\text{box}}|} \quad (6-3-6)$$

The potential energy of the charge at the center of the box is usually written as

$$U = \frac{1}{2} \sum_{|n|=0}^{\infty} \sum_{i=1}^N \sum_{j=1}^N \frac{q_i q_j}{4\pi\epsilon_0 |r_{ij} + n|} \quad (6-3-7)$$

The problem now is: the sum of this formula converges very slowly, in fact it is conditionally convergent. Ewald uses a technique in the summation, which is to transform the above equation into two series that converge quickly. Each point charge is surrounded by two charge distributions of equal size and opposite signs, as shown in Figure 6.5.

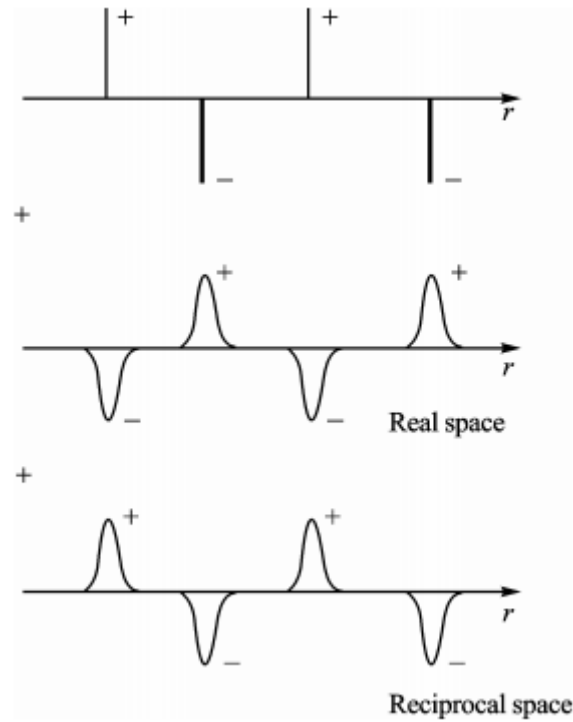


Fig 6.5 The charge distribution in Ewald summation method

This charge distribution function is represented by Gaussian distribution as:

$$\rho(r) = \frac{q_i \alpha^3}{\pi^{1.5}} \exp(-\alpha^3 r^2) \quad (6-3-8)$$

The real space summation is given by:

$$U_1 = \frac{1}{2} \sum_{i=1}^N \sum_{j=1}^N \sum_{|n|=0}^{\infty} \frac{q_i q_j}{4\pi\epsilon_0} \frac{\text{erfc}(|r_{ij} + n|)}{|r_{ij} + n|} \quad (6-3-9)$$

In this formula, erfc is residual error function:

$$\text{erfc}(x) = \frac{2}{\sqrt{\pi}} \int_x^{\infty} \exp(-t^2) dt \quad (6-3-10)$$

The new summation of the error-containing function can quickly converge. The speed of convergence depends on the width of the Gaussian function. The wider the Gaussian distribution function, the faster the series will converge.

The second term, the potential function generated by the charge distribution function is:

$$U_2 = \frac{1}{2} \sum_{k \neq 0} \sum_{i=1}^N \sum_{j=1}^N \frac{1}{\pi L^3} \frac{q_i q_j}{4\pi\epsilon_0} \frac{4\pi^2}{k^2} \exp\left(-\frac{k^2}{4\alpha^2}\right) \cos(k \cdot r_{ij}) \quad (6-3-11)$$

The potential of real space should also include the third term: the interaction of the Gaussian charge distribution itself:

$$U_3 = -\frac{\alpha}{\sqrt{\pi}} \sum_{k=1}^N \frac{qk^2}{4\pi\epsilon_0} \quad (6-3-12)$$

In addition, the potential generated by the spherical medium around the simulation box must be added:

$$U_{\text{correction}} = \frac{2\pi}{3L^3} \left| \sum_{i=1}^N \frac{q_i}{4\pi\epsilon_0} r_i \right|^2 \quad (6-3-13)$$

So, the total expression of Ewald sum should be:

$$U = \frac{1}{2} \sum_{i=1}^N \sum_{j=1}^N \left\{ \sum_{|n|=0}^{\infty} \frac{q_i q_j}{4\pi\epsilon_0} \frac{\text{erfc}(|r_{ij}+n|)}{|r_{ij}+n|} + \sum_{k \neq 0} \frac{1}{\pi L^3} \frac{q_i q_j}{4\pi\epsilon_0} \frac{4\pi^2}{k^2} \exp\left(-\frac{k^2}{4\alpha^2}\right) \cos(k \cdot r_{ij}) - \frac{\alpha}{\sqrt{\pi}} \sum_{k=1}^N \frac{qk^2}{4\pi\epsilon_0} + \frac{2\pi}{3L^3} \left| \sum_{i=1}^N \frac{q_i}{4\pi\epsilon_0} r_i \right|^2 \right\} \quad (6-3-14)$$

6.3.6 Numerical solution of molecular motion equation

The Newton equation of the multi-particle system cannot be solved analytically and needs to be solved by numerical integration. The basic idea of the finite difference technique is to divide the integration into many small steps, and the time of each small step is fixed at δt . The sum of the forces of a particle is equal to the vector sum of the interaction forces between it and all other particles. According to this force, we can get the acceleration of this particle, combined with the position and velocity at time t , we can get the position and velocity at time $t + \delta t$. This force is assumed to be constant during the time interval.

Here are a few common algorithms:

Verlet algorithm¹⁷

Using the position and velocity at t and $t-\delta t$, to calculate the position $r(t+\delta t)$, the derivation of the Verlet algorithm can be expanded by using Taylor series.

$$r_i(t + \delta t) = r_i(t) + \delta t v_i(t) + \frac{1}{2} \delta t^2 a_i(t) + \dots \quad (6-3-15)$$

$$r_i(t-\delta t) = r_i(t) - \delta t v_i(t) + \frac{1}{2} \delta t^2 a_i(t) - \dots \quad (6-3-16)$$

Sum up (6-3-15) (6-3-16):

$$r_i(t + \delta t) = 2r_i(t) - r_i(t - \delta t) + \delta t^2 \frac{F_i(t)}{m_i} \quad (6-3-17)$$

$$v(t) = [r(t + \delta t) - r(t - \delta t)] / 2\delta t \quad (6-3-18)$$

The Verlet algorithm is simple, but the disadvantage is that the position $r(t + \delta t)$ which is a small term must be obtained by the difference between very large two terms $2r(t)$ and $r(t - \delta t)$ which is likely to cause loss of accuracy. The velocity term is not shown in the equation, and it is not a self-heuristic algorithm.

Leap-frog algorithm¹⁸

The speed differential is expressed by the difference of the speed at the time $t + \delta t$ and $t - \delta t$.

$$\frac{v_i(t + \delta t/2) - v_i(t - \delta t/2)}{\delta t} = \frac{F_i(t)}{m_i} \quad (6-3-19)$$

The velocity of $t + \delta t$

$$v_i(t + \delta t/2) = v_i(t - \delta t/2) + \frac{F_i(t)\delta t}{m_i} \quad (6-3-20)$$

the differential of atomic coordinates can be expressed as

$$\frac{r_i(t + \delta t) - r_i(t)}{\delta t} = v_i(t + \delta t/2) \quad (6-3-21)$$

To execute the leap-frog algorithm, $v(t - \frac{\delta t}{2})$ and acceleration at t must be determined to calculate the $v(t + \frac{\delta t}{2})$, then $r(t + \delta t)$ can be calculated by equation (6-3-21).

$$v(t) = \frac{1}{2} \left[v\left(t + \frac{\delta t}{2}\right) + v\left(t - \frac{\delta t}{2}\right) \right] \quad (6-3-22)$$

The Leap-frog algorithm has two advantages over the Verlet algorithm: it includes a velocity term, and the amount of calculation is slightly smaller. It also has obvious flaws: position and speed are not synchronized. This means that at a certain position, it is impossible to calculate the contribution of kinetic energy to the total energy at the same time.

Velocity Verlet algorithm¹⁹

The velocity Verlet algorithm can give position, velocity and acceleration at the same

time without sacrificing accuracy.

$$r_i(t + \delta t) = r(t) + \delta t v_i(t) + \frac{1}{2m} F_i(t) \delta t^2 \quad (6-3-23)$$

$$v_i(t + \delta t) = v_i(t) + \frac{1}{2m} [F_i(t + \delta t) + F_i(t)] \delta t^2 \quad (6-3-24)$$

The algorithm needs to store the coordinates, speed and force of each time step. Each time step of this method involves two time steps, and it is necessary to calculate the force after the coordinate update and before the speed update. Among these three algorithms, the speed Verlet algorithm has the best accuracy and stability. The calculation of force is time-consuming, if memory is not a problem, higher-order methods can use a larger time step, so the calculation is very beneficial.

6.3.7 Potential function²⁰⁻²⁶

The potential function is a function that represents the interaction between atoms (molecules), also known as the force field. The interaction between atoms controls the interaction behavior between atoms and fundamentally determines all the properties of the material. This effect is specifically described by the potential function.

The interaction potential between atoms can be divided into classical potential and first-principle potential according to the source; the classical potential can be divided into the interaction potential between atoms and the interaction potential between molecules according to the scope of use; according to the form of the potential function, it can be divided into pairs Potential and multi-body potential, which as shown in Figure 6.6.

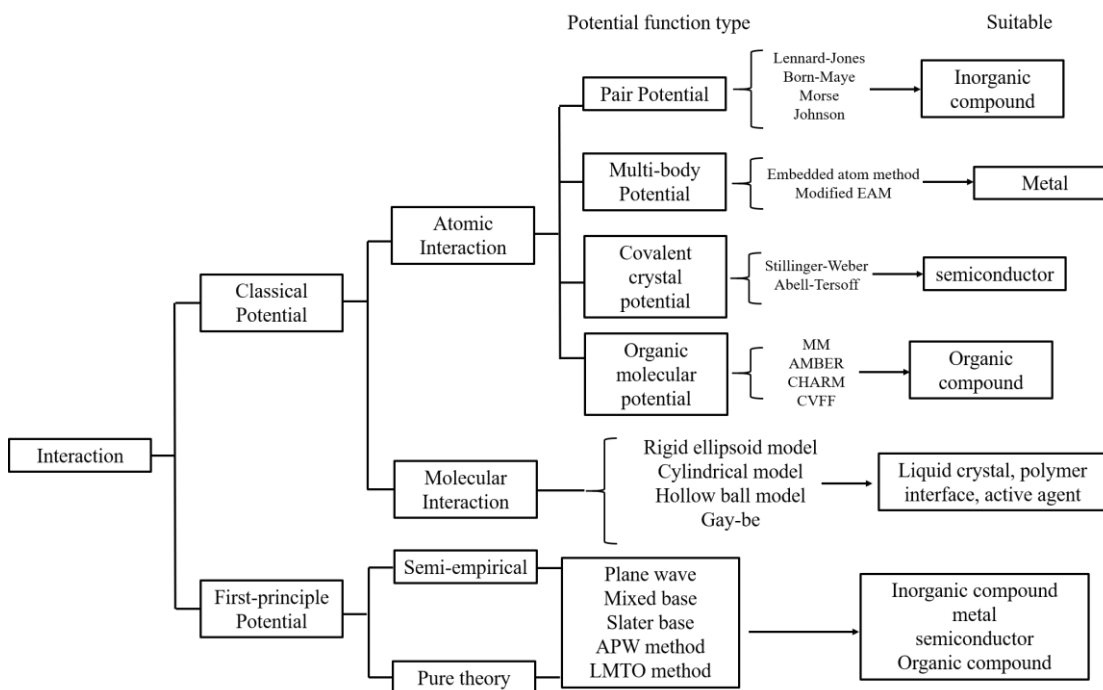


Fig 6.6 Classification of interaction potential

In this work, the specific used potential, and formula as shown in Chapter 3 method part. Here, it mainly introduces the classification of potential field, and its specific mathematical expression will not be introduced in detail.

6.3.8 Ensemble theory^{27,28}

Ensemble is a concept of statistical mechanics, which was created by Gibbs in 1901. The object of molecular dynamics research is a multi-particle system, but due to the limitation of computer memory and calculation speed, the number of particles in the simulated system is limited, but the laws of statistical physics are still valid, so the computer-simulated multi-particle system uses statistics to describe the laws of physics.

An ensemble is a huge system, composed of identical systems with exactly the same composition, nature, size and shape, and a collection of extremely large numbers of systems. Each system is in a certain state of microscopic motion, and is independent of each other. The microscopic state of motion constitutes a continuous area in the phase space (the space formed by the generalized coordinates and the generalized momentum is called the phase space), and the macroscopic quantity corresponding to the microscopic quantity is the average of all possible motion states under certain macroscopic conditions. For any microscopic quantity $A(p, q)$, the macroscopic average can be expressed as:

$$\bar{A} = \frac{\int A(p,q)\rho(p,q,t)d^{3N}qd^{3N}p}{\rho(p,q)d^{3N}qd^{3N}p} \quad (6-3-25)$$

In the formula, N is the total number of particles in the system, q and p are the generalized coordinates and generalized momentum, and ρ is the weighting factor.

Molecular dynamics and Monte Carlo methods include equilibrium and non-equilibrium simulations. According to the characteristics of the research object, the main ensembles are micro-canonical ensemble (NVE), canonical ensemble (NVT), isothermal and pressure ensemble (NPT), isenthalpy and pressure ensemble (NPH) and so on.

Reference

1. 徐光宪, 黎乐民 & 王德民. 量子化学. 基本原理和从头计算法. 中 (1985).
2. 谢希德 & 陆栋. 固体能带理论. (1998).
3. Hohenberg, P. & Kohn, W. Inhomogeneous electron gas. *Physical review* **136**, B864 (1964).
4. Kohn, W. & Sham, L. J. Self-consistent equations including exchange and correlation effects. *Physical review* **140**, A1133 (1965).
5. Callaway, J. & March, N. H. Solid State Phys. *Adv. Res. Appl* **38**, 135 (1984).
6. Perdew, J. P. & Schmidt, K. Jacob's ladder of density functional approximations for the exchange-correlation energy. in *AIP Conference Proceedings* **577**, 1–20 (American Institute of Physics, 2001).
7. Metropolis, N. & Ulam, S. The monte carlo method. *Journal of the American statistical association* **44**, 335–341 (1949).
8. Muller, M. E. Review: J. M. Hammersley, D. C. Handscomb, Monte Carlo Methods ; Yu. A. Shreider, Methods of Statistical Testing/Monte Carlo Method. *The Annals of Mathematical Statistics* **37**, 532–538 (1966).
9. Shreider, I. A., Tee, G. J. & Buslenko, N. P. *The Monte Carlo method: the method of statistical trials*. (Pergamon Press, 1966).
10. 徐钟济. 蒙特卡罗方法. (上海科学技术出版社, 1985).
11. 陈舜麟. 计算材料科学. (化学工业出版社, 2005).
12. Binder, K. Applications of Monte Carlo methods to statistical physics. *Reports on Progress in Physics* **60**, 487 (1997).
13. Gubernatis, J. E. The Monte Carlo method in the physical sciences: celebrating the 50th anniversary of the Metropolis Algorithm. *The Monte Carlo Method in the Physical Sciences* **690**, (2003).
14. Schlick, T. *Molecular modeling and simulation: an interdisciplinary guide: an interdisciplinary guide*. **21**, (Springer Science & Business Media, 2010).
15. Andersen, H. C. Molecular dynamics simulations at constant pressure and/or temperature. *The Journal of chemical physics* **72**, 2384–2393 (1980).
16. Ewald, P. P. Ewald summation. *Ann. Phys* **369**, 253 (1921).
17. Verlet, L. Computer "experiments" on classical fluids. I. Thermodynamical properties of Lennard-Jones molecules. *Physical review* **159**, 98 (1967).
18. Hockney, R. W. Methods in Computational Physics. *Alder, B* 136–211 (1970).
19. Swope, W. C., Andersen, H. C., Berens, P. H. & Wilson, K. R. A computer simulation method for the calculation of equilibrium constants for the formation of physical clusters of molecules: Application to small water clusters. *The Journal of chemical physics* **76**, 637–649 (1982).
20. 钱学森. 物理力学讲义. (上海交通大学出版社, 2007).

21. Morse, P. M. Diatomic molecules according to the wave mechanics. II. Vibrational levels. *Physical review* **34**, 57 (1929).
22. Johnson, R. A. Relationship between two-body interatomic potentials in a lattice model and elastic constants. *Physical Review B* **6**, 2094 (1972).
23. Johnson, R. A. & Oh, D. J. Analytic embedded atom method model for bcc metals. *Journal of Materials Research* **4**, 1195–1201 (1989).
24. Jacobsen, K. W., Norskov, J. K. & Puska, M. J. Interatomic interactions in the effective-medium theory. *Physical Review B* **35**, 7423 (1987).
25. Stillinger, F. H. & Weber, T. A. Computer simulation of local order in condensed phases of silicon. *Physical Review B* **31**, 5262–5271 (1985).
26. Abell, G. C. Empirical chemical pseudopotential theory of molecular and metallic bonding. *Physical Review B* **31**, 6184 (1985).
27. Andrew, R. L. Molecular modeling principles and applications. *2nd, editor.: Pearson Education Limited* (2001).
28. 蘇文鍛. 系綜原理. (廈門大學出版社, 1990).

